



DGK Veröffentlichungen der DGK

Ausschuss Geodäsie der Bayerischen Akademie der Wissenschaften

Reihe C

Dissertationen

Heft Nr. 917

Andre Cahyadi Kalia

**Landslide activity detection based on
nationwide Sentinel-1 PSI datasets**

München 2023

Bayerische Akademie der Wissenschaften

ISSN 0065-5325

ISBN 978-3-7696-5329-8

Diese Arbeit ist gleichzeitig veröffentlicht in:
Wissenschaftliche Arbeiten der Fachrichtung Geodäsie und Geoinformatik der Leibniz Universität Hannover
ISSN 0174-1454, Nr. 392, Hannover 2023

Landslide activity detection based on nationwide Sentinel-1 PSI datasets

Von der Fakultät für Bauingenieurwesen und Geodäsie
der Gottfried Wilhelm Leibniz Universität Hannover
zur Erlangung des Grades
Doktor-Ingenieur (Dr.-Ing.)
genehmigte Dissertation

von

Andre Cahyadi Kalia, Dipl.-Geogr.

München 2023

Bayerische Akademie der Wissenschaften

Adresse der DGK:



Ausschuss Geodäsie der Bayerischen Akademie der Wissenschaften (DGK)

Alfons-Goppel-Straße 11 • D – 80 539 München
Telefon +49 - 331 - 288 1685 • E-Mail post@dgk.badw.de
<http://www.dgk.badw.de>

Prüfungskommission:

Vorsitzender: Prof. Dr.-Ing. Christian Heipke

Referent: Prof. Dr. Mahdi Motagh

Korreferenten: Prof. Dr. Federico Raspini (University of Florence)
Prof. Dr.-Ing. Ingo Neumann

Tag der mündlichen Prüfung: 04.07.2023

© 2023 Bayerische Akademie der Wissenschaften, München

Alle Rechte vorbehalten. Ohne Genehmigung der Herausgeber ist es auch nicht gestattet,
die Veröffentlichung oder Teile daraus auf photomechanischem Wege (Photokopie, Mikrokopie) zu vervielfältigen

ISSN 0065-5325

ISBN 978-3-7696-5329-8

Abstract

Slow deformations of the Earth are caused by natural and anthropogenic processes and can lead to e.g. damaged buildings and infrastructure. Advanced differential interferometric SAR (A-DInSAR) processing techniques (Persistent Scatterer Interferometry - PSI, Small Baseline Subset - SBAS) are able to monitor these slow deformations with high precision and with a high spatial measurement density over large areas. Currently no other measurement technique can provide such an amount of measurements in space and time regarding transient surface deformations of the Earth. These measurements are of interest in order to improve e.g. hazard assessments for various applications (e.g. landslides, subsidence, soil compaction, fluid injection). Although the reliability and maturity of the A-DInSAR techniques have been proven by the scientific community it is hardly ever used in the day-to-day work by responsible authorities.

In order to support the use of A-DInSAR products the Ground Motion Service Germany (GMS) is operated. Before the GMS Germany was realized a service-concept was proposed to specify the characteristics of nationwide Sentinel-1 PSI datasets for the GMS. The main contributions of this thesis are i) the proposed service-concept and ii) the (semi-) automatic information extraction for landslide applications by subsequent post-processing.

During the creation of the proposed service-concept a case study based on ERS-1/2 SAR data was performed. The case study covers an area of approximately 30,000 km² in North-West Germany and surface deformation processes regarding soil compaction and natural gas extraction are present. In order to fully cover the area of interest six partly overlapping ERS-1/2 data stacks have been used (swath wide: 100 km). Each stack was independently processed using a PSI algorithm capable of handling large areas. Subsequently these results are mosaicked and GNSS-calibrated to produce a consistent and interoperable PSI dataset. The concept and case-study was accepted by the end-users and consequently the approach was extended to the entire area of Germany (approximately 360,000 km²). Therefore, six partly overlapping Sentinel-1 tracks (swath wide: 250 km) in ascending and descending orbit were processed by the PSI technique. The nationwide PSI datasets consists of tenths of millions of measurement points each consisting of a deformation time series with hundreds of measurements. Verification results based on GNSS- and levelling- time series showed a precision of ~2-3 mm a⁻¹ for the LoS (Line of Sight) velocity and ~12 m for the PS geocoding. These PSI datasets are updated in a yearly interval and published in a WebGIS capable of handling the large amount of data. Despite the high information content of such nationwide PSI datasets the use is in general done by manual visual inspection. This is time consuming, subjective and error-prone due to outliers.

In order to improve the use of nationwide PSI datasets a post-processing approach is proposed. The approach is implemented and tested for the detection of slow moving landslides on a regional scale (1,500 km²). The local Moran's Index is proposed to detect spatial clusters of deforming Persistent Scatterers (PS) in a-priori mapped landslide areas. The rationale is that spatial clusters with a consistent deformation signal are more reliable than individual PS. These semi-automatically detected deformation clusters can then be used to i) focus the attention of an end-user to a specific geographical region and ii) to intersect the attributes of the deformation clusters with a thematic layer (e.g. a-priori mapped landslide extent). Besides spatial

characteristics, the PSI datasets also consists of temporal information. Thus, a post-processing approach focusing on the deformation time series is implemented and tested. Therefore, landslides are analyzed regarding a sudden acceleration and seasonal periodical deformation signals. The time series analysis have been done in combination with a potential triggering factor to estimate the time-lag between deformation and potential triggering factor.

Keywords: Sentinel-1, InSAR, Persistent Scatterer Interferometry, Ground Motion Service Germany, Landslide

Zusammenfassung

Langsame Deformationen der Erde werden durch natürliche und anthropogene Prozesse verursacht und können z. B. zu Schäden an Gebäuden und Infrastruktur führen. Fortgeschrittene differentielle interferometrische SAR-Verfahren (A-DInSAR) (z.B. Persistent Scatterer Interferometrie - PSI, Small Baseline Subset - SBAS) sind in der Lage, diese langsamen Verformungen mit Millimetergenauigkeit über große Gebiete zu messen. Aktuell kann keine andere Messtechnik eine solche Menge an räumlichen und zeitlichen Messungen bzgl. Oberflächenverformungen liefern. Diese Messungen sind von Interesse, um z. B. Gefahrenabschätzungen für verschiedene Anwendungen zu verbessern (z. B. Erdbeben, Subsidenz, Bodenverdichtung, Flüssigkeitsinjektion). Obwohl die Zuverlässigkeit und Reife der A-DInSAR-Techniken von der wissenschaftlichen Gemeinschaft nachgewiesen wurde, wird sie in der täglichen Arbeit der zuständigen Behörden kaum eingesetzt.

Um die Nutzung von A-DInSAR-Produkten zu unterstützen, wird der BodenBewegungsdienst Deutschland (BBD) betrieben. Vor der Realisierung des BBD wurde ein Dienste-Konzept erstellt, das die Eigenschaften des GMS auf der Basis von bundesweiten Sentinel-1 PSI-Datensätzen spezifiziert. Die Hauptbeiträge dieser Arbeit sind i) das Service-Konzept und ii) die (semi-) automatische Informationsextraktion für Erdbeben-Anwendungen durch anschließendes post-processing.

Zur Erstellung des Dienste-Konzeptes wurde eine Fallstudie auf Basis von ERS-1/2 SAR-Daten durchgeführt. Die Fallstudie deckt ein Gebiet von ca. 30.000 km² im Nordwesten Deutschlands ab, in dem Deformationsprozesse im Zusammenhang mit Bodenverdichtung und Erdgasförderung auftreten. Um das Gebiet vollständig abzudecken, wurden sechs benachbarte ERS-1/-2-Datenstapel verwendet. Jeder Stapel wurde unabhängig voneinander mit dem PSI-Verfahren verarbeitet. Anschließend wurden diese Ergebnisse mosaikiert und GNSS-kalibriert, um einen konsistenten und interoperablen PSI-Datensatz zu erzeugen. Das Konzept und die Fallstudie wurden von den Endnutzern akzeptiert, so dass der Ansatz auf das gesamte Gebiet Deutschlands (ca. 360.000 km²) ausgeweitet wurde. Dazu wurden fünf Sentinel-1 Tracks im auf- und absteigenden Orbit mit der PSI-Technik verarbeitet. Die bundesweiten PSI-Datensätze bestehen aus Zehnermillionen von Messpunkten, die jeweils aus einer Deformationszeitreihe mit Hunderten von Messungen bestehen. Die Verifizierungsergebnisse auf der Grundlage von GNSS- und Nivellement-Zeitreihen zeigten eine Genauigkeit von ~2-3 mm a⁻¹ für die LoS-Geschwindigkeit und ~12 m für die PS-Geokodierung. Diese PSI Datensätze werden in jährlichen Abständen aktualisiert und in einem WebGIS veröffentlicht, das in der Lage ist, die große Datenmenge zu verarbeiten. Trotz des hohen Informationsgehalts solcher landesweiten PSI-Datensätze erfolgt die Nutzung im Allgemeinen durch visuelle Interpretation. Dies ist zeitaufwendig, subjektiv und aufgrund von Ausreißern fehleranfällig.

Um die Nutzung von landesweiten PSI-Datensätzen zu verbessern, wird ein Post-Prozessierungs-Ansatz vorgeschlagen. Der Ansatz wurde für die Erkennung von sich langsam bewegenden Erdbeben auf regionaler Ebene (1.500 km²) implementiert und getestet. Der lokale Moran-Index wird vorgeschlagen, um räumliche Cluster von sich bewegenden Persistent Scatterers (PS) in a-priori kartierten Erdbebengebieten zu erkennen. Der Grundgedanke ist, dass räumliche Cluster mit einem konsistenten Deformationssignal zuverlässiger sind als einzelne PS. Diese halbautomatisch detektierten Deformationscluster können dann verwendet werden, um i) die Aufmerksamkeit eines Endnutzers auf eine bestimmte geografische Region zu lenken und ii) die Attribute der Deformationscluster mit einer thematischen Ebene (z. B. der

a-priori kartierten Erdrutschausdehnung) zu verknüpfen. Neben den räumlichen Merkmalen enthalten die PSI-Datensätze auch zeitliche Informationen. Daher wird ein Post-Prozessierungs Ansatz mit Schwerpunkt auf den Deformationszeitreihen implementiert und getestet. So werden Erdrutsche im Hinblick auf eine plötzliche Beschleunigung und saisonale periodische Deformationssignale analysiert. Die Zeitreihenanalyse wurde in Kombination mit einem potenziellen Auslösefaktor durchgeführt, um die zeitliche Verzögerung zwischen Deformation und potenziellem Auslösefaktor abzuschätzen.

Schlagwörter: Sentinel-1, InSAR, Persistent Scatterer Interferometrie, BodenBewegungsdienst Deutschland, Erdrutsch

Contents

1	Introduction.....	10
1.1	Introduction	11
1.2	Research Objectives	12
1.3	Structure of the Thesis	12
2	Theoretical Background.....	14
2.1	SAR Imaging	15
2.1.1	Geometric Image Distortions	16
2.2	Interferometric SAR	16
2.2.1	InSAR principle.....	16
2.2.2	Phase decorrelation	17
2.2.3	Scattering mechanisms	17
2.3	Persistent Scatterer Interferometry	18
2.3.1	Interferometric processing.....	19
2.3.2	PS detection.....	19
2.3.3	Phase unwrapping	20
2.3.4	Geocoding	21
2.4	Landslides.....	21
2.4.1	Landslide mapping and monitoring based on A-DInSAR datasets.....	22
3	Scientific Contributions	24
3.1	Introduction	25
3.2	Challenges for a nationwide InSAR based Ground Motion Service	25
3.3	Contributions for a nationwide InSAR based Ground Motion Service.....	26
3.4	Challenges in PSI based landslide applications.....	26
3.5	Contributions to PSI based landslide applications	27
4	A Copernicus downstream-service for the nationwide monitoring of surface displacements in Germany	28
4.1	Abstract.....	29
4.2	Introduction	29
4.3	User requirements.....	31
4.4	Ground Motion Service Germany	34
4.5	The L2A PSI-WAP dataset.....	35
4.6	Case-study PSI-WAP Lower Saxony	44
4.7	Data-/product provision.....	52

4.8	Conclusion	54
4.9	Acknowledgements	56
5	Classification of Landslide Activity on a Regional Scale Using Persistent Scatterer Interferometry at the Moselle Valley (Germany).....	57
5.1	Abstract.....	58
5.2	Introduction	58
5.3	Study Area	59
5.4	Methodology and Data	61
5.4.1	PSI-Processing	61
5.4.2	Conversion from <i>vLOS</i> into <i>vSLOPE</i>	62
5.4.3	Cluster Analysis	62
5.4.4	Classification of the Landslides' State of Activity.....	63
5.4.5	Ancillary Data	65
5.5	Results	67
5.6	Discussion.....	72
5.7	Conclusion	73
5.8	Acknowledgements	74
6	Landslide activity detection based on Sentinel-1 PSI datasets of the Ground Motion service Germany - The Trittenheim case study.....	75
6.1	Abstract.....	76
6.2	Introduction	76
6.3	Sentinel-1 PSI dataset and study area.....	77
6.3.1	Sentinel-1 PSI dataset.....	77
6.3.2	Study area	78
6.4	Methodology.....	80
6.4.1	Active deformation area mapping	81
6.4.2	Time series classification	82
6.4.3	Wavelet analysis.....	83
6.5	Results	85
6.5.1	ADA-mapping results	85
6.5.2	Time series classification results.....	87
6.5.3	Wavelet analysis.....	88
6.6	Discussion.....	89
6.7	Conclusion	92
6.8	Acknowledgement	92
7	Conclusion	94

8	Outlook	96
9	Bibliography	97

1 Introduction

1.1 Introduction

The first civilian spaceborne SAR (Synthetic Aperture Radar) Mission was launched in 1978 by NASA. It was named Seasat and was focusing on maritime research. Although Seasat was active for only 105 days it proved the technical possibility of spaceborne SAR and marks the starting point for many follow-up SAR missions. ESA launched the first European spaceborne SAR mission in 1991, named ERS-1 (European Remote Sensing Satellite, C-Band SAR Sensor). Based on ERS-1 deformations of the Earth's surface, e.g. caused by an earthquake, became visible for the first time in an earth observation image (Massonnet et al., 1993). Since ERS-1 several SAR missions in the C-Band (ERS-2, Envisat, Radarsat-1), X-Band (SIR-C/X-SAR, SRTM) and L-Band (ALOS Palsar, SIR-A/B/C/X-SAR) provided SAR imagery with medium spatial resolutions (~20 m) for specific areas of the Earth. The focus of these SAR missions were mainly scientific studies. This changed to a certain extent by the start of commercial SAR missions, e.g. TerraSAR-X (start in 2007), TanDEM-X (start in 2010) and the COSMO-SkyMed constellation (start between 2007 and 2010). These SAR missions included advanced acquisition techniques able to provide very high spatial resolution (down to ~ 0.25 m) and higher temporal resolutions (e.g. COSMO-SkyMed revisit time = 5 days). These high resolution SAR missions made it possible to detect deformations of single buildings or infrastructure objects like bridges (Gernhardt et al., 2009, Lazecky et al., 2017).

The launch of the Copernicus Sentinel-1 mission (C-Band) on April 3rd 2014 marks an important milestone for an operational mapping of surface deformations for entire nations and even continents. This became possible because Sentinel-1 provides i) the technical capabilities (large swath: 250 km and medium spatial resolution: ~20 m x ~5 m), ii) the mapping mission design (regular acquisitions of the entire land surface and long-term mission design) and iii) the data policy (free, full and open). Thus, the Sentinel-1 enables nationwide, or even continent-wide surface deformation products and services with regularly updated products.

Today, European-wide GMS (Costantini et al., 2022), nation-wide, e.g. Norway (Dehls 2018), Germany (Kalia, 2021) and regional, e.g. Tuscany/Italy (Raspini et al., 2018) are providing Sentinel-1 (S-1) based A-DInSAR products. An overview of GMS is provided by Crosetto et al. (2020). To the authors knowledge, the first nationwide A-DInSAR dataset covers Italy and is based on ERS, Envisat and COSMO-SkyMed SAR data (Costantini et al., 2017). Due to the limited SAR data availability only the ERS descending dataset was able to provide a full coverage of Italy. ERS ascending, Envisat ascending/descending and COSMO-SkyMed ascending/descending does not provide a full coverage. Besides the limited coverage, no GNSS calibration and 2D motion decomposition was performed, which limits the interoperability of the A-DInSAR dataset with respect to other (terrestrial) measurements. In addition, no value-added-product, e.g. automatic detection of deforming areas, detection of timeseries with acceleration, is derived from these nationwide datasets. Thus, a visual inspection of millions of measurement points is required to extract these information. This is time consuming, subjective and error prone due to potential outliers.

In this thesis, first the concept of the GMS Germany is proposed. The concept includes a case study based on ERS-1/2 wide-area PSI datasets as proof-of-concept. Second, value-added products for the automatic information extraction regarding landslides are investigated. The value-added-products are based on nationwide S-1 PSI datasets from the GMS Germany.

1.2 Research Objectives

Spaceborne A-DInSAR has proven to be a powerful technique to measure deformations of the Earth's surface. Since the start of Sentinel-1 it became possible to produce A-DInSAR products for entire nations or even continents (Dehls, 2018, Kalia et al., 2019, Costantini et al., 2022). However, the use of A-DInSAR products was still limited in the day-to-day work of responsible authorities. Examples where A-DInSAR products have been operationally used by responsible authorities in Germany includes the monitoring of an uplift of the Earth's surface due to geothermal leakage (Engesser et al., 2010, Koch et al., 2015). In order to support the use of A-DInSAR products a concept for a nationwide GMS was developed. Based on this objective, research questions are:

- What are the user requirements for a nationwide Ground Motion Service in Germany?
- What are the technical requirements regarding an A-DInSAR for a nationwide Ground Motion Service in Germany?

Due to the huge amount of measurement points in a nationwide S-1 PSI product (e.g. in Germany ~100 million PS) the usually performed visual inspection of deformation rates and time series became even more challenging with respect to smaller areas of interests. The question arises how spatial- and temporal- patterns of the PSI velocity and timeseries can be detected in an automatic way. Therefore, several A-DInSAR post-processing techniques have been proposed by the scientific community (Berti et al. 2013, Chaussard et al. 2014, Haghshenas and Motagh 2016, Barra et al. 2017, Carlà et al. 2019). Research Questions addressed in this thesis are:

- What are the requirements for an automatic mapping of the landslide state of activity, detection of accelerations and seasonality within PS deformation time series?

Both groups of research questions are the objectives of this thesis.

1.3 Structure of the Thesis

This is a cumulative dissertation consisting of three peer-reviewed scientific journal publications.

Chapter 2 provides the theoretical background regarding SAR, interferometric SAR (InSAR), Persistent Scatterer Interferometry (PSI), landslides and PSI based landslide applications. Error sources in each of these techniques are addressed.

Chapter 3 shows the scientific contributions of this thesis. The chapter is split in two subchapters, the first addressing the challenges regarding a nationwide PSI dataset for the GMS Germany and the second regarding PSI based landslide applications.

Chapter 4 presents a concept for the GMS Germany based on Sentinel-1 PSI. The concept shows national user requirements and a case study based on five ERS-1/S PSI stacks located in north Germany. Chapter 4 is published in Remote Sensing of Environment (Kalia et al. 2017).

Chapter 5 provides a case study regarding the classification of landslide activity on a regional scale. It uses a nationwide Sentinel-1 PSI dataset of the GMS Germany. The PSI data is verified with GNSS time series acquired at corner reflectors. Classification results are verified with thematic maps. Chapter 5 is published in Remote Sensing (Kalia 2019).

Chapter 6 provides a case study focusing on the calculation of a time lag between an acceleration- and seasonal- signal in a PS time series and a potential landslide triggering factor. Chapter 6 is published in Landslides (Kalia 2022).

Chapter 7 provides a conclusion of this thesis and chapter 8 provides an outlook where future research directions are proposed.

2 Theoretical Background

The theoretical background of Synthetic Aperture Radar (SAR) imaging, interferometric SAR (InSAR), Persistent Scatterer Interferometry (PSI), landslides and landslide applications based on PSI are described in this chapter.

2.1 SAR Imaging

The acquisition principle of a SAR image is based on the radiation of electromagnetic waves through a SAR antenna, scattering of the electromagnetic radiation at the earth's surface and receiving of the backscattered radiation at the SAR antenna. The signal strength (amplitude), as well as the position of the electromagnetic wave (phase) is recorded at the SAR satellite. The satellite illuminates and captures the next parts of the earth surface as it moves along its flight path, forming the SAR image (Ulaby et al. 1982).

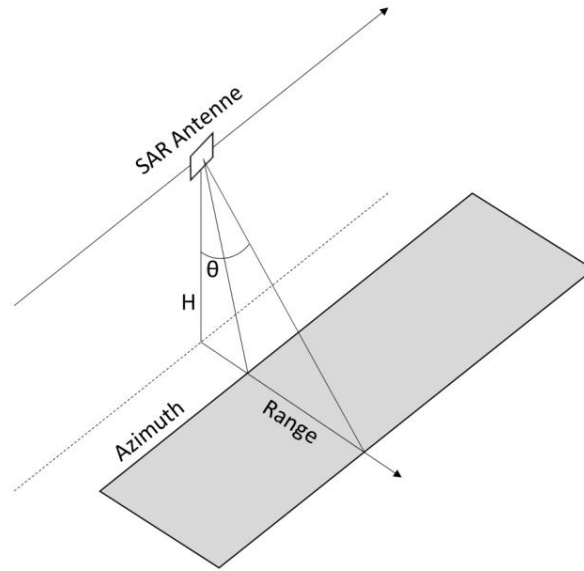


Figure 2.1: Principle of SAR imaging geometry

The interaction between the signal and the illuminated surface determines the recorded amplitude. A high amplitude value implies that there is a lot of reflection from the surface towards the sensor, whereas a low amplitude value suggests that there is not much reflection. The recorded phase is a function of the distance between the sensor and the earth surface and can be used to determine the surface topography or deformation (Ulaby et al., 1982, Bürgmann et al., 2000, Rosen et al., 2000). For every image pixel the complex SAR signal s is given by:

$$s = a \cdot e^{j\phi} = a \cdot e^{j\left(\frac{-2\pi}{\lambda}2R + \phi_{scat}\right)} = a \cdot e^{j\left(\frac{-4\pi}{\lambda}R + \phi_{scat}\right)}$$

Where a is the amplitude, ϕ is the phase, λ is the wavelength of the SAR, R is the range distance and ϕ_{scat} is the phase contribution caused by the scattering within the resolution cell. Typical spaceborne SAR wavelengths are 3.1 cm (X-Band), 5.6 cm (C-Band) and 22.9 cm (L-Band).

2.1.1 Geometric Image Distortions

Figure 1 visualizes the side-looking (slant range) SAR imaging geometry. The sensor is observing the earth's surface via the slant range geometry in order to prevent range ambiguities and strong backscatter signals from vertical observations. The incidence angle θ is the angle between the slant range plane and nadir. As a consequence of the side-looking observation geometry three types of geometrical image distortions can be distinguished: foreshortening, shadow and layover (Fig. 2.2). Foreshortening is present when a slope facing the sensor is less steep than the incidence angle. Then the time difference between the signals backscattered from the top and bottom of the object is lower than their real horizontal distance. Foreshortening areas appear bright in the SAR image, because the backscatter is compressed into a smaller area. SAR shadow happens when a slope on the backside of the look direction is steeper than the incidence angle. In these areas no signal can be retrieved and thus these areas are dark in a SAR image. The shadow effect increases with higher incidence angle. Thus areas in far range are more affected than in near range. Layover is present on slopes facing the sensor when the incidence angle is smaller than slope. In these areas, the radially emitted radar pulse reaches the top of a vertical object before the bottom. Thus in the slant range plane the top of that object is tilt over the bottom. The Layover effect increases with lower incidence angles. Thus, the near range is more effected from layover than the far range (Ulaby et al. 1982).

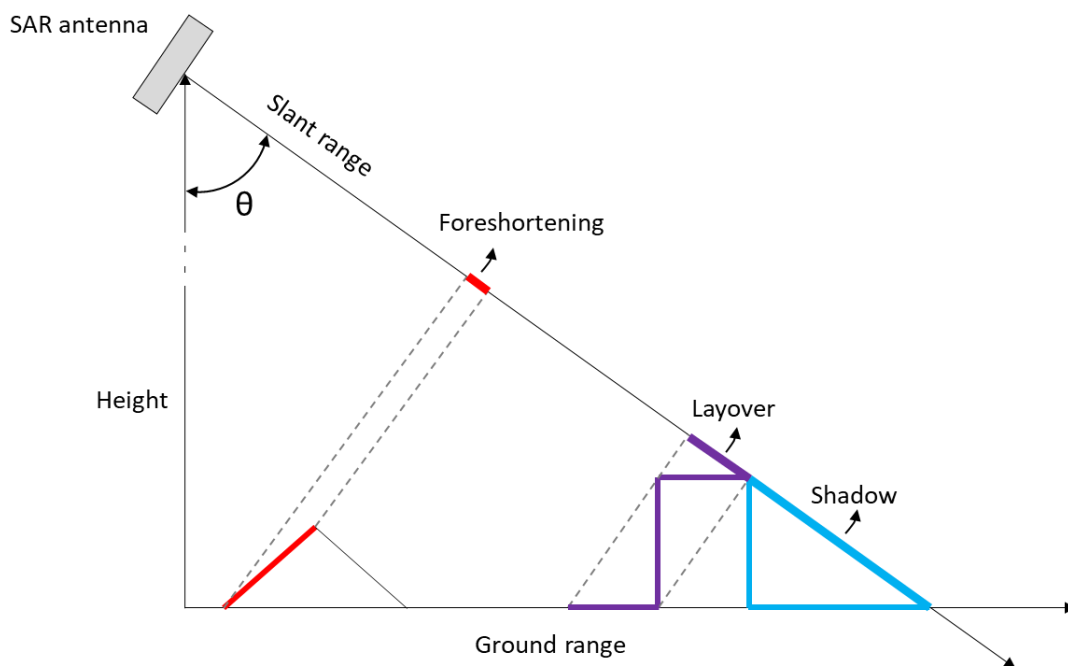


Figure 2.2: Principle of SAR foreshortening-, shadow- and layover- effect

2.2 Interferometric SAR

2.2.1 InSAR principle

The interference of two complex SAR signals is used in interferometric SAR. In repeat-pass interferometry, an interferogram is calculated by subtracting the phase of two SAR images acquired at different times from slightly different orbit positions. The resulting interferogram

consists of the phase difference for every coherent pixel. The interferogram can be characterized by the temporal- (time difference between the two SAR images) and geometrical- (spatial distance between the two orbit positions of the two SAR images) baseline. Major applications based on interferometric SAR are the mapping of the Earth's topography (Rosen et al., 2000) and deformation (Massonnet et al., 1993). The phase difference, also called the interferometric phase, has several contributions which can be decomposed into (Bamler and Hartl 1998, Rosen et al., 2000):

$$\Delta\Phi = \Delta\Phi^{gmt} + \Delta\Phi^{topo} + \Delta\Phi^{defo} + \Delta\Phi^{atmo} + \Delta\Phi^{noise}$$

With $\Delta\Phi$ as interferometric phase, $\Delta\Phi^{gmt}$ as geometric induced phase, $\Delta\Phi^{topo}$ as topography induced phase, $\Delta\Phi^{defo}$ as deformation induced phase, $\Delta\Phi^{atmo}$ as atmospheric variation induced phase and $\Delta\Phi^{noise}$ as noise induced phase. In order to retrieve the deformation of the Earth's surface, the $\Delta\Phi^{gmt}$ is estimated based on the orbit positions and subtracted from the measured interferometric phase, the $\Delta\Phi^{topo}$ is estimated based on e.g. an external digital elevation model and subtracted from the measured interferometric phase and the $\Delta\Phi^{atmo}$ is estimated based on e.g. an external numerical weather model and subtracted from the measured interferometric phase. The $\Delta\Phi^{noise}$ comes from e.g. the thermal noise of the SAR instrument and is usually ignored in interferometric processing.

2.2.2 Phase decorrelation

The interferometric phase of a pixel can only be exploited if a high similarity of the backscattered signal between both SAR acquisitions is present (Zebker and Villasenor, 1992, Hanssen, 2001). The similarity is approximated by the spatial coherence which can be calculated by:

$$\gamma = \frac{|E[s_1 s_2^*]|}{\sqrt{E[s_1 s_1^*] E[s_2 s_2^*]}}$$

With γ as spatial coherence, * as the complex conjugate of a SAR acquisition and $E[\]$ as the mathematical expectation. A low coherence value indicates a low quality of the interferometric phase of a pixel. A low coherence value can be caused by e.g. temporal- or geometrical-decorrelation. Temporal decorrelation is caused by a change of the interaction of the electromagnetic waves with the scatterers within a single resolution cell. Usually areas covered with vegetation or water are affected by temporal decorrelation because the scattering properties changes within (fractions of) seconds. Geometrical decorrelation is caused by the geometrical baseline of the SAR satellites at the time of the two acquisitions. An increased geometrical baseline causes a reduced spectral overlap of the signal and thus a decorrelation of the interferometric phase.

2.2.3 Scattering mechanisms

PSI uses Persistent Scatterer (PS) pixels, which are characterized by a long-term phase stability. In theory, two extreme scenarios of scattering mechanisms can be distinguished to describe time-coherent pixels of a stack of SAR images: PS and distributed scatterers (DS). PS are characterized by a single dominant scatterer within a resolution cell. In consequence, PS have

a low phase noise level and high signal strength. PS are not affected by temporal- or geometrical- baseline properties because they are considered to be ideal point targets. In practice, PS can be caused by e.g. a dihedral-, trihedral-, pole- or mirror- reflector as far as it has a strong and coherent scattering mechanism. PS are present in man-made and natural areas. Examples of man-made PS are buildings, traffic signs, electrical power-poles, bridges, dams or pipelines. Examples of PS in natural areas are solid surfaces without vegetation, rock outcrops or boulders. In contrast, DS are pixels, where several coherent scattering elements within a single resolution are present (Ferretti, 2014). The phase noise of DS is high and temporal- and geometrical- decorrelation exists. In order to increase the signal-to-noise ratio (SNR) of DS spatial averaging of the interferograms is performed, e.g. by multilooking.

2.3 Persistent Scatterer Interferometry

The Persistent Scatterer Interferometry (PSI) technique was invented by Ferretti et al. (1999, 2000). The motivation was to overcome the challenges of repeat-pass SAR interferometry, namely variability of the atmospheric properties, geometrical- and temporal- decorrelations. The major characteristics of PSI are i) the use of a single reference SAR image in a stack of interferograms and ii) the focus only on pixels with long-term phase stability (Persistent Scatterers, PS). A typical PSI workflow is visualized in Fig. 2.3. Based on a stack of SAR single look complex (SLC) images a reference image is chosen. Then, all images are coregistered with respect to the reference image and corresponding interferograms are formed. Based on a stack of coregistered SAR images PS pixels are detected. An external DEM is then used to model and remove the topographic phase contribution. The resulting differential interferograms are the basis for the estimation of the mean velocity and residual height for PS pixels. Then, a stochastic model is used to estimate and reduce the APS for each differential interferogram. These APS reduced differential interferograms are then used to finally estimate the mean velocity and residual height of the PS pixels. Each of these processing steps are described in the following subchapters.

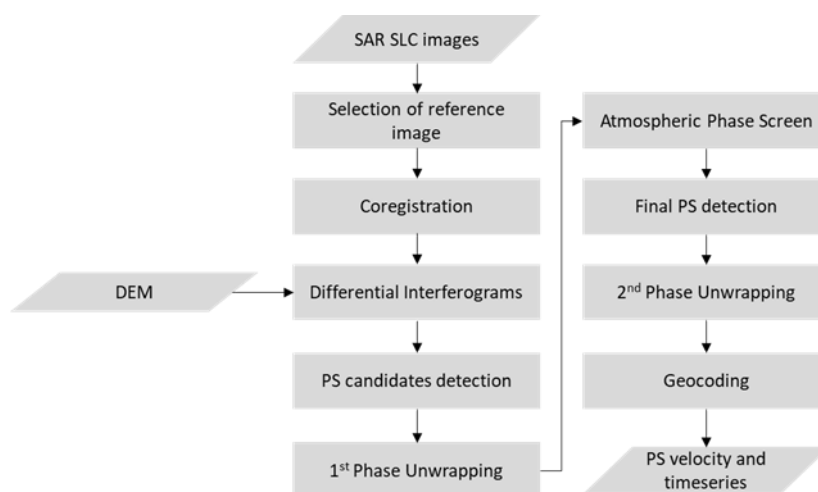


Figure 2.3: Generalized PSI Workflow

2.3.1 Interferometric processing

The interferometric processing in a PSI workflow is based on a stack of many SAR images (ranging from ~20 images to hundreds of images) covering several years. It starts with a selection of a reference SAR image. The selection of the reference image aims to maximize the average coherence by minimizing the geometrical- and temporal- baseline dispersion (Ferretti et al., 2021):

$$\max_i \left\{ \sum_{j=1}^N \left(1 - \frac{|B_g^{ij}|}{B_{\perp,crit}} \right) \cdot e^{-|B_t^{ij}|/\tau} \right\}$$

With B_g^{ij} and B_t^{ij} are the geometrical- and temporal- baseline of the interferogram based on SAR image i and j , $B_{\perp,crit}$ is the critical geometrical baseline and τ is a temporal decorrelation constant. When the critical baseline is reached, the phase decorrelates completely due to the loss of spectral overlap. The critical baseline for flat areas can be calculated by (Li and Goldstein, 1990):

$$B_{\perp,crit} = \frac{\lambda r_0 \tan(\theta)}{\delta r}$$

With $B_{\perp,crit}$ is the critical geometrical baseline, λ is the wavelength, r_0 is the slant range distance, θ is the incidence angle, δr is the slant range resolution. For Sentinel-1 it ranges between ~4 km - ~7 km. Taking into account the small geometrical baseline of the Sentinel-1 mission (rms of the diameter of the orbital tube: 100 m, Torres et al., 2012) the System is one order of magnitude below the critical baseline.

After the selection of the reference SAR image, all secondary SAR images are coregistered to the reference SAR image. For Sentinel-1 the coregistration is based on the enhanced spectral diversity approach (Scheiber et al., 2000, Prats-Iraola et al., 2012), due to the high requirements regarding the azimuth coregistration accuracy of 1/1000 of a pixel.

Subsequently, $n-1$ interferograms are computed by multiplication of the single look complex (SLC) reference image with the complex conjugate of the secondary SLC images. The next step is the simulation and subtraction of the topographic phase contribution by using a digital elevation model (DEM). The topographic phase can be described by (Bamler and Hartl, 1998):

$$\Delta\Phi_{topo} = -\frac{4\pi}{\lambda} \frac{B^{\perp}}{r \sin \theta} \Delta h$$

With B^{\perp} is the geometrical perpendicular baseline, r is the slant range distance between the satellite and the Earth surface, θ is the incidence angle and Δh is the ellipsoidal height. After removing the topography related phase component, the interferogram is called differential interferogram. The stack of differential interferograms are the basis for the following PSI processing steps.

2.3.2 PS detection

Based on the stack of SAR images the PS pixels are detected. Therefore, the temporal stability of the SAR amplitude is used. The rationale is the use of the temporal stability of the radar cross section of a backscattering object as a proxy for phase stability. Usually, the amplitude dispersion index (Ferretti et al., 2001) or the signal-to-clutter ratio (SCR, Adam et al., 2005) is used for this purpose. The amplitude dispersion index estimates the clutter from the amplitude dispersion of a single resolution cell over time. The SCR method infers the clutter from a spatial window around a resolution cell for every SAR image individually and then computes the average over time to detect the PS. Both methods are based on the same signal model which assumes additive complex circular Gaussian noise affecting the SAR signal. A resolution cell is considered to contain a PS if the power of the clutter is much lower than the power of the signal.

2.3.3 Phase unwrapping

Based on the phase values of the detected PS the deformation rate and the residual height are estimated. Usually, the estimation is based on a constant velocity model on phase variations between neighboring PS pixels. The assumption is that the impact of atmospheric phase contributions is very similar in neighbouring pixels and thus, cancels out in the difference. The estimation can be performed by using a periodogram solver which can be described by (Ferretti et al., 2001):

$$\arg \max_{\Delta q, v} \left\{ |\gamma| = \left| \frac{1}{K} \sum_{k=1}^K e^{j\varphi k} \cdot e^{-j(C_q B_K \Delta q + C_v T_k \cdot v)} \right| \right\}$$

With Δq is the residual height, v is the linear deformation rate, γ is the coherence, K are the differential interferograms, φk is the phase value of the differential interferogram K , $C_q = \frac{4\pi}{\lambda R} \sin \alpha$, B_K is the geometrical baseline, $C_v = \frac{4\pi}{\lambda}$ and T_k is the temporal baseline. Thus, the unknowns Δq and v are estimated by maximizing the coherence γ for each PS pixel. After the ambiguity of the phase variation between neighboring PS are resolved the phase data is integrated. Therefore, several algorithms based on e.g. region growing, L^p-norm optimization, graph Theory or network flow can be used (Costantini, 1998, Ferretti et al., 2007). All these global optimization processes assume a single PS with no deformation and residual height. This PS is called PS reference point and all estimated deformation rates and residual heights are relative to this PS.

For short distances, the assumption that the atmospheric phase contribution is similar and therefore cancels out is in general valid, but on larger distances (e.g. > 5 km) it is not valid (Adam 2019). Therefore, the atmospheric phase contribution, also called atmospheric phase screen (APS), should be mitigated for every interferogram in order to achieve high precision estimates over larger distances (e.g. hundred km). The APS can be differentiated into ionospheric-, tropospheric turbulence- (wet delay) and tropospheric stratification- (dry delay) effects (Hanssen 2001, Adam 2019). The ionospheric effect is most strongly in SAR Systems with long wavelengths (e.g. L-Band), but have a limited impact shorter wavelengths (C- and X-Band) and mid-latitudes. It can be modelled by e.g. low order polynomials. The wet delay is

caused by the variability of the water vapor density in the troposphere. The spatial correlation length of the wet delay can vary from one to ten km. The dry delay is caused by the variability of the refraction indices at different elevations. The effect is often present in mountainous regions and is correlated to topography. Therefore several authors proposed methods to mitigate the dry delay, e.g. based on a power-law relationship (Bekaert et al., 2015b). The APS can be estimated from the statistics of the phase values at the PS (Ferretti et al., 2001). In addition, external data from e.g. numerical weather models can be used to further mitigate the APS (Adam 2019).

After the APS of every differential interferogram has been mitigated the PS detection and phase unwrapping is performed again to estimate the deformation rates and residual heights with high precision. Thus, a final PS detection and 2nd phase unwrapping is performed (Fig. 2.3).

It should be noted that, due to the ambiguity of the phase the maximum detectable deformation between two PS and two acquisitions is $\lambda/4$ (Crosetto et al., 2015). Thus, in theory, the maximum measurable differential deformation rate of Sentinel-1 (considering wavelength and revisit time) is 42.6 cm per year with a 12 day revisit time (e.g. only Sentinel-1 A) or 85.2 cm per year with a 6 day revisit time (e.g. Sentinel-1 A/B). In practice, the capability to detect fast displacements depends on various aspects, e.g. the noise level of the data, the specific phase unwrapping technique, the spatial pattern of the deformation phenomena (the smoother the pattern, the better) and the PS density over this phenomena (the higher the density, the better) (Van Leijen, 2014).

2.3.4 Geocoding

The last step of the PSI processing is the projection of the PS from SAR image coordinates (range, azimuth) to a geographic coordinate system (e.g. WGS84 with latitude, longitude, height). The projection is performed based on the orbital data of the reference SAR image, range and azimuth coordinates and the estimated height of the radar target (Ferretti et al., 2007).

2.4 Landslides

Landslides can be defined as mass movement of a mass of rock, debris or earth down a slope (Cruden, 1991). Varnes (1978) proposed a landslide classification according to the type of movement (falls, topples, slides, lateral spreads, flows) and type of material (rock, debris, earth). In addition, a combination of two or more movement- and material- types is classified as complex. A classification according to the landslide velocity is given by Cruden (1995) and covers ten orders of magnitude (Tab. 2.4.1).

Table 2.4.1: Landslide velocity classification (Cruden, 1995)

Description	Velocity limits
Extremely rapid	$>5 \text{ m s}^{-1}$
Vary rapid	$>3 \text{ m min}^{-1}$
Rapid	$>1.8 \text{ m h}^{-1}$
Moderate	$>13 \text{ m month}^{-1}$
Slow	$>1.6 \text{ m year}^{-1}$

Very slow	>16 mm year ⁻¹
Extremely slow	<16 mm year ⁻¹

From this large variety of velocities the PSI technique can detect only very slow to extremely slow moving landslides. E.g. the theoretical maximum detectable velocity, considering the SAR wavelength and revisit rate of Sentinel-1, is 42.6 cm a⁻¹ (Crosetto et al., 2015). Causes of landslides can be differentiated into three categories (USGS, 2004):

- Geological (e.g. weathered materials, bedding, contrast of permeability)
- Morphological (e.g. fluvial erosion of slope toe, deposition loading slope)
- Anthropogenic (e.g. excavation of slope, irrigation, artificial vibration)

The three main triggering processes of landslides worldwide are:

- Slope saturation by water
- Seismic activity
- Volcanic activity

E.g. the triggering process “slope saturation by water” can happen due to intense rainfall, snowmelt, changes in ground-water level and water level changes along e.g. rivers, lakes, coastlines (USGS, 2004). A high level of water saturation at the sliding surface can cause an acceleration of the landslide deformation by decreasing the friction coefficient. Therefore, several authors have studied the correlation of currently active landslide deformation with potential triggering factors like precipitation as a proxy for slope saturation by water.

Active landslides are those, which are currently moving or suspended. Suspended refers to landslides which are currently not moving, but have moved in the last cycle of seasons (Varnes, 1978). If no evidence of movement is present within the last cycles of seasons, a landslide is considered as inactive. These inactive landslides can either be dormant, fossil or ancient. Dormant landslides have the potential of reactivation, because the causes of failure still exist. Fossil and ancient landslides cannot be reactivated at present, because they have developed, in general, under different morphological- and climatic- conditions.

2.4.1 Landslide mapping and monitoring based on A-DInSAR datasets

Regarding A-DInSAR based landslide mapping and monitoring three categories are proposed by Casagli et al. (2016):

- Landslide Inventory Mapping (LIM) for large areas covering a few thousand square kilometers
- Landslide Monitoring (LM) for single large landslides affecting built-up areas with a high risk level
- Rapid Landslide Mapping (RLM) carried out after an emergency for rapid mapping of pre-existing landslides with potential reactivations and new landslides

Landslide inventory maps provides information regarding e.g. spatial extent, type, date, state of activity, frequency of occurrence, causal factor, caused damage.

Righini et al. (2012) used ERS and Envisat PSI datasets to map the state of activity, geometry and to identify new landslides in the central-eastern part of Italy. The study area covered an area of 1,320 km² and PSI datasets were combined with optical imagery and ancillary data. The study identified 95 new landslides and ~9% of the pre-existing inventory were modified by the PSI datasets.

Cigna et al. (2013) proposes a PSI post-processing including a conversion of the PSI LOS vector into the slope direction and the application of thresholds regarding the PSI-derived mean velocity and a minimum number of persistent scatterers (PS) per landslide. In order to improve the criterion of a minimum number of persistent scatterers (PS) per landslide, Barra et al. (2017) uses a spatial clustering of PSs with similar velocities to detect deformation areas, e.g. in landslide areas.

Casagli et al. (2016) used ERS, Envisat, Radarsat, TerraSAR-X DInSAR and A-DInSAR datasets in combination with optical image analysis to perform LIM, LM and RLM. Two landslide inventory maps were produced (lower Austria/Austria and South Tyrol/Italy), two LM were performed (Lubietova/Slovakia and Kaohsiung County/Taiwan) and one RLM was performed (Abruzzo/Italy). The RLM resulted in 39% of updated landslides based on ERS, Envisat and Radarsat A-DInSAR datasets with respect to the pre-existing landslide inventory. 57 new landslides were detected in Abruzzo/Italy based on A-DInSAR datasets. These case studies demonstrate the potential of SAR/optical earth observation techniques for (rapid) landslide mapping and monitoring in different regions.

Rosi et al. (2017) updated an existing landslide inventory map from the early 2000. The inventory was updated with a PSI dataset covering the timespan 1992-2010 (ERS-1/2, Envisat). Results were analyzed to assess i) the geographical distribution, ii) the area-frequency distribution and iii) the geological-/geomorphological- properties of landslides.

While the focus of these studies (Righini et al., 2012, Cigna et al., 2013, Casagli et al., 2016, Rosi et al., 2017) was mainly on the A-DInSAR mean velocity and the corresponding spatial distribution, another group of studies focuses on the information present in the A-DInSAR deformation time series. E.g. Berti et al., (2013) uses a sequential series of statistical tests to classify PS time series into pre-defined classes. Chaussard et al. (2014) proposes a temporal mode principal component analysis (PCA) to compute a set of uncorrelated principal components. The use of independent component analysis (ICA) to maximize the statistical independence of an arbitrary number of independent components is proposed by Cohen-Waeber et al. (2018). Other approaches are, e.g., the inverse velocity approach to estimate the time of slope failure (Carlà et al. 2019), wavelet analysis to quantify and correlate (intermittent) periodical signals (Haghshenas and Motagh 2016, Tomás et al. 2016, Liu et al. 2022). In general, these studies uses a wavelet analysis to correlate (intermittent) periodical signals of A-DInSAR deformation time series with precipitation measurements (as potential landslide triggering factor).

3 Scientific Contributions

3.1 Introduction

The invention of advanced InSAR techniques, PSI (Ferretti et al., 2001) and Small Baseline Subset (Berardino et al., 2002) creates the possibility to detect mm-scale deformations of the Earth's surface for thousands of measurements points. Since these inventions numerous scientific studies has proven the operational readiness of this techniques. However, the analysis was restricted to the relatively small SAR image footprints (e.g. ERS-1/2 images have a footprint size of 100 km x 100 km) and non-complete coverage. This has changed completely since the launch of the Copernicus ESA Mission Sentinel-1 in 2014. The standard acquisition mode over land areas of Sentinel-1 has a swath wide of 250 km and even more important a complete coverage of the entire land areas of the Earth. Together with these technical specifications comes a long-term mission design and a free, full and open data policy. These characteristics of the Sentinel-1 mission opens the possibility to routinely map and provide end-users (e.g. responsible authorities) surface deformations for entire nations and even continents.

This chapter provides the scientific contributions of this thesis which can be differentiated in i) the creation of a concept for an operational Ground Motion Service for Germany based on nationwide Sentinel-1 PSI data and ii) investigate in several post-processing techniques to semi-automatically extract relevant information regarding landslide applications (LIM and LM) from PSI datasets.

3.2 Challenges for a nationwide InSAR based Ground Motion Service

Various challenges has to be addressed for a nationwide GMS based on A-DInSAR. At first a decision has to taken, which advanced A-DInSAR techniques technique should be used for a nationwide GMS. In principle, when using A-DInSAR a trade-off between measurement precision and measurement point density exists. The reason is the lower noise level, but also lower measurement point density of Persistent Scatterers compared to Distributed Scatterers. Therefore, a decision which A-DInSAR technique is going to be used has to be taken, e.g. PSI or SBAS.

A second challenge is the relative nature of all A-DInSAR techniques. By increasing the distance to the reference point the precision decreases due to error propagation caused by e.g. residual atmospheric contributions. This characteristic becomes relevant for nationwide A-DInSAR datasets because of the large area that has to be covered (e.g. Germany: ~360,000 km²). It is relevant for a single Sentinel-1 image stack due to the large image footprint (swath wide: ~250 km) and across adjacent Sentinel-1 image stacks (six descending- and ascending-tracks resliced into 65 descending- and 59 ascending- stacks, Kalia 2022). Usually, a linear trend or higher order polynomials are applied to mitigate the long wavelength error.

A third challenge is the difficulty when the estimated deformation rates and time series are going to be used with other independent deformation measurements (e.g. from levelling). The difficulty is caused by a different datum definition of the A-DInSAR results and other measurement techniques. Therefore, a common datum definition is required to ensure the interoperability of different measurement techniques (Del Soladato et al., 2021b).

3.3 Contributions for a nationwide InSAR based Ground Motion Service

In order to decide which advanced InSAR technique should be used for the Ground Motion Service Germany (BBD) the end-user requirements were collected in several user workshops and national Copernicus Fora. The result was that precision was of highest priority for the German user community. Therefore, the PSI technique was chosen and a case study based on a wide-area ERS-1/2 PSI processing was performed as a proof-of-concept. The case study showed a high precision of the deformation rate estimates, while at the same time covering a large area (~ 30,000 km²). In order to assess the precision GNSS time series were compared against the wide-area ERS-1/2 PSI dataset.

In order to ensure the interoperability of the PSI dataset a calibration based on GNSS time series is demonstrated in the ERS-1/2 PSI case study and subsequently realized in the nationwide Sentinel-1 PSI datasets. After calibration, the PSI deformation rates and time series are relative to a well-defined GNSS derived reference frame. Another benefit from the GNSS calibration is the complementary nature with regards to PSI. PSI derived deformation rates with low spatial frequency (e.g. caused by tectonic processes) can be mistaken with phase artefacts (e.g. from residual APS). On the other hand, PSI provides very high measurement point densities compared to GNSS and high precision on local scales. GNSS in turn provides a low measurement point densities (approximately 250 permanent GNSS stations across Germany) but a high precision regarding large scale deformations. By performing a GNSS calibration the benefits of both techniques, the high measurement point density and high precision on local scales from PSI and the high precision on large scales from GNSS are combined.

In order to provide nationwide consistent PSI datasets to the end-users the PSI results from adjacent image stacks are mosaicked. This was demonstrated in the ERS-1/2 case study and subsequently realized in the nationwide Sentinel-1 PSI LoS datasets. The mosaicking process starts with the calculation of the offset of the PSI deformation rates in all overlapping areas (excluding deformation areas). Based on these offsets a bundle block adjustment was performed to reduce the offsets between adjacent Sentinel-1 image stacks. The adjusting parameters are applied to the velocity field and the deformation time series.

3.4 Challenges in PSI based landslide applications

Several methodologies have been proposed to extract relevant information from PSI datasets. These methodologies are usually focusing on the detection of spatial deformation clusters (Barra et al., 2017, Festa et al., 2022, Confuorto et al. 2022) or temporal deformation patterns (Berti et al., 2013, Chaussard et al. 2014). Only few studies use a combined approach to extract spatial- and temporal- patterns. To the authors knowledge no such study has been performed on nationwide A-DInSAR datasets.

With respect to the kind of information that is semi-automatically extracted from A-DInSAR datasets a specific application has to be in focus. In this thesis, landslides in rural areas with relatively low PS densities are investigated. The rural landcover makes it a challenging application example for a nationwide A-DInSAR dataset. On the other hand, it is a relevant application because of damages to buildings and infrastructure are present and in-situ measurements are only sparsely available for specific landslides. To the authors' knowledge no

scientific study has been performed in Germany to investigate in (semi-) automatic information extraction based on A-DInSAR datasets for landslide applications on a regional scale. In addition, to the authors' knowledge, the time-lag between rainfall and landslide deformations which is of relevance in order to understand the triggering mechanism (Liu, 2022), has not been studied in this area.

3.5 Contributions to PSI based landslide applications

In this thesis, distance- and noise- thresholds are proposed for the semi-automatic detection of spatial clusters of moving PS on a regional scale. The thresholds are adapted for the characteristics of the nationwide S-1 PSI dataset of the GMS Germany. Based on the detected deformation clusters a classification of the landslide state of activity is performed on the regional scale (1,500 km²). Results are verified based on GNSS time series measurements, ground-truth and a regional scale landslide hazard indication map. The measurement precision w.r.t. GNSS time series at corner reflectors is 2σ mean LoS velocity = ± 0.37 mm a⁻¹, the thematic classification results could be successfully verified by field surveys and ancillary thematic data. To the authors knowledge, this is the first time the clustering algorithm (local Moran's Index) is used for PSI based landslide applications.

A second contribution to the research field of PSI post processing are time series analysis in combination with ancillary thematic information (meteorological measurements). Therefore, the time-lag between a potential triggering factor (climatic water balance) and the PSI velocity is estimated. This is done for a single PS regarding an individual acceleration event and a seasonal periodical deformation signal. In both cases, a time lag between PSI deformation signal and climatic water balance is estimated. Results are verified by a second PS deformation time series at the similar spatial location but from a second S-1 PSI image stack. While the approach to estimate the periodical signal delay could be successfully verified, the approach for the delay estimation of the acceleration event could not be verified. To the authors' knowledge, this is the first time the time-lag between climatic water balance and A-DInSAR based landslide deformation time series has been studied.

4 A Copernicus downstream-service for the nationwide monitoring of surface displacements in Germany

This chapter was published as:

Kalia, A. C., Frei, M., Lege, T. (2017): A Copernicus downstream-service for the nationwide monitoring of surface displacements in Germany, *Remote Sensing of Environment*, Volume 202, p. 234-249, ISSN 0034-4257, <https://doi.org/10.1016/j.rse.2017.05.015>

Contribution statement

Andre C. Kalia did the conceptualization, which includes the research ideas and the formulation of the overarching research goals. He did the writing of the initial draft manuscript, respond to the reviewer comments and writing of the final manuscript. He did the investigation process by data collection and subsequent analysis of the experimental results. He created the visualizations of the published work. Michaela Frei and Thomas Lege had the leadership responsibility for the research activity and reviewed and commented the draft manuscript. German Aerospace Center (DLR) was contracted for interferometric SAR processing.

4.1 Abstract

Advanced interferometric SAR processing techniques (Persistent Scatterer Interferometry, Small Baseline Subset) are able to detect and monitor various surface displacements caused by e.g. gravitative mass movement, subsrosion, groundwater extraction, fluid injection, natural gas extraction. These processes can e.g. cause damage to buildings and infrastructure, affect ecosystems and agriculture or affect the economic use of the geological underground by influencing the hydrogeological setting. Despite the maturity and operational readiness of the PSI technology it is rarely used in operational workflows of the German user community (e.g. from responsible authorities).

In order to support the operational use of this technique a “Ground Motion Service Germany” has been designed by the Federal Institute for Geosciences and Natural Resources (BGR) in collaboration with the user community, land surveying agencies, SME and research institutions. A major outcome of this collaboration is the user request regarding a PSI-WAP (Persistent Scatterer Interferometry Wide-Area-Product) dataset of the entire nation (approx. 360,000 km²) based on Sentinel-1 data. For this reason the PSI mapping coverage is increased by mosaicking PSI data products from adjacent SAR data stacks. Several case studies has been performed to demonstrate the design of the service. Within this paper one case study regarding the PSI-WAP technique and the calibration/validation scheme is presented. The pilot study is focusing on the built up of an officially approved PSI-WAP dataset. The study area covers an area of 30,000 km² and is located in the Northwest German Basin. This is the first time a PSI-WAP analysis is performed in this area. Several natural processes (e.g. compaction of marine sediments, peat growth/shrinkage) and anthropogenic activities (e.g. natural gas extraction, rock salt mining) are causing surface displacements in the study area. The PSI-WAP analysis is based on six adjacent ERS-1/-2 data stacks covering the timespan from 1992 until 2001. Each data stack consists of 49 to 73 acquisitions. A comparison of the PSI results with thematic data (e.g. cumulated volume of extracted natural gas and location of natural gas fields) indicates that a part of the detected land subsidence is caused by natural gas extraction. To summarize, this paper shows i) the design of the “Ground Motion Service Germany” and ii) a pilot study to exemplarily demonstrate a PSI-WAP, the calibration/validation scheme and value-added-products.

4.2 Introduction

It is clear, that fast surface displacements due to earthquakes or landslides are geohazards. But also relatively slow surface displacements can cause damage to buildings and infrastructure, influence the hydrogeological setting or increase the vulnerability of flooding in coastal lowlands. Slow displacements can even be a precursor to fast movements or an indicator for looming earthquakes (Bekaert et al., 2015). Mass movements can even lead to loss of live. In order to mitigate these hazards, accurate information regarding the displacement of interest are mandatory. Surface displacements phenomena are mainly detected and monitored by geodetic techniques (optical leveling campaigns, tilt meters, GNSS). Spaceborne SAR-Interferometry (InSAR) is gaining increasing attention because of its unique characteristics (large spatial coverage, dense sampling grid, high temporal measurement density, independence of accessibility). InSAR has been used to detect surface displacements of the earth surface since

>20 years (Massonnet et al., 1993) and reached maturity in recent years (Adam et al., 2009). Advanced interferometric SAR processing techniques, e.g. Persistent Scatterer Interferometry (PSI) (Ferretti et al., 2000, 2001, Kampes and Adam, 2003, Werner et al., 2003), Small Baseline Subset (SBAS) (Berardino et al., 2002, Lanari et al., 2004) or combinations of PSI and SBAS (Ferretti et al., 2011, Hooper, 2008) allow the detection of surface displacements with a high precision in the order of mm per year. In this manuscript, the term Advanced DInSAR (A-DInSAR) technique is used as a generic term to summarize these sets of techniques. Several studies have shown the successful measurement of surface deformation and mass movements by using A-DInSAR techniques for e.g. landslide (Calò et al., 2014, Del Ventisette et al., 2014, Notarnicola et al., 2014), coastal subsidence (Gruijters and van der Krogt, 2013), karst processes (Chang and Hanssen, 2014, Galve et al., 2015), ground water overexploitation (Tomás et al., 2010), mining (Abdikan et al., 2013, Guéguen et al., 2009), natural gas production (Chaussard et al., 2013, Ketelaar, 2009), geothermal energy production monitoring (Lubitz et al., 2013, Lubitz et al., 2012) or earthquake induced displacements (Bekaert et al., 2015, Kobayashi et al., 2015). Depending on the application, the range of velocities and spatial extent varies strongly (mm/year to m/month, hundreds of m² to hundreds of km²). Modern SAR sensors like Sentinel-1 A/B (S-1) (Torres et al., 2012) can provide precise phase measurements with large coverage (250 km wide swath) while preserving a spatial resolution of 5 × 20 m (Interferometric Wide Swath mode, IW). Very high spatial resolution SAR data are provided by e.g. the TerraSAR-X (Werninghaus, 2004) or Cosmo-SkyMed (Covello et al., 2010) missions (3 × 3 m with the Stripmap mode), but with smaller coverage (swath width 30 km). All mentioned SAR missions offer a fast revisit cycle (6-, 11- and 4-days respectively) which is mandatory for the monitoring of fast non-linear displacements (e.g. landslides). Furthermore, the high repeat cycle enables the fast buildup of image stacks, which are required for e.g. the PSI technique. S-1 is designed as a “mapping mission” providing complete coverage in particular over Europe, every 6 days. With a PSI analysis based on S-1 IW datasets, an operational nationwide surface displacement monitoring (millions of PS – Persistent Scatterer with mm a⁻¹ precision) becomes technically feasible.

The demand for operational InSAR based surface displacement products and in particular a German nationwide surface displacement monitoring product was articulated by the German national user community during so called “National Fora” in 2011, 2012, 2014 and 2015 (DLR, 2016). Several EU projects were aiming at the creation of user-driven products based on A-DInSAR analysis, e.g. ESA-TerraFirma (2003 – 2012) (Adam et al., 2009), EU-FP7-PanGeo (2011–2014) (Capes, 2012) and EU-FP7-SubCoast (2010–2013) (Gruijters and van der Krogt, 2013). These projects established product standards based on user requirements and demonstrated the operational readiness of the PSI technique. A validation scheme of PSI processing and value added products was proposed by (Agudo et al., 2006) and (Adam and Kampes, 2008). This includes displacement products like the geocoding-, mean velocity accuracy and quality control aspects during interferometric SAR processing like missing lines check of the SAR imagery.

Based on the requirements of numerous stakeholders of the German user community and the operational readiness of the A-DInSAR techniques a “Copernicus downstream-service for the nationwide monitoring of surface displacements in Germany” is designed by the Federal Institute for Geosciences and Natural Resources (BGR). Copernicus (before 2012 called GMES, Global Monitoring of Environment and Security) is the European Earth Observation program coordinated by the EC (European Commission) in collaboration with the ESA

(European Space Agency), EUMETSAT (European Organization for the Exploitation of Meteorological Satellites), ECMWF (European Centre for Medium- Range Weather Forecasts), EEA (European Environment Agency) and Mercator Ocean. Copernicus aims at the support of European environmental, climate and security policies (EC, 2013). It provides information products for public policy makers (e.g. atmosphere monitoring service: European air quality, land monitoring service: CORINE land cover, emergency management service: burnt area map, flooded area map) based on remote sensing and in-situ data. As an extension of these European Copernicus core services a national Copernicus downstream service regarding A-DInSAR based information products to monitor surface displacements is requested by the German national user community (government agencies, public authorities, industry and general public).

This manuscript outlines the concept for a Copernicus downstream service (Fig. 2) with standard and value added products of different Levels (L). In order to demonstrate the feasibility and usability of the standard level 2A Product (L2A), results from ERS-1/2 based PSI-WAP analysis are presented and discussed. Subsequently the L2A product is described from the processing, calibration/validation perspective. Furthermore, a potential level 3 (L3) product is presented. The conclusion focuses on potential challenges within the designed workflow and current applied research themes.

4.3 User requirements

User workshops and inter-ministerial meetings dedicated to the preparation of a national Copernicus service regarding displacement monitoring were performed in 2014 and 2015 by the BGR (Kalia et al., 2014, Lege, 2014, Kalia et al., 2016). End-users from German governmental agencies (e.g. state geological surveys, mining authorities and ordnance surveying), remote sensing experts/companies and researchers were participating at these workshops. Besides the identification of relevant displacement processes also technical aspects like the tradeoff between spatial measurement density vs. coverage or preferred data formats were discussed. In addition to these workshops, a user survey, based on a questionnaire, was performed in order to support the identification of required applications and rank the importance of specific data and processing characteristics. The user community identified ten displacement phenomena (Table 4.3.1).

Table 4.3.1: Surface displacement phenomena were identified by the user community

Crude oil and natural gas extraction/storage	Karst processes
(Abandoned) mining	Landslides
Groundwater extraction (management)	Coastal subsidence/sediment consolidation
Geothermal energy production	Salt tectonics/subrosion
Dewatering of organic soils	Settlement of infrastructure

These anthropogenic and natural displacement phenomena occur in spatial relation to the geological, hydrogeological, pedological, geomorphological setting and anthropogenic activities. Fig. 4.1 shows a nationwide generalized overview of areas with a potential occurrence of particular displacement processes where local/regional displacement areas might

appear. This nationwide overview shows e.g. the location of major natural gas reservoirs or carbonates and thus indicates areas with the potential of subsidence caused by natural gas extraction or karst processes. Fig. 4.1 highlights that regions, potentially affected by surface displacements, are located throughout Germany. However, some processes are clustering in certain areas of Germany, e.g. subsidence caused by natural gas extraction, salt tectonics, dewatering of organic soils is mostly present in the North of Germany, while mass movements, karst collapse are mostly present in central and Southern Germany. In some regions, several displacement processes can be present at the same location, challenging a correct interpretation of the associated displacement process.

In order to cover all potential displacement areas in Germany, a nationwide map of surface displacements is requested by the national user community. Key user requirements are the consistency of the PSI-WAP dataset with other measurements (e.g. GNSS, leveling) and the reliability of the PSI-WAP dataset. Thus, the PSI processing chain as well as the calibration/validation workflow are important parts of the national Copernicus downstream service.

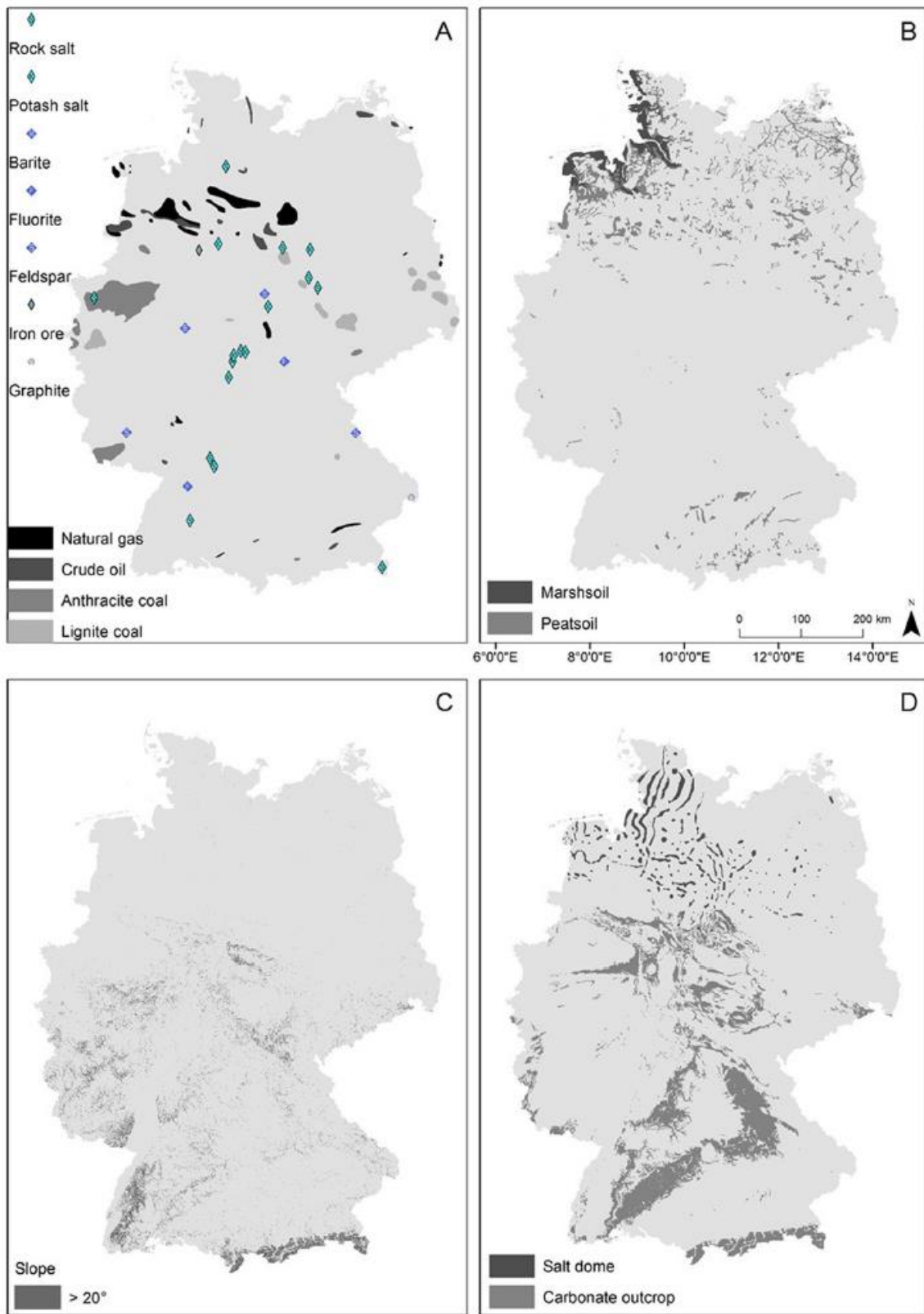


Figure 4.1: Indication of potential surface displacement areas caused by: mining activities (A), compaction of peat- or marsh soils (B), mass movements in areas with steep slopes (>20°) (C), subrosion related to carbonate rocks and salt structures (D) (data source: A: modified after (Lahner and Wellmer, 2004), B: modified after (Stange, 2007), C: modified after DGM10, BKG (2015), D: modified after (Toloczyki et al., 2006) and (Kockel et al., 2008)).

4.4 Ground Motion Service Germany

The Ground Motion Service Germany is based on the identified requirements of the German user community. Fig. 4.2 visualizes the generalized design of the service. The service is based on two displacement data categories:

- nationwide PSI-WAP dataset → Level 2A (L2A) and
- local/regional A-DInSAR datasets → Level 2B (L2B).

L2A will provide a German wide PSI-WAP map, while L2B will provide surface displacement measurements of specific areas with high spatial resolution to enable the monitoring of small-scale displacements. The PSI-WAP is a PSI product with a coverage of more than one SAR frame. Several PSI datasets are mosaicked and GNSS calibrated to produce a consistent and interoperable dataset. A L2B dataset will be produced upon specific user request (subsequent satellite tasking, combination with other data), while the L2A dataset will be routinely produced by the Ground Motion Service Germany.

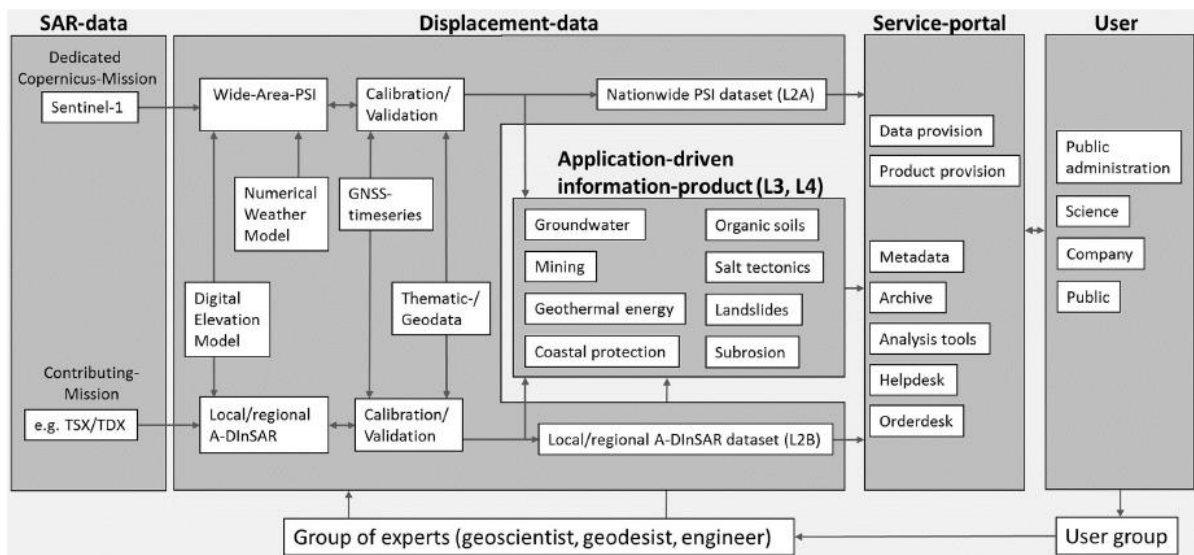


Figure 4.2: Workflow of the Ground Motion Service Germany for the monitoring of surface displacements in Germany.

The L2A dataset will cover the entire landmass of Germany and will provide the mean velocity (including standard deviation), the displacement time series and the location (latitude, longitude, height) for each PS. Based on the L2A and L2B datasets the production of application-driven information-products will be conducted. These value-added products (L3, L4) are driven by the application focus, e.g. the surveillance authority of mining activities is interested where the outer border of a subsidence area related to mining is located in order to assess the area of influence caused by this anthropogenic activity. The L3 product categories are referring to a combination with thematic data (e.g. mining areas) (L3) or to geophysical modeling (e.g. natural gas reservoir characteristics) (L4) (Fig. 4.3). The L3, L4 products are developed for multiple applications during the built-up of the nationwide PSI-WAP dataset together with ongoing pilot studies.

The displacement data (L2A/L2B datasets) as well as the products (L3, L4) will be provided via a web-based service-portal to the user community. Within this service-portal, the Nationwide PSI-WAP dataset (L2A) and comprehensive metadata, analysis tools, a helpdesk and an order desk will be present. The metadata include processing and validation reports. The analysis tools consist of e.g. interactive plotting functions of groups of PS time series. The helpdesk involves interpretation tutorials or user fora.

In order to constantly adapt the displacement-data (L2A, L2B) and the information-products (L3) to the user requirements, the built up of an advisory board and blogs is envisaged in order to provide advice to the service providers regarding A-DInSAR processing (L2A, L2B) and value-adding providers regarding required thematic products (L3, L4).

The L2A dataset will be the basic displacement dataset of the Copernicus downstream service, therefore it is described in more detail in the following chapter.

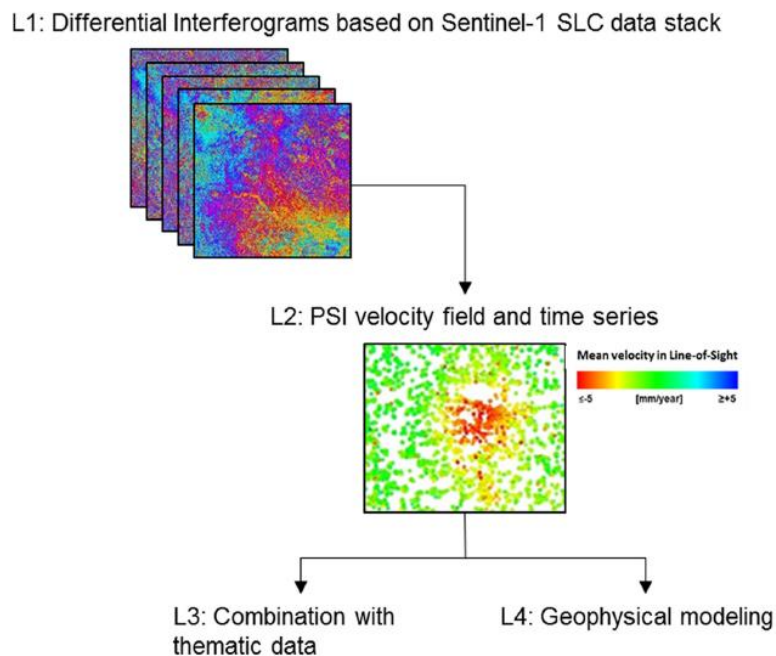


Figure 4.3: Simplified overview regarding the creation of Level 3 and Level 4 Products (L3, L4).

4.5 The L2A PSI-WAP dataset

The L2A PSI-WAP dataset is a consistent, German-wide, validated PSI-WAP dataset. It covers the entire land territory of Germany, which is an area of approximately 360,000 km².

This chapter introduces the SAR data, upon the L2A dataset are based, the interferometric processing chain and the GNSS calibration/validation workflow. In order to demonstrate the workflow an example from a pilot study is presented.

The L2A product will be based on C-band (wavelength of 5.6 cm, frequency of 5.405 GHz) SAR imagery from the Sentinel-1 mission (operated by ESA). The Sentinel-1 mission is a

constellation of two identical satellites (Sentinel-1A and Sentinel-1B). Sentinel-1A was launched on April 3, 2014 and has entered the operational phase in June 2015 (ESA, 2015). Sentinel-1B was launched on April 25th, 2016 (ESA, 2016). Both satellites are designed for an operational lifetime of seven years (consumable for 12 years). The subsequent SAR missions (Sentinel-1C and Sentinel-1D) are currently under development, however they will provide long-term data availability for the Copernicus program. The revisiting time with the constellation of two satellites, separated in orbit by 180°, is six days and thus allows a fast buildup of data stacks required for PSI analysis. Moreover, it will support the detection of fast non-linear displacements. For comparison, the maximum differential deformation rate measurable is 14.7, 25.7, 42.6 and 46.8 cm/year for Envisat-ASAR, TerraSAR-X, Sentinel-1 and ALOS-Palsar respectively (considering wavelength and revisiting time) (Crosetto et al., 2015). These are theoretical values, in practice, the capability to detect fast displacements depends on various aspects, e.g. the noise level of the data, the specific phase unwrapping technique, the spatial pattern of the deformation phenomena (the smoother the pattern, the better) and the PS density over this phenomena (the higher the density, the better) (Van Leijen, 2014, Crosetto et al., 2015). The spatial resolution of Sentinel- 1A/B is 5 (range) × 20 (azimuth) m in the default acquisition mode for land observations (Interferometric Wide Swath mode, IW) (Torres et al., 2012). The Sentinel-1 swath width in IW mode is 250 km (for comparison e.g. TerraSAR-X Stripmap mode: 30 km). An innovative acquisition technique called TOPSAR (De Zan and Monti Guarnieri, 2006) is used for this reason. The tradeoff is that the azimuth resolution worsens compare to equivalent Stripmap images. The German nationwide coverage will be achieved by using 24 IW frames from five partly overlapping tracks (Fig. 4.4). Within the overlap areas the PS density is increased because of the different acquisition geometry causing different effective scattering centers and thus different PS locations. 74% of Germany are observed by two adjacent tracks in ascending orbit, respective 77.8% in descending orbit (Table 4.2).

Challenges of the L2A dataset with respect to the Ground Motion Service Germany are missing IW acquisitions leading to missing data within the SAR time series. Although the IW mode is the standard acquisition mode of Sentinel-1 above land areas e.g. the Stripmap mode can be activated by Copernicus core services in case of e.g. hazardous flooding events, or the Extra Wide swath mode (EW) which is used off-shore for e.g. sea-ice monitoring in the North Sea and the Baltic Sea can cause acquisition gaps in the coastal regions. The different acquisition modes are not compatible for interferometric processing and thus a realization of a six day repeat cycle, using IW mode over land is crucial for the Ground Motion Service Germany due to the users requirements (detect fast non-linear deformations, high accuracy of the PS velocity).

A repeat cycle of six days will produce a significant amount of Sentinel-1A/B SAR-data. 24 standard IW frames are required to achieve a complete coverage of Germany. Considering VV polarized data, an oversampling factor of two in range and in azimuth direction, ascending and descending orbits the Single Look Complex (SLC) data volume will be >43.6 TB per year.

The standard dataflow from the Sentinel-1 satellite to the users is as follows. The SAR-data are transmitted from the Sentinel-1 A/B satellites to ESA's X-band core stations (Matera in Italy, Maspalomas in Spain and Svalbard in Norway) then transferred to the Processing and Archiving Centres (UK-PAC and DLR-PAC) where the raw data are processed to Level-1 products (e.g. SLC images) and then disseminated online to the users. This is done by the Copernicus Space Component (CSC) Data Access System operated by ESA and complemented by Sentinel

Collaborative Ground Segments (CollGS) on national level. The CSC Data Access System provides dedicated data access for Copernicus (core) services, scientific users, international users, CollGS users and users from ESA funded research and development projects. Within the Ground Motion Service Germany it is planned to access the raw data from DLR-PAC and produce consistent SLC images with one and the same S-1 Instrument Processing Facility (IPF) version. The motivation for this approach is that the SLC imagery currently provided in the CSC Data Access System was produced with different IPF versions, correcting different Elevation Antenna Patterns, which hamper the stacking of the SLC imagery.

Another challenge regarding the large data volumes is the interferometric processing itself and the production of updated PSI-WAP datasets. This challenge can be divided into two aspects, the first is the large data volume, the second is the non-linear complexity of many necessary processing steps (e.g. the spatial unwrapping). In order to handle the large data volumes the parallelization of algorithms and subsequent distributed computing (Casu et al., 2014, Zinno et al., 2016) are ongoing research topics. Concerning the processing complexity new strategies, e.g. a sequential estimator for distributed scatterer interferometry (Ansari et al., 2016) are ongoing research topics.

PSI processing

The basic principle of repeat pass interferometry is that the measured interferometric phase at a pixel in an interferogram is related to the distance differences between the effective scattering center and the SAR sensor between two successive acquisitions separated in time. The interferometric phase is measured as modulo 2π and thus it is ambiguous. Because the interferometric phase is not only related to surface displacements but also to e.g. atmospheric effects, the topography and the earth curvature, these phase contributions have to be estimated and subtracted from the measured interferometric phase to correctly estimate the displacement (Ferretti et al., 2000, Kampes, 2006). Moreover, the interferometric phase can only be successfully measured if the backscattered electro-magnetic signal remains correlated between the acquisition pair. Decorrelation can be due to e.g. temporal (large separation between the acquisitions in time), geometrical (large perpendicular baseline) and scattering effects (incoherent movement of individual scattering elements within a resolution cell) (Gatelli et al., 1994, Zebker and Villasenor, 1992). In order to overcome, or at least mitigate these drawbacks the PSI technique was introduced by Ferretti et al. (1999).

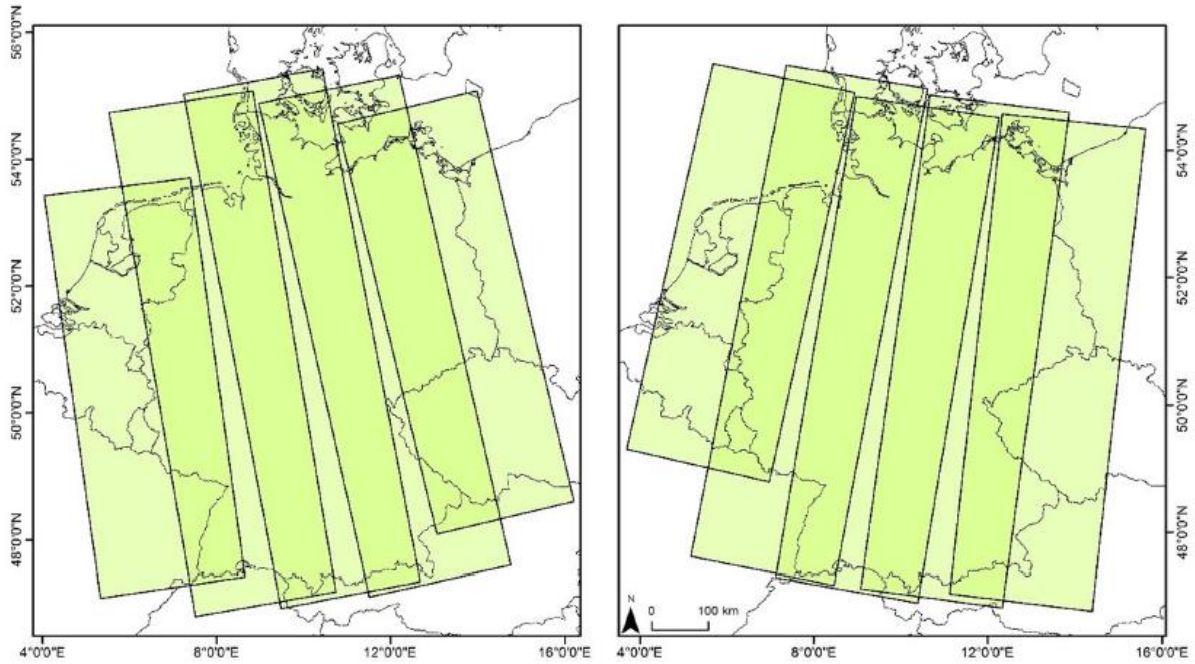


Figure 4.4: Sentinel-1 IW tracks required for complete coverage of Germany for ascending (A) and descending orbit (B). The green colors show coverage of the Sentinel-1 IW SLC data. Note that the amount of overlap between adjacent tracks is increasing towards the North because of the geometry of the near polar orbit.

Instead of analyzing single interferograms, formed by a single SAR acquisition pair, a stack of interferograms based on acquisition pairs covering a long period are computed and mutually analyzed. For this reason the interferometric phase of isolated long-time coherent point targets (so called Persistent Scatterer, PS) are analyzed. By using the statistical properties of the interferometric phase, in space and time, a separation of the interferometric phase contributions caused by atmospheric effects, surface displacements and topography is performed. This can be done by using e.g. the weighted integer least square estimator (Kampes, 2006). By using this approach, the PSs mean velocity, the displacement time series for each PS and the PS ellipsoidal height are estimated. Because of the phase ambiguity these estimates are all relative to one PS reference point (per data stack) characterized by a known mean velocity and height. The PS reference point is a highly time-coherent PS with a minimum phase shift, thus it is assumed that it is not affected by displacement (the PS height is extracted from an external DEM). PSs are often man-made features, thus the technique works best in urban (residential and industrial) areas because of the high density of usable PSs leading to a robust separation of the different phase contributions. The interested reader is referred to (Ferretti, 2014) for an application-oriented introduction into the PSI technique or to (Ferretti et al., 2000, 2001) for the algorithmic background of the PSI technique.

With the motivation to extend the PSI mapping area to rural areas several modified versions of the PSI technique were developed (Adam et al., 2013, Adam et al., 2011a, Adam et al., 2011b, Ferretti et al., 2011, Liebhart et al., 2012). The algorithmic improvements include, e.g. the detection and characterization of the PSs, the reference network setup and its robust inversion as well as the troposphere effect mitigation (Adam et al., 2011a).

Table 4.5.1: Size of the overlap areas per orbit over Germany.

Coverage	Ascending		Descending	
	Area [1000 km ²]	% of Germany	Area [1000 km ²]	% of Germany
1	92.92	26.0	79.31	22.2
2	264.45	74.0	278.05	77.8

The PSI technique was also modified in order to produce surface motion datasets covering areas larger than the extent of one SAR image. PSI datasets from several adjacent satellite tracks are mosaicked for this purpose. Thus, a consistent PSI dataset covering entire countries became realizable, the so called PSI-WAP. Note that no spatial averaging is performed and therefore the full spatial resolution as well as the high precision are preserved.

The processing workflow for the German-wide PSI-WAP map is visualized in Fig. 4.5. The workflow uses operational PSI mass processing techniques (intensively tested, robust algorithms, highly automated processing). In addition to standard PSI techniques two extra modules are used. First, the measurement precision is increased by a numerical weather forecasting model for estimation and removal of the atmospheric phase screen (APS) of each interferogram (Ulmer and Adam, 2015). Second, in a post-processing step, the relative PSI-WAP measurements are transformed into absolute measurements by a calibration based on continuous GNSS time series data (cGNSS).

Mosaicking

In order to produce a consistent PSI-WAP dataset covering the entire German territory PSI results based on several tracks are mosaicked. The mosaicking procedure consists of an independent detrending of the velocity field of each SAR frame and an offset calculation/adjustment of the velocity field of adjacent SAR frames. Detrending is necessary because current atmospheric models are not precise enough and therefore a residual tropospheric delay can be present in the velocity field (Fattahi and Amelung, 2015). First, a velocity field is fitted through the PS reference network points via singular value decomposition. Then the best fitting velocity field is subtracted from all PSs in order to get the detrended velocity field (Goel and Adam, 2015b). The detrended velocity field of each PSI result can still be affected by a constant offset, caused by an inappropriate (unstable) reference point, thus the offsets between the PSI results from adjacent tracks are calculated and subsequently adjusted with respect to a reference track. The offset of the velocity field is calculated in the overlap regions of the tracks using the median of difference of common reference network points, which are identified through a distance criterion (e.g. 20 m).

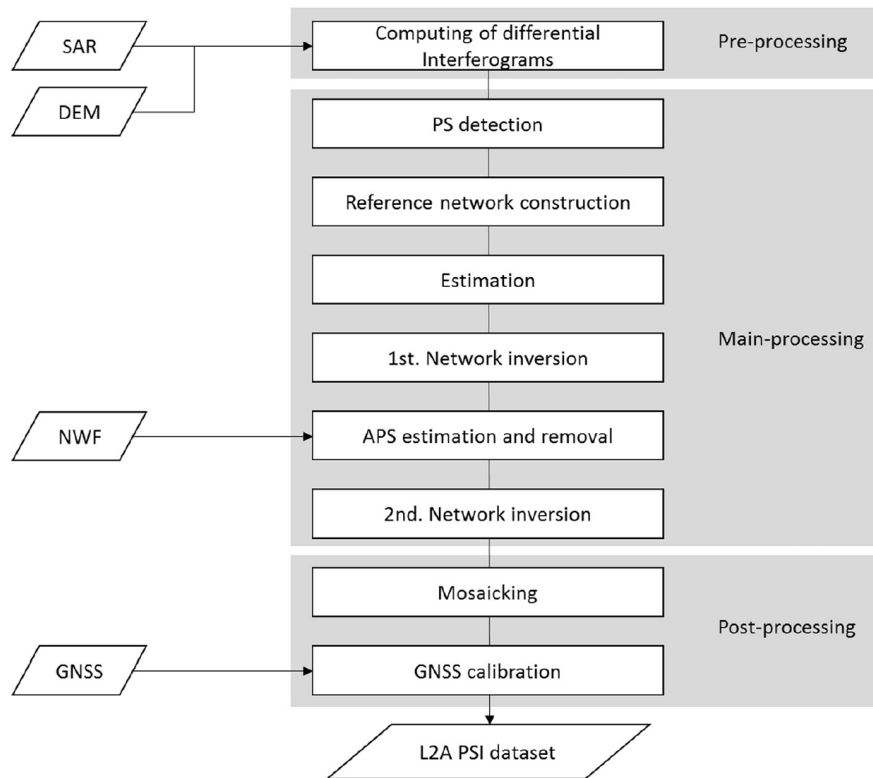


Figure 4.5: L2A interferometric processing workflow (modified after Adam et al., 2011a).

The incidence angles vary in the overlap area of adjacent tracks thus a projection of the LOS-velocities into vertical velocities is done to calculate the offset of the adjacent velocity fields. For this reason only PSs that are assumed to be stable ($\pm 0.5 \text{ mm a}^{-1}$) are projected from the LOS direction to the vertical direction and the differences are calculated. Then the differences of the vertical velocities are back-projected into the LOS directions and subsequently subtracted from the LOS velocities (Chang et al., 2016). Although the velocity offset is calculated within the overlap areas, it is valid for the whole frame because PSI is a relative measurement technique. In other words, if “stable” PSs in the overlap areas are affected by an offset, all PSs within a frame are affected by the same offset. Now all the LOS PS measurements are relative to one PS reference point of one master track.

But the mosaicked PSI-WAP result is not the final result yet. It still can't detect deformation phenomena larger than a SAR frame due to the ambiguity of e.g. deformations caused by tectonic processes with e.g. orbital ramps. However, large scale deformations, caused by e.g. glacial isostatic adjustment, are present in Germany and included in GNSS measurements (Steffen and Wu, 2011). Because the velocities of the PSI-WAP dataset must be comparable with other independent measurements (e.g. GNSS campaigns) an absolute calibration of the PSI-WAP dataset is mandatory.

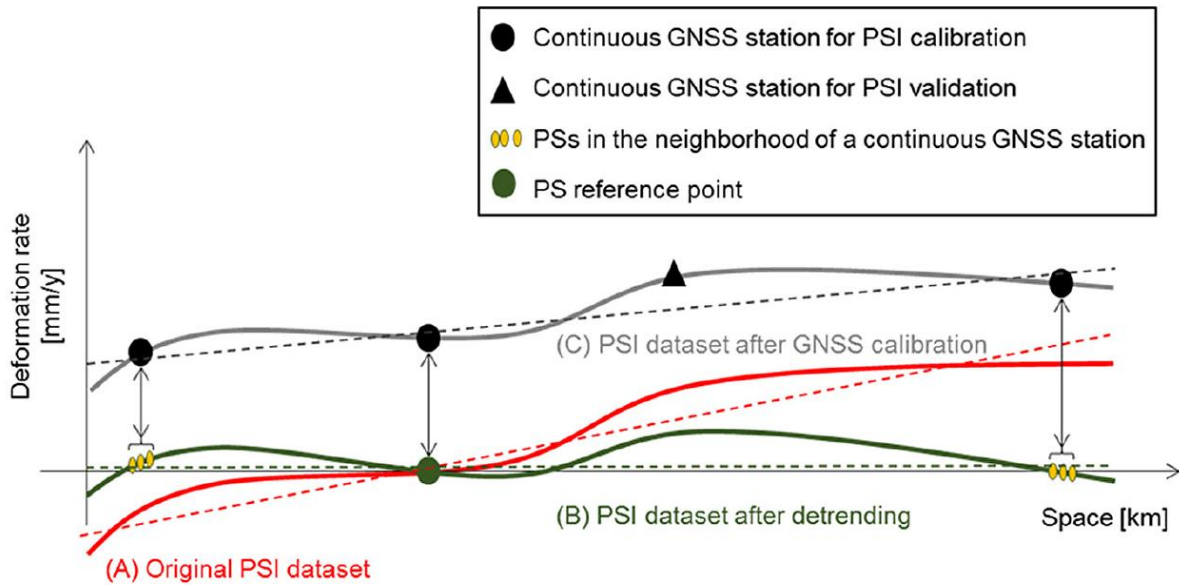


Figure 4.6: 2D geometry sketch regarding the GNSS calibration of the PSI mean velocity field. The original velocity field of the PSI dataset (A), after detrending (B) and the final velocity field after GNSS calibration (C). Only GNSS stations with adjacent PSs showing very limited displacements ($\pm 2 \text{ mm a}^{-1}$) are used for the calibration procedure. Source: modified after (Parizzi, 2015).

GNSS calibration

All PSs of the detrended and mosaicked PSI-WAP dataset are referring to a single PS reference point of the master track, which is assumed to be stable. If this assumption is not correct, an offset between the mosaicked dataset and the real velocity field occurs (Fig. 4.6). Furthermore, the PSI-WAP dataset has been detrended in order to mitigate possible large scale residual errors due to e.g. residual orbital or atmospheric errors. However, the detrending step also mitigates possible large-scale deformation phenomena, e.g. due to tectonic deformation processes (Lege et al., 2016). Both aspects, an inappropriate PS reference point (incorrect height and/or incorrect velocity estimates) and a large scale deformation, can cause a bias between the mosaicked PSI-WAP dataset and the real deformation. Thus a combination with other independent datasets can become problematic (GNSS, different SAR acquisition geometries, geoscience). For this reason, a calibration based on continuous GNSS time series data is performed. The term “absolute” and “relative” regarding GNSS and PSI-WAP, respectively, might be confusing because in fact both techniques are relative. Nevertheless, if the PSI-WAP measurements are relative to a well-defined terrestrial reference frame (e.g. European Terrestrial Reference System, ETRS89) the PSI-WAP measurements become comparable with other datasets and the term absolute measurement can be used for a GNSS calibrated PSI-WAP dataset (Mahapatra et al., 2015).

The GNSS calibration procedure consists of (Goel and Adam, 2015a):

1. GNSS data analysis in order to identify jumps in the GNSS time series and a usability assessment of each cGNSS station.
2. Clustering of cGNSS stations according to coherent tectonic provinces.

3. Transformation of the GNSS coordinate (X, Y, Z) time series into mean velocities (v_X , v_Y , v_Z) and subsequently projection into the mean velocity in Line-of-Sight direction.
4. Calculation of the PS mean velocity in the neighborhood (e.g. 500 m) of the cGNSS stations and calculating the difference between the GNSS and PSI-WAP mean velocities.
5. Deformation plane fitting through the differences between the GNSS and PSI-WAP mean velocities using a least-squares approach with first grade polynomials. If higher order polynomials are used the result might be affected by overfitting.
6. Subtraction of the interpolated deformation plane from the PSI-WAP mean velocities.

Note that the calibration is performed for each tectonic province separately in order to preserve a discontinuous deformation field at fault zones.

>200 cGNSS stations of the German SAPOS® reference network exist in Germany (Jahn, 2015, Jahn et al., 2011). It is projected to use approximately 100 for the calibration and the rest for the accuracy assessment of the PSI-WAP mean velocity. For the PSI-WAP validation only GNSS stations showing relatively fast deformation (e.g. $\geq 2 \text{ mm a}^{-1}$) are planned to be used, while for the calibration only GNSS stations showing little or no deformation are planned to be used (e.g. $< 2 \text{ mm a}^{-1}$). The reason for this strategy is that only large-scale deformation, caused by tectonic processes, should be present in the GNSS calibration dataset. The definition of the tectonic provinces used for clustering the cGNSS stations is an ongoing research topic (Lege et al., 2016, Spies et al., 2016). Fig. 4.7 shows the distribution of cGNSS stations in relation to Sentinel-1 tracks. Due to the spatially dense distribution the proposed GNSS calibration workflow seems to be suitable.

Validation

The aim of the PSI-WAP validation is to assess the precision and accuracy of the L2A dataset with respect to the mean velocity, the displacement time series and the PS location.

The precision of the mean velocity is provided for every PS in the attribute table. The accuracies of the geocoding and the mean velocity is assessed for selected PS and are validated against cGNSS stations.

Precision of the mean velocity

In practice, various parameters influence the precision of the mean velocity, e.g.: observation time span (Emardson et al., 2003), number of acquisitions (Adam et al., 2009), tropospheric delay (Agram and Simons, 2015, Fattahi and Amelung, 2015), orbital errors (Fattahi and Amelung, 2014), spatial density and signal to clutter ratio (SCR) of the PSs, redundancy of the reference network, and the distance in relation to the reference point (Ferretti, 2014).

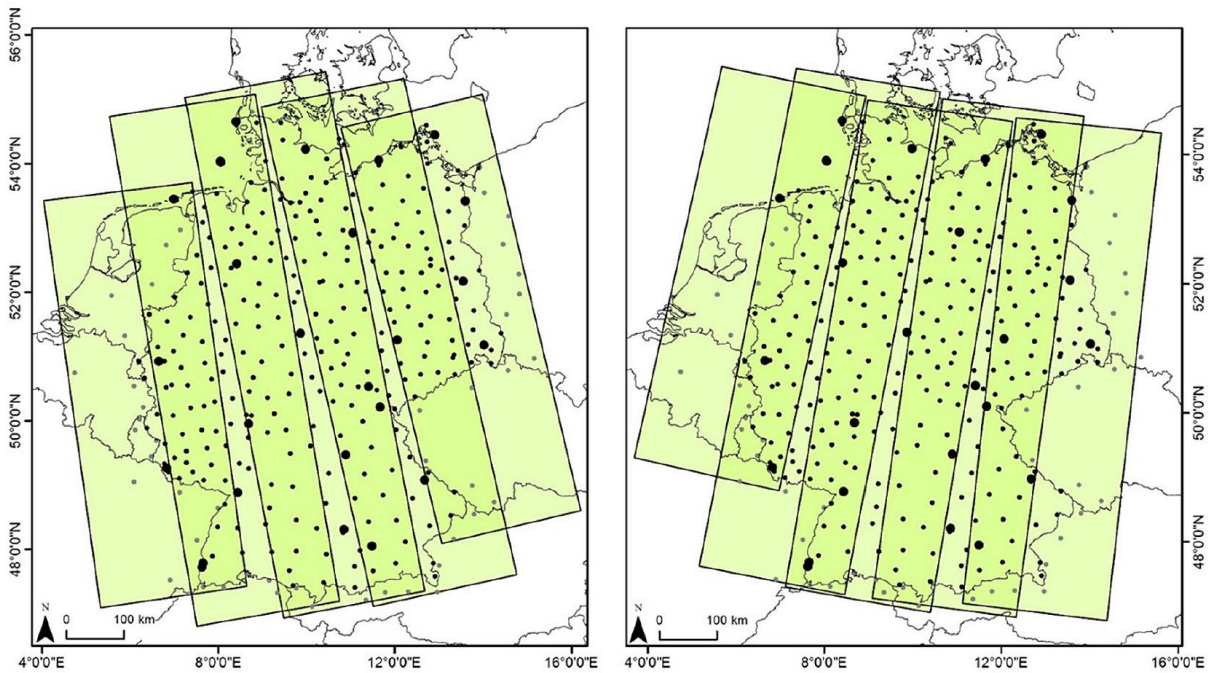


Figure 4.7: Distribution of continuous GNSS stations (GREF network: big black points, SAPOS network: small black points, stations outside of Germany: grey points) in relation to Sentinel-1 tracks (ascending orbit: left, descending orbit: right).

In order to report on the quality of the PSI dataset of the pilot study, the precision of the estimated mean velocity parameter is characterized by two quality measures. Both support an interpretation of the PSI velocity field.

First, the temporal coherence per PS is a normalized (value from 0 to 1) signal to noise ratio. It is characterizing the SCR of the PS, uncompensated atmosphere effects and unmodelled deformation. Second, the Gaussian error propagation provides the standard deviation of the deformation (in units of mm per year). It considers the structure and redundancy of the reference network and provides the spatial error propagation in contrast to the coherence. Finally, it characterizes the non-systematic errors, e.g. scattering noise and uncompensated tropospheric and deformation effects, with respect to the mean velocity but not residual spatial trends/ramps (Shau et al., 2016). Van Leijen (2014) provides a comparison and description of several quality measures.

In PSI, only a single observation is present per location per epoch (Van Leijen, 2014). However, three parameters need to be estimated (LOS velocity, topography update and atmosphere effect). As a consequence, the estimation is under-determined and a complete quality assessment based on geodetic quality control methods cannot be achieved. In the pilot study the velocity standard deviation and the temporal coherence are computed. The Gaussian error propagation analysis is part of the weighted integer least square estimator (Kampes, 2006) which is used for the estimation of the mean velocity and the residual height. It is based on a stochastic model (Kampes, 2006).

Accuracy of the geocoding

The assessment of the geocoding accuracy gives information regarding the accuracy of the PS location. Non-systematic shifts, due to an incorrect residual height estimation of the PS (not systematic because the residual height is estimated for each PS) as well as systematic shifts, due to timing inaccuracies of the master scene, affecting the complete PSI dataset can be present. In order to automatically assess the geocoding accuracy of a PSI dataset the PS location is related to the real location of a backscattering object on the Earth's surface. For this reason more than ten Corner Reflectors (in combination with cGNSS stations), spread over Germany, are used up to now (several more are planned) to automatically quantify the geolocation accuracy of the corresponding PSs. The connection between the phase center of the SAR- and the GNSS- data will be established by periodic tachymetric measurements.

Accuracy of the mean velocity

The assessment of the mean velocity accuracy uses a correlation analysis between the PSI-WAP mean velocity and the mean velocity based on GNSS time series data. The measurement of the PSI-WAP analysis can be biased due to e.g. few acquisitions (i.e. <20), incorrect estimation of the topographic/atmospheric phase contribution (mountainous terrain, strong atmospheric variability) and error propagation (separated clusters within the reference network). It can reach several mm per year. However, the differential motion of two PSs over short distances characterized by a high Signal-to-Noise ratio can be estimated with sub-millimeter accuracy (Ferretti, 2014). Although the point position accuracy of cGNSS stations in Z direction is in the order of centimeters the mean velocity can have accuracies in the order of mm per year because of the high temporal sampling rate of a cGNSS station. Within the Ground Motion Service Germany the accuracy is routinely assessed by using a set of continuous GNSS stations. GNSS coordinate time series (X, Y, Z) are transformed into mean velocities (v_X , v_Y , v_Z) and projected into the mean velocity in Line-of-Sight direction. Then the PSI-WAP based mean velocities are interpolated to obtain the velocity at the exact location of the cGNSS station. For this purpose, the standard deviation of the mean velocity of each PS is used to weight the interpolation. Subsequently the difference between the mean velocity of the cGNSS station and the interpolated PS mean velocity is calculated and provided in the validation report.

4.6 Case-study PSI-WAP Lower Saxony

The motivation of the pilot study Lower-Saxony is to show that the L2A dataset is able to monitor various surface displacement phenomena. The study area is located in Northwest Germany and has an extension of $>30,000 \text{ km}^2$. Several processes, e.g. soil compaction due to drainage (Behre, 2004), peat shrinkage due to drainage, evaporation and oxidation (Eggesmann, 1984), natural gas extraction (Wolf, 2012) and salt mining are causing subsidence in the study area. Germany's major natural gas fields are located in the study area at a mean depth of 3.5 km below the surface. A small-scale uplift is expected due to high-pressure fluid injection for petroleum production in the South-Western part of the investigated area. A large-scale surface motion might be present due to glacial isostatic adjustment (GIA) in the forebulge of the Fennoscandian uplift (Brandes et al., 2015). Areas potentially affected by local and regional displacement processes are indicated in Fig. 8 (e.g. potential sinkhole hazard from LBEG, 2016).

PSI-WAP processing

The Pilot study uses ERS-1/2 data because no Sentinel-1 data were available at the time when the pilot study started (early 2014). The PSI-WAP processing is based on six partly overlapping ERS-1/2 frames (Fig. 8). Two frames shifted in azimuth direction were used in track 294 in order to cover the whole area of interest. Each SAR data stack consists of 49–73 ERS-1/2 acquisitions, covering the timespan from 1992 to 2001 (Table 4.3). DLR's PSI Genesis processor (Adam et al., 2013) is used for the PSI-WAP processing. After processing each stack separately, the PSI results are detrended and mosaicked in order to obtain a consistent large-area PSI-WAP dataset covering the whole area of interest.

Mosaicking

The result of the detrending and mosaicking step is shown in Fig. 4.9. Before mosaicking each PSI dataset (Fig. 4.9 A–F) is referring to an individual PS reference point, after mosaicking all PSI datasets are referring to a single PS reference point (Fig. 4.9 G). A large-scale trend of the mean velocity (Fig. 4.9 A, B, F) is visible before the PSI results were detrended and mosaicked (Fig. 4.9 G). Within the overlap areas of the tracks, the offset of the mean velocity of nearby PSs from different tracks are computed. The maximum offset after the mosaicking is below 0.1 mm a^{-1} , thus a consistent PSI-WAP dataset covering the whole area of interest ($>30,000 \text{ km}^2$) is created.

In the overlap areas the spatial (and temporal) sampling frequency is increased due to different acquisition geometries and acquisition dates of the SAR data stacks (Fig. 4.10). By analyzing several independent data stacks covering the same object of interest the interpretation of the observed displacement can be enhanced. In order to demonstrate this effect, four neighboring PSs (distance $<34 \text{ m}$), based on four independent SAR data stacks, are picked in Fig. 4.10. All four PSs show a subsidence (mean velocity of all four PSs: -6.7 mm a^{-1}) in the timespan from 1992 until mid-1999. Between end-1999 and 2001 the displacement time series of three PSs (track: 294S, 294 N and 337) show an aliasing of the phase unwrapping procedure most probably due to a fast uplift. One PS (track 65) shows a stable behavior between end- 1999 and 2001, but it has only five acquisitions in the year 2000. Because three out of four independent PSs (track: 294S, 294 N and 337) show an aliased phase unwrapping pattern in the displacement time series, the most probable interpretation is a fast uplift (dashed black line in Fig. 4.10). This interpretation is not possible when only the displacement time series of the PS from Track 337 is used. Thus it is planned to include all independently processed PSs in the final PSI-WAP (the L1A dataset).

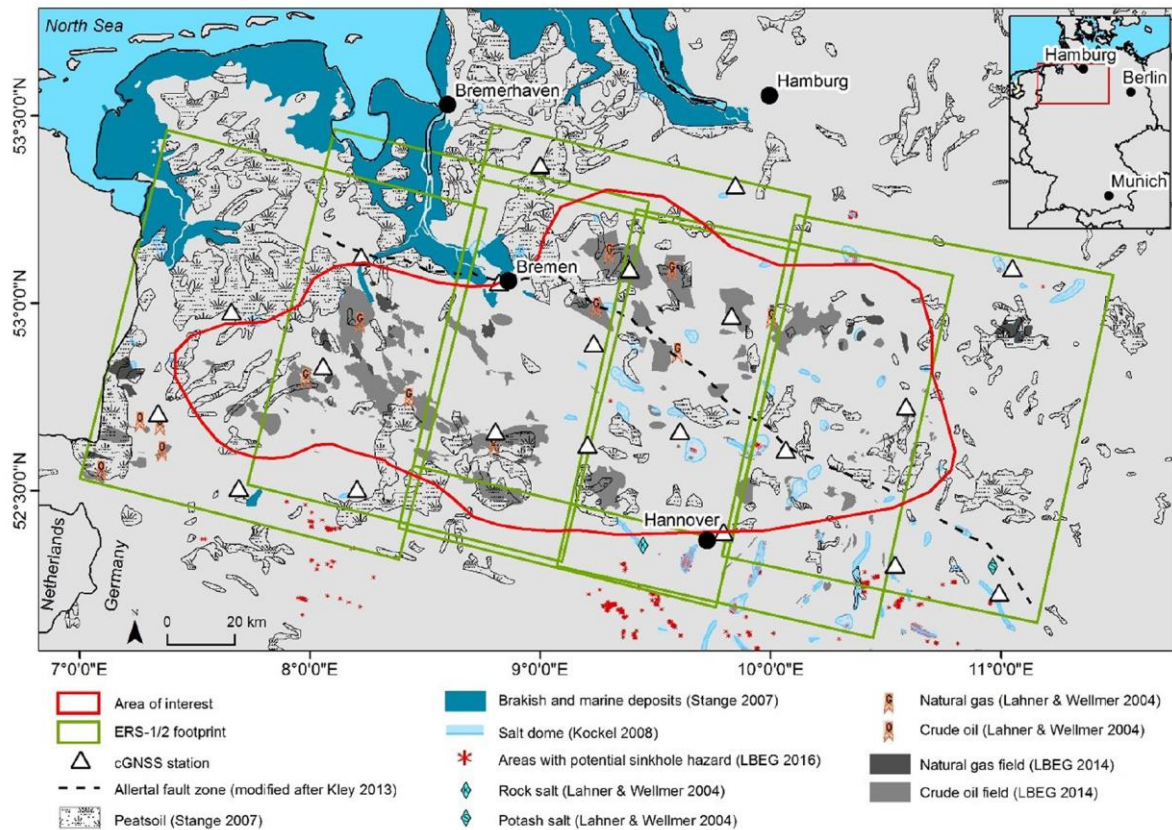


Figure 4.8: The Figure shows the location of the input dataset (SAR data, cGNSS stations) and areas potentially affected by displacement process (mining, peat loss, soil compaction, sinkholes, tectonics). The annotation shows the track number of the ERS-1/2 SAR data. Two SAR data stacks are used from track 294 to completely cover the area of interest.

In order to enable a proper identification of the PS and its corresponding data stack, a data stack identification number will be included in the attribute table of the L1A dataset.

After mosaicking, a GNSS calibration is required to introduce large-scale deformations (e.g. from glacial isostatic adjustment, GIA), to support a combined use with independent datasets (e.g. terrestrial measurements) (Fuhrmann et al., 2015) and for mutual analysis of PSI-WAP datasets based on ascending and descending orbits.

GNSS calibration of the ERS-1/2 based PSI-WAP dataset

Fig. 4.9 visualizes the effect of the transformation of the PSI-WAP dataset into absolute measurements by using GNSS time series (Brockmeyer, 2015). Before calibration, the PSs are relative to one reference point, after the calibration the PSs are relative to a GNSS based velocity field based on time series of cGNSS stations (Fig. 4.9).

Table 4.6.1: Characteristics of the ERS-1/2 data used in the PSI-WAP processing.

Track	Time period [dd.mm.yy]	N° of acquisitions	PS density [PS per km ²]	N° of PS
22	20.09.1992–01.11.200	49	23.14	237,512
65	06.05.1992–13.01.2001	53	22.53	231,455
251	28.07.1992–22.12.2000	69	16.19	158,348
294	17.04.1992–20.11.2000	69	17.38	172,138
294 S ^a	17.04.1992–20.11.2000	73	19.87	201,505
337	25.05.1992–19.10.2000	52	17.92	181,395

^a Two frames are used from track 294 to cover the entire area of interest.

Being relative to a well-defined terrestrial reference system (e.g. European Terrestrial Reference System 1989, ETRS89) the PSI-WAP data are transformed into absolute measurements. In the case study area, two deformation planes were estimated separately to avoid an interpolation across a fault. The location of the fault was extracted from (Kley, 2013). Attention regarding the processing of GNSS time series has to be paid.

E.g. a change of GNSS receiver hardware can cause an offset in the GNSS time series and thus might lead to an incorrect mean velocity of the cGNSS station. Another potential error source is caused by the location of most GNSS receivers on top of (large) buildings, prone to internal deformation patterns (e.g. caused by thermal expansion/contraction) which might cause a bias in the GNSS velocity field. This effect is mitigated by using GNSS time series from several years. Due to the lack of GNSS data from 1992 to 2001 GNSS data from 2008 to 2011 are used to test this method. Keeping in mind that in this approach only linear velocities are assumed, this approach is suitable for the purpose of the pilot study. For the L2A dataset GNSS and SAR data will cover the same timespans. It has to be mentioned, that multiple solutions for the large area GNSS velocity field can be present, depending on the geologic, tectonic and/or geophysical assumptions (compare the approach of the IKÜS project results, IKÜS, 2008).

Validation

The validation procedure used in the frame of the national Copernicus service is demonstrated based on the pilot study.

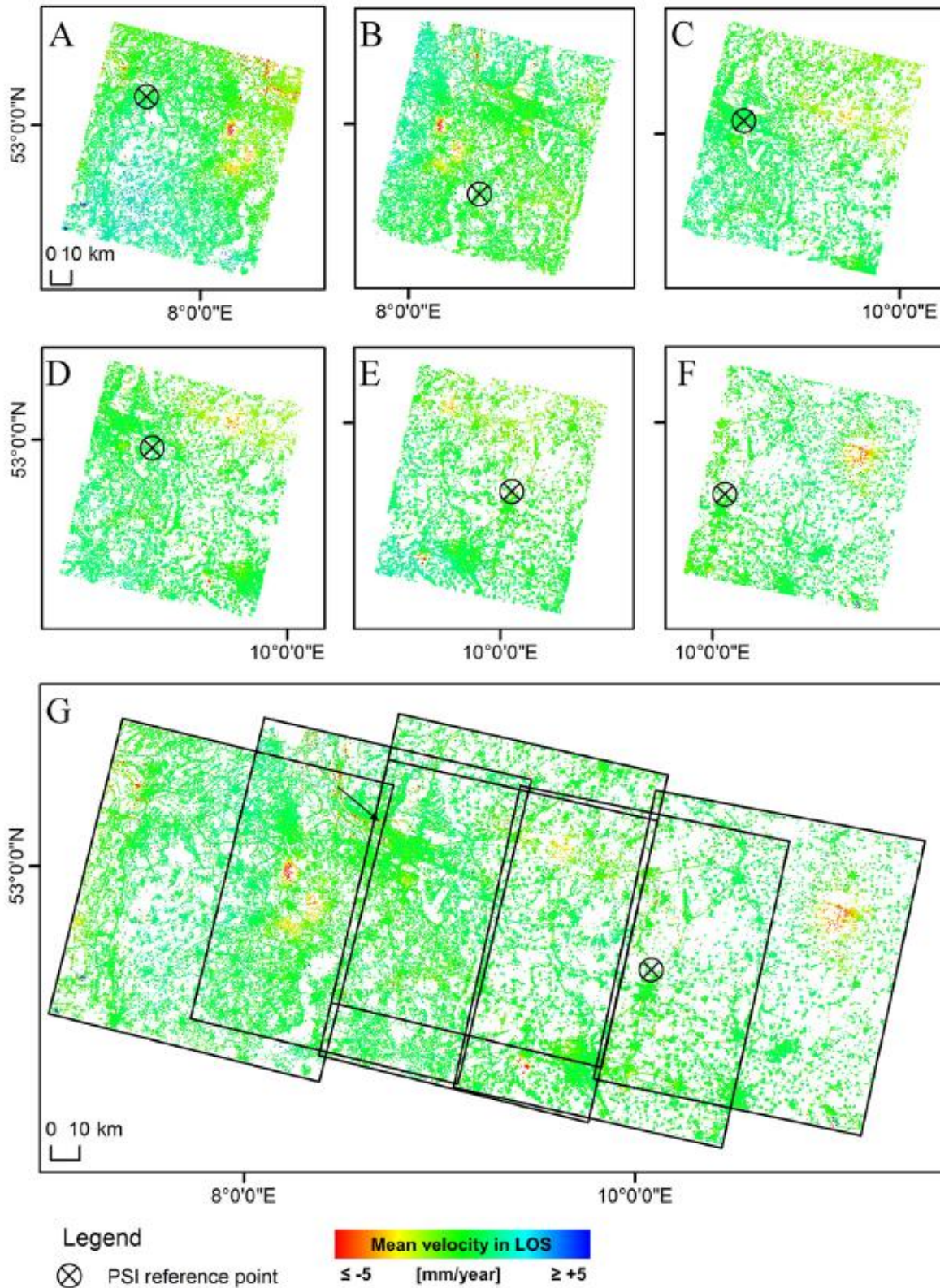


Figure 4.9: Original PSI result per SAR data stack (A–F) and after the detrending and mosaicking step (G). The location of the six SAR data stacks are indicated as black outlines (G). The black arrow indicates the location of the PSs shown in Fig. 4.10.

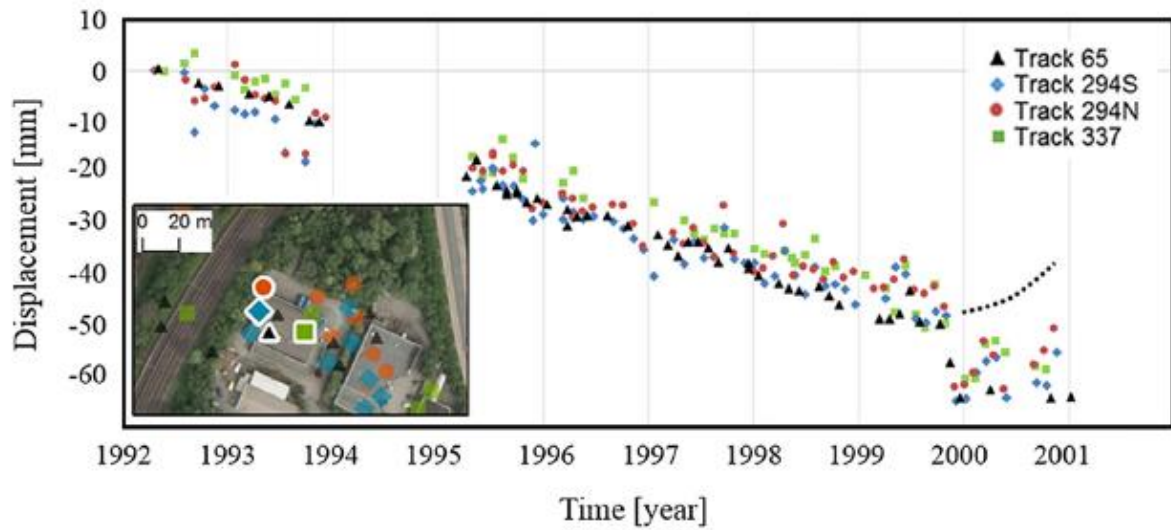


Figure 4.10: Displacement time series of four PSs (location is indicated by the white circle in the inset) in the overlapping area of four SAR data stacks. The temporal and spatial sampling density is increased in the overlap areas of the SAR frames. The interpreted displacement after end-1999 until 2001 is indicated by the dashed black line.

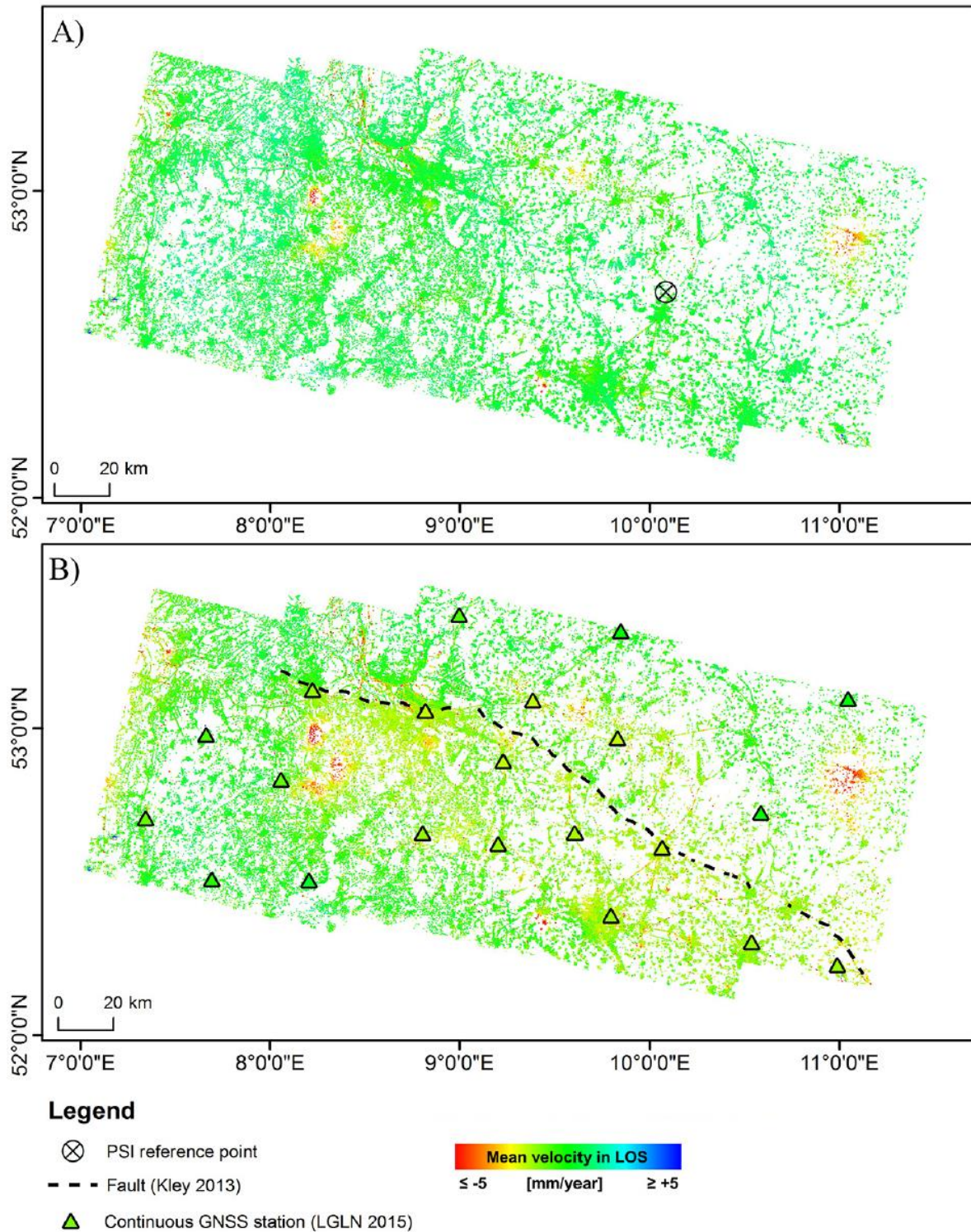


Figure 4.11: The Figure shows the PSI-WAP dataset before (A) and after the GNSS calibration (B). Before calibration the PSs are relative to one reference point, after the calibration the PSs are relative to a GNSS based velocity field based on time series of continuous GNSS stations. Being relative to a well-defined terrestrial reference frame based on GNSS time series the PSI-WAP data is transformed into an absolute measurement.

5.4.1. Precision of the mean velocity

The precision of the mean velocity is shown exemplarily for track 337 (Fig. 4.12), based on the Gaussian error propagation (Shau et al., 2016). The standard deviation (2σ) of the mean velocity for track 337 ranges from 0.27 up to 0.5 mm a⁻¹. The high precision of these PSs is achieved by using a large data stack (49 SAR images) and a highly redundant reference network.

5.4.2. Accuracy of the geocoding

In order to interpret the observed displacement correctly or combine the PSI data with independent datasets (e.g. geological maps, other PSI or GNSS data) an accurate geocoding is mandatory. The geocoding accuracy of a PSI dataset, based on ERS-1/2 SAR data can be in the order of couple of tens of meters (Agudo et al., 2006). The bias in the geolocation in range direction can be due to incorrect PS height estimation (which is related e.g. to the perpendicular baseline), the error in azimuth direction can be due to timing inaccuracies of the master scene (Adam and Kampes, 2008). The PS geocoding accuracy in range direction is variable for each PS (because the PS height is estimated for each PS), while the geocoding accuracy in azimuth is constant within one PSI dataset. The accuracy of the PS height estimation based on Sentinel-1 data is expected to be lower in comparison to ERS-1/2 data because the perpendicular baseline is kept within a small orbital tube with a diameter of 100 m (rms) (Torres et al., 2012), thus a large number of acquisitions is needed to reach a high accuracy in range direction.

5.4.3. Accuracy of the mean velocity

The accuracy assessment of the PSI-WAP mean velocity is based on cGNSS station data. Unfortunately the PSI-WAP and GNSS datasets used in the case study cover different time spans (PSI-WAP: 1992–2000 versus GNSS: 2008–2011), so the intention of this validation is to show the validation concept for the L2A dataset.

PSs in the neighborhood (100 m) of the cGNSS station are used for the validation. Because the effective scattering center of the GNSS antenna and the effective scattering center of the PSs are not identical, a spatial interpolation is required (Raucoules et al., 2009). The precision of the mean velocity of each PS is used to weight the interpolation of the PSI-WAP mean velocities. In Fig. 4.13, the interpolated PS velocities in the neighborhood of a cGNSS station are shown. The interpolated velocity at the location of the cGNSS station will be used for the validation.

5.5. L3 product example based on a L2A dataset

Based on the L2A PSI-WAP dataset exemplarily a L3 product is developed to introduce the potential of the PSI-WAP dataset for further exploitation. As example the area of influence caused by natural gas extraction and the shape of the corresponding subsidence bowl are presented.

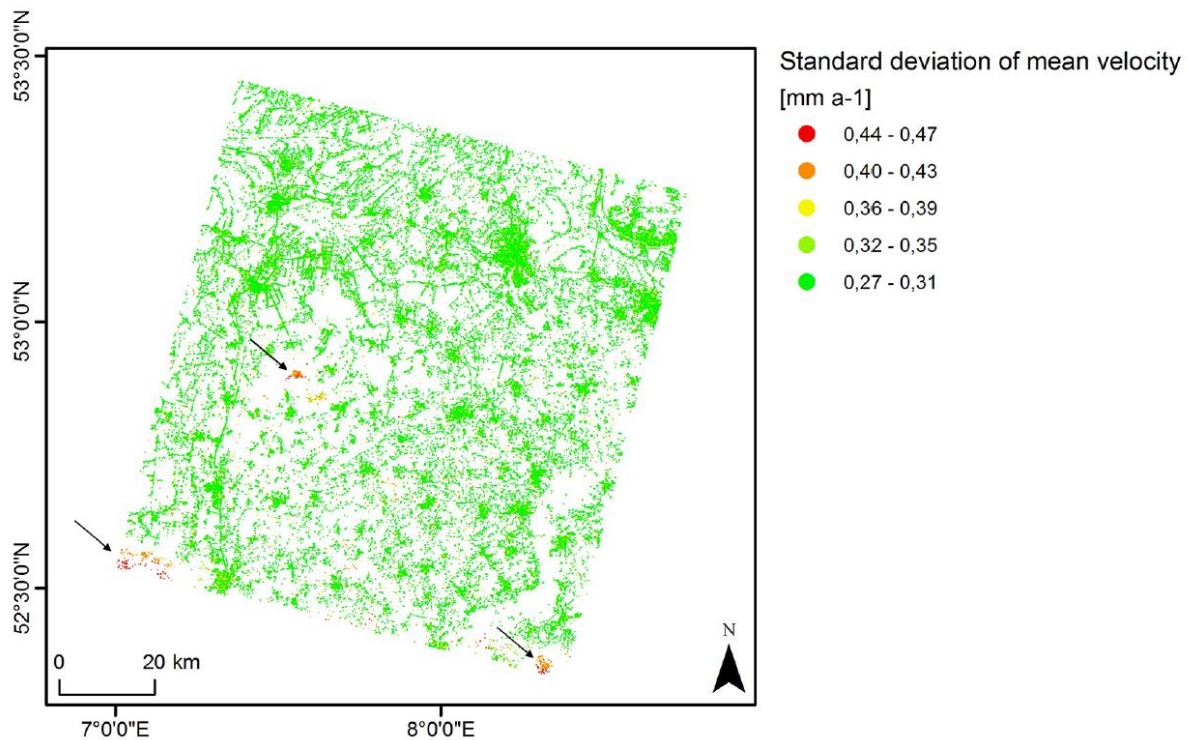


Figure 4.12: The precision distribution of the mean velocity of track 337 is shown in this Figure. Although the maximum value of the standard deviation is very small $<0.5 \text{ mm a}^{-1}$ at least three PS clusters with relative high standard deviations can be seen (indicated with black arrows).

In order to define a L3 product the process(es) which causes the observed displacement have to be identified. This can be realized by several approaches: e.g. superposition with thematic maps, explanatory regression with independent datasets etc.

For the L3 example the observed displacement is related to natural gas extraction, assessed by comparison with the location of the natural gas field (LBEG, 2014) and the amount of extracted natural gas over time (LBEG 1992–2000). The result shows a strong spatial and temporal agreement (Fig. 4.14). Furthermore, a comparison with other potential displacement processes (peat shrinkage, groundwater extraction) shows no agreement. In order to visualize the shape of the subsidence bowl and delineate the area of influence, lines of equal subsidence rates are calculated. A kriging interpolation based on the PSI-WAP mean velocity data and subsequent processing of lines of equal subsidence rate is performed. In order to interpret the PSI-WAP data in more detail a close up view showing the PS mean velocity and the associated standard deviation is provided to the end user (Fig. 4.15).

4.7 Data-/product provision

The official provision of L2A datasets and upcoming L3 products is projected via an online platform at BGR. It is conceptualized, that the L2A dataset will be provided as a download as well as a web feature service (WFS) for online integration into local GIS. Besides that, a service

platform is planned to provide a Web-GIS application for online visualization of the L2A dataset.

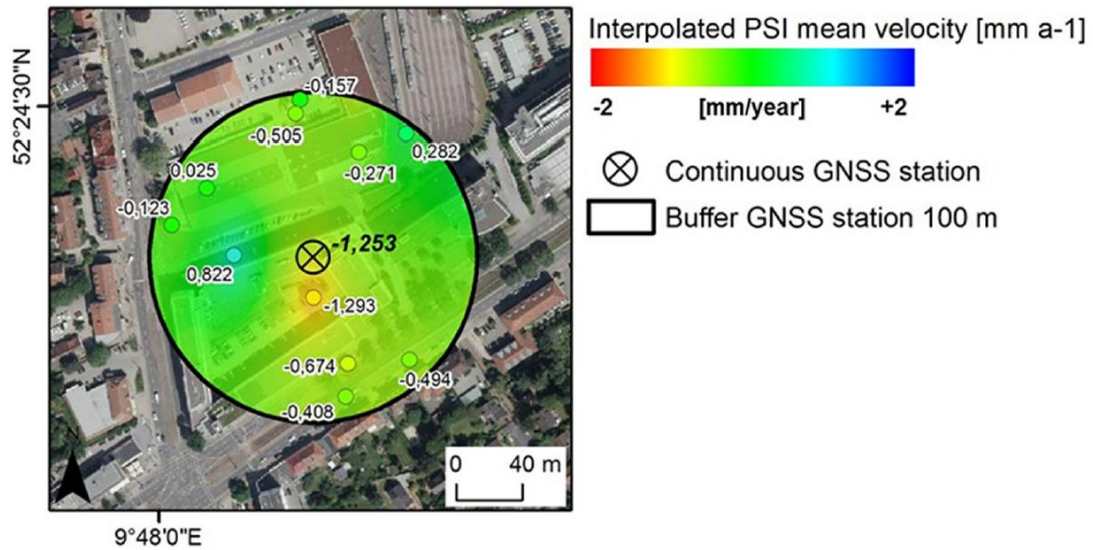


Figure 4.13: Location of a continuous GNSS station on top of a building and PSs with a maximum distance of 100 m. The interpolated PSI-WAP mean velocity at the location of the GNSS station is -0.832 mm a^{-1} . The numbers with a white outline are showing the PSs mean velocity in Line-of-Sight in mm a^{-1} . The bold number shows the cGNSS mean velocity projected in Line-of-Sight. Note that the GPS time series covers a different timespan than the PSI-WAP time series (2008–2010 respective 1992–2001). The purpose of this Figure is to visualize the foreseen validation workflow for the Ground Motion Service Germany. A true-color digital orthophoto serves as background (DOP40cm, ©BKG 2015).

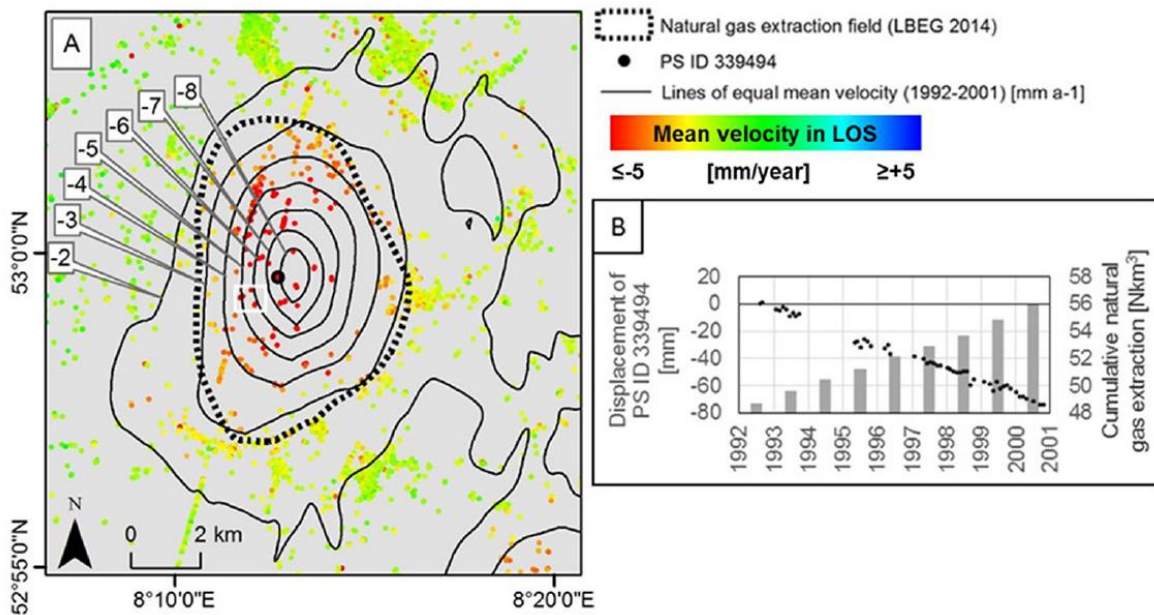


Figure 4.14: PSI-WAP mean velocity (mm a^{-1}) superimposed with the outline of a natural gas extraction field shows high spatial correlation (A). The shape of the subsidence bowl is

clearly visible through the lines of equal mean velocity (A). A comparison of the displacement time series versus the cumulative natural gas extraction (LBEG, 2015) shows a strong temporal correlation (B). The white rectangle shows the location of Fig. 4.15.

This application is envisioned to be extended with nationwide available geoscientific data (geological, pedological, hydrological maps) in order to provide the user with a comprehensive dataset to investigate the observed displacements with e.g. geologic strata. Ongoing work is focusing on e.g. analysis tools for interactive time series visualization of several selected PSs and displacement statistics for user-defined areas of interest to provide not only the velocity field and the time series but also user driven statistical information which is enhanced by geoscientific information.

4.8 Conclusion

Several European research projects e.g. ESA-TerraFirma (2003–2012) (Adam et al., 2009), EU-FP7-PanGeo (2011–2014) (Capes, 2012) and EU-FP7-SubCoast (2010–2013) (Gruijters and van der Krogt, 2013) demonstrated the operational readiness of the PSI technique. In order to foster the operational use of Copernicus Sentinel data and derivative products the Ground Motion Service Germany is established. This manuscript gives an overview of the national user requirements, the concept of the service, the nationwide PSI-WAP dataset (L2A) characteristics and its validation scheme as well as a L3 product example.

The data- and processing workflows used in the ERS-1/2 based pilot study are not comparable to the envisaged Sentinel-1 based PSI-WAP. This is due to the different acquisition mode (TOPS vs. Stripmap), the smaller perpendicular baseline (orbital tube with a diameter of 100 m vs. several hundred meters) the larger swath width (250 km vs. 100 km), the larger area of interest (357,375 km² vs. 30,000 km²), the different temporal resolution (6 days repeat cycle vs. 35 days) and observation time span (the first S-1 PSI-WAP will cover two years vs. nine years in the pilot study). E.g. the small perpendicular baseline is causing better coherence properties for distributed targets and thus a higher spatial sampling for SBAS-like algorithms. At the same time it causes a lower sensitivity regarding the topographic phase contribution (for PS's and DS's). Thus, the PS height estimation and in turn the geocoding accuracy in range direction will be less accurate compared to orbit configurations characterized by a larger perpendicular baseline.

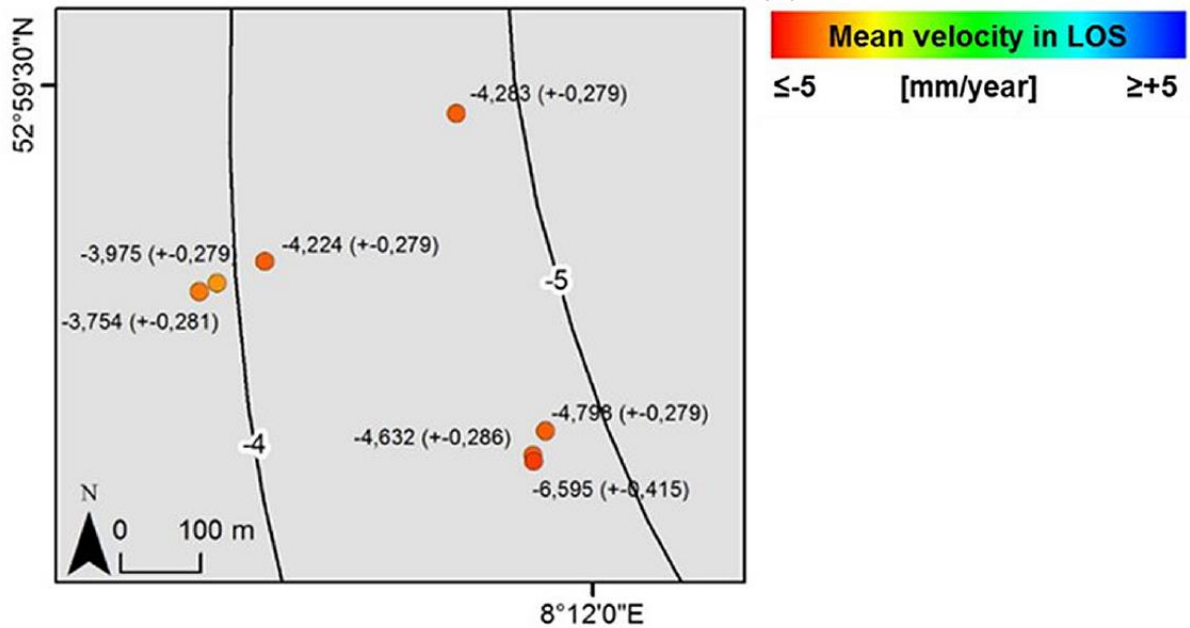


Figure 4.15: A close up showing the mean velocities (mm a^{-1}) of selected PS, the corresponding standard deviation and the interpolated lines of equal mean velocity. It gives the user the possibility to investigate the measured displacement in more detail.

However, a high geocoding accuracy in range direction using Sentinel-1 data is expected, but it needs more acquisitions and longer observation time spans compared to e.g. ERS like orbit configurations. Another difference between Sentinel-1 and ERS-1/2 is the production concept of the mission operator. The spatial extent of ERS-1/2 stripmap scenes is based on a fixed pre-defined framing concept, while the extent of Sentinel-1 TOPS scenes are based on slices with a maximum data-volume of 2 GB per GeoTIFF band (ESA, 2017). This causes a variation of the along track scene position, if the start of the data take is varying. In order to produce spatially consistent Sentinel-1 data stacks the SLC products are resliced before PSI processing. This is done by assembling pre-defined group of bursts, including their corresponding annotations. The group of bursts are chosen with respect to the land-surface characteristics of the imaged area (vegetated and mountainous areas should be within a resliced frame to minimize Gaussian error propagation by construction of an optimized PS reference network). An overlap of one burst per sub-swath in along-track direction is used for the mosaicking procedure.

To sum up, the SAR processing workflow of the ERS based pilot study are not directly transferable to the envisaged Sentinel-1 PSI-WAP, but the experiences with respect to a base product for the Ground Motion Service Germany are valid. E.g. the production of value added products for mining applications, the use of several quality indicators and the usefulness of a GNSS calibration.

The large area of interest in combination with the fast repeat cycle will produce significantly higher data volumes. This affects all steps of the data flow, e.g. raw data transmission, (pre-) processing, quality control, value-adding and product delivery to the end-users. Recent interferometric SAR processing approaches aiming at big SAR-data processing demonstrate the technological feasibility to process large data volumes within short time (Casu et al., 2014,

Zinno et al., 2016, Ansari et al., 2016). Regarding quality control an increased automatization is envisaged, e.g. the calculation and reporting of the assessed accuracies.

The installation of corner reflectors for the assessment of the geocoding- and mean velocity accuracy is ongoing.

It is expected that the L2A dataset will significantly contribute to the applications identified by the German national user community. However, the monitoring of small scale and/or very fast moving terrain may require higher spatial/temporal resolution SAR data. For this reason very high spatial resolution SAR data from Copernicus contributing missions e.g. TerraSAR-X/TanDEM-X or Cosmo-SkyMed are foreseen as SAR input data for the L2B dataset. The complementary character of the L2A and L2B datasets, in terms of coverage and resolution, is expected to cover a broad range of displacement monitoring applications. However, plausibility assessments are mandatory for any L3 product because the observed displacements of PSs are not obligatory related to a near or sub-surface process, but can also be caused by the characteristics of the backscattering objects e.g. by internal building deformation. The plausibility assessment can be based on a comparison with geoscientific information (e.g. geological map, pedological map, and hydrological map) and/or field surveys. The presented validation aspects (measurement precision, geocoding-/mean velocity accuracy) are aiming to support the subsequent plausibility assessment.

The identification, definition and testing of value-added products is ongoing. E.g. the area of influence of mining activities, quantification of reservoir compaction (Fokker et al., 2012), update of landslide inventory.

4.9 Acknowledgements

The authors thank the European Space Agency (ESA) for providing ERS-1/2 SAR data. Highly appreciated is the contractor German Aerospace Center (DLR) for processing the SAR data and fruitful discussions regarding the PSI-WAP dataset, the Department of Geoinformation and Land Development of Lower Saxony (LGLN) for processing the GNSS data and the State mining authority of Lower Saxony (LBEG) for productive discussions regarding the interpretation of the PSI-WAP results. All workshop attendees are acknowledged for their contributions to specify the user requirements. The authors thank the anonymous reviewers for their useful comments that improved the quality of this paper. This research is funded by the BGR/BMWi.

5 Classification of Landslide Activity on a Regional Scale Using Persistent Scatterer Interferometry at the Moselle Valley (Germany)

This chapter was published as:

Kalia, A. C. (2018): Classification of landslide activity on a regional scale using Persistent Scatterer Interferometry at the Moselle Valley (Germany), *Remote Sens.*, 10(12), 1880, <https://doi.org/10.3390/rs10121880>

5.1 Abstract

Landslides are a major natural hazard which can cause significant damage, economic loss, and loss of life. Between the years of 2004 and 2016, 55,997 fatalities caused by landslides were reported worldwide. Up-to-date, reliable, and comprehensive landslide inventories are mandatory for optimized disaster risk reduction (DRR). Various stakeholders recognize the potential of Earth observation techniques for an optimized DRR, and one example of this is the Sendai Framework for DRR, 2015–2030. Some of the major benefits of spaceborne interferometric Synthetic Aperture Radar (SAR) techniques, compared to terrestrial techniques, are the large spatial coverage, high temporal resolution, and cost effectiveness. Nevertheless, SAR data availability is a precondition for its operational use. From this perspective, Copernicus Sentinel-1 is a game changer, ensuring SAR data availability for almost the entire world, at least until 2030. This paper focuses on a Sentinel-1-based Persistent Scatterer Interferometry (PSI) post-processing workflow to classify landslide activity on a regional scale, to update existing landslide inventories a priori. Before classification, a Line-of-Sight (LOS) velocity conversion to slope velocity and a cluster analysis was performed. Afterwards, the classification was achieved by applying a fixed velocity threshold. The results are verified through the Global Positioning System (GPS) survey and a landslide hazard indication map.

5.2 Introduction

On all continents, landslides represent a major natural hazard which can cause significant damage, economic loss, and loss of life. Landslides can be defined as a downslope mass movement of rock, debris, or soil (Cruden, 1991), and can be categorized with respect to the type of material (bedrock, debris, soil), the type of movement (fall, topple, slide, flow, complex), and the velocity (Cruden and Varnes, 1996).

Compared to other natural hazards (e.g., earthquakes, storms, or flooding), the impact of landslides is often underestimated because the affected areas are mostly on a local scale. Between 2004 and 2016, 55,997 fatalities caused by landslides were reported worldwide (Froude and Petley, 2018). In Europe, it has been reported that landslides caused 312 fatalities and an economic loss of approximately 48 billion € in the timespan of 1998–2009 (Herrera et al., 2018). Landslide hazards are expected to increase in the future through population growth, new settlements in landslide-prone areas, and climate change (Gariano and Guzzetti, 2016).

Up-to-date, reliable, and comprehensive landslide inventories are mandatory for optimized disaster risk reduction (DRR) regarding landslides. Landslide risk can be defined as a measure of the expected probability of a damaging event for a specific area. It is based on the product of three factors: hazard, vulnerability, and exposure of elements at risk (Sassa et al., 2005). Landslide hazards can be defined as specific areas' susceptibility to a potentially damaging landslide. For hazard assessments, landslide inventories are an important source of data. Conventional methods for the production of landslide inventories include things like the visual interpretation of stereoscopic aerial imagery, Light Detection and Ranging (LiDAR)-based digital surface models, and field surveys. A review of methods used for the production of landslide inventories is given by (Guzzetti et al., 2012). In general, landslide inventories lack information regarding the landslides' state of activity, and are thus not up-to-date.

A new methodology for the updating of landslide inventories was recently proposed by the scientific community (e.g., Righini et al., 2012, Casagli et al., 2016, Rosi et al., 2017). These studies showed the potential of advanced Differential Interferometric SAR (DInSAR) methods (e.g., Persistent Scatterer Interferometry, Ferretti et al., 2001, Small Baseline Subset, (Berardino et al., 2002, SqueeSAR, Ferretti et al., 2011) for updating landslide inventory maps for large areas (up to 2100 km²). The major benefit of these methods is the provision of landslide movement information for large areas, with high precision and high temporal resolution. A standardization of procedures to classify the landslide state of activity, named the “PSI-based matrix approach”, was proposed by Cigna et al. (2013). It focuses on the post-processing and comparison of PSI datasets covering successive time spans. The post-processing includes a conversion of the PSI LOS vector into the slope direction and the application of thresholds regarding the PSI-derived mean velocity and the minimum number of measurement points (persistent scatterer, PS) per landslide.

In this study, the “PSI-based matrix approach” is modified using a cluster analysis, instead of having a minimum number of PS per landslide as a precondition for the classification of the landslide’s state of activity. Our hypothesis was that the classification of the landslide’s state of activity would be more robust if a cluster of PSs with similar velocities is used, because the criterion for assigning a “representative velocity” to a landslide is not based on the number of PSs alone, but on a group of PSs with similar velocities. The clustering of PSs with similar velocities has been proposed by (Lu et al., 2012, Xi, 2017). However, the clustering algorithm used in this work (local Moran’s Index) has not been proposed for landslide applications.

The second aim of this study was to demonstrate the capability of the German Ground Motion Service (BBD) for expanding landslide inventories with a classification of the landslide’s state of activity. The BBD PSI dataset was based on the recently started Copernicus Sentinel-1 SAR mission. The Sentinel-1 mission is of particular interest because it ensures SAR data availability for almost the entire world, until at least 2030 (follow-on missions are in preparation). Long-term SAR data availability, and operationally available, advanced DInSAR products is a key precondition for the update of landslide inventories. The EC-FP7 project SAFER has proposed three services regarding landslide mapping and monitoring (Casagli et al., 2016):

- Landslide Inventory Mapping (LIM) for large areas covering a few thousand square kilometers,
- Landslide Monitoring (LM) for single large landslides affecting built-up areas with a high risk level,
- Rapid Landslide Mapping (RLM) carried out after an emergency for rapid mapping of pre-existing landslides with potential reactivations and new landslides.

Using this service definition, this study focuses on the procedure of performing a LIM.

5.3 Study Area

The study area had a size of approximately 1500 km² and is located at the Moselle Valley, Germany. The Moselle Valley has different elements at risk, such as settlements, tourist attractions, federal roads, and a highway under construction. The river Moselle flows from the

southwest to the northeast, and divides the low mountain ranges of the Hunsrück in the south from the Eifel in the north. The river enters the study area at a height of 123 m. a. s. l. and leaves it at a height of 78 m. a. s. l., with a height difference of 45 m along with a distance of 145 km. The adjacent plateau and mountain ridges reach heights of more than 400 m. a. s. l. (Figure 5.1B). The geomorphology is characterized by narrow, V-shaped valleys with a pronounced meandering of the river, causing distinct slip-off banks and undercut slopes. While the slip-off banks are relatively flat, some of the undercut slopes are very steep (transect in Figure 5.1B) and reach inclinations of more than 40°. The majority of the slopes have inclinations below 30°. The slopes with a southwest-, southeast- and south exposition are often used for winegrowing. Most of the north-facing slopes and the upper slope areas are covered with forests. On steep undercut slopes, bare rocks emerge, and settlements are often at the foot of the slopes.

The geology of the study area is almost completely composed of Lower-Devonian Hunsrückslate (Unterems). The Hunsrückslate is a monotone, anchimethamorph sequence of approximately 3000 m-thick clay and siltstones, with sporadic occurrence of thin quartzitic sandstones and slates (LGB, 2003). At the southwestern border of the study area, near the village Schweich, a sequence of grayblue argillaceous schists with gravelsized concretions is present. Near the village Ürzig, light-red siliciclastics and tuffs are present. Near the village Alf, the Mosel Valley leaves the Hunsrückslate and enters an area composed of clay and sandstones, belonging to the Oberems/Devonian Laubach- and Hohenrhein sequence (Figure 5.1). All rock units were folded and foliated during the Variscian orogeny. Tectonically, the area belongs to the southeast-vergent Moselle depression. Since the Tertiary, the Rhenish Shield has been affected by largescale uplift, which is still ongoing. Multiple changes in the tectonic stress caused deep fragmentation of the rocks.

The fast incise of the Moselle Valley induced steep slopes with high relief energy. These young slopes are morphologically immature, and not yet in equilibrium. Evidence of the low slope stability is given by things such as landslides, rockfalls, tilting of houses, and cracks in roads.

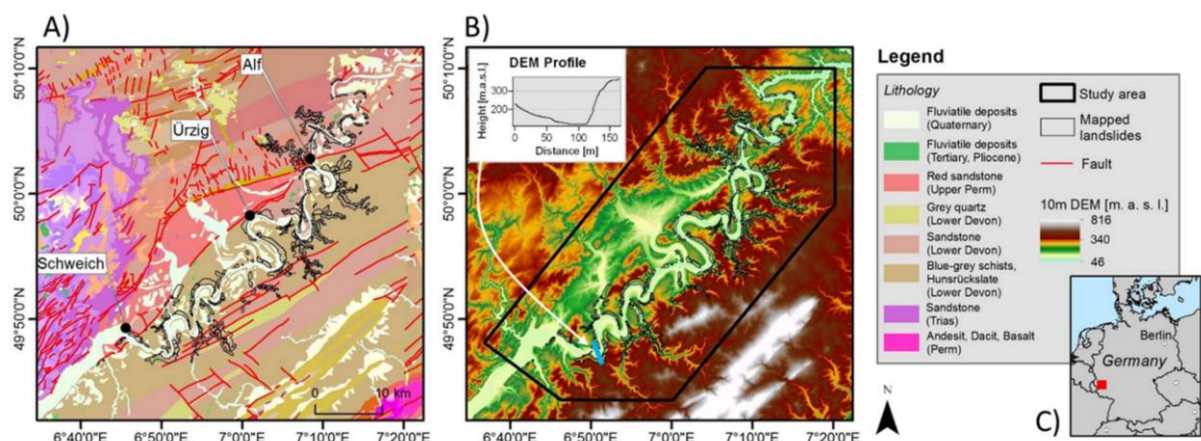


Figure 5.1: A) Geological setting (modified from geological map 1:200,000, GK1000, © BGR, Hannover, 2018, Zitzmann, 2003). B) Elevation map of the study area, based on a Digital Elevation Model (DEM) © GeoBasis-DE / BKG 2018 and characteristic elevation transect across the river Moselle. The location of the transect is indicated by the blue line. C) Location of the study area (red polygon) in Germany.

Landslides are defined as a downslope mass movement of rock, debris, or soil (Cruden, 1991). They can be categorized with respect to the type of material (bedrock, debris, soil), the type of movement (fall, topple, slide, flow, complex), and the velocity (Cruden and Varnes, 1996).

The majority of landslides in the study area are large, deep-seated slides, which are often located at the undercut slopes. The landslides are located between 80 and 427 m. a. s. l. Some of the landslides are in built-up areas and crossed by roads. The geomorphology often consists of convex, upper slope areas, and concave, lower slope areas. The DEM profile in Figure 5.1B represents the characteristic geomorphology of slopes at the river Moselle. In general, the landslides in the study area are related to the occurrence of the Hunsrückslate. Most of the displacements in the upper areas are in vertical direction, while in the convex lower parts of the landslides, horizontal displacements dominate. Besides the deep-seated slides, creeping soils/debris are present on relatively steep slopes where the soils/debris are characterized by low permeability. The highest measured debris slide velocity in the study area reaches up to 16 cm per year (Krauter, 2001).

5.4 Methodology and Data

The methodology consists of four steps: i) PSI-processing, ii) transformation from vLOS into vSLOPE, iii) cluster analysis, and iv) classification of the landslide's state of activity. The classification results are verified with a landslide hazard indication map.

5.4.1 PSI-Processing

The PSI dataset used in this work was processed by the German Aerospace Center (DLR). DLR was contracted in the framework of the German Ground Motion Service (BBD) for PSI-processing. PSI processing starts with the detection of PS candidates by thresholding the Signal-to-Clutter ratio (SCR) in the coregistered SAR data stack (Adam et al., 2004). Afterwards, the PS candidates are geocoded, and a grid with a cell size of about 1 km is created and superimposed onto the PS candidates. Based on the grid, the PS candidates with the highest phase stability are extracted from each grid cell. The extracted PSs build the basis of the reference network. For all arcs of the reference network (Goel et al., 2016), the height update, mean velocity, and the atmospheric phase screen (APS) are estimated. Now, a robust L1-norm network inversion is performed for outlier removal (Rodriguez Gozalez, et al., 2011, Adam, 2018), and a PS reference point is selected. Afterwards, the residual height, mean velocity, and the displacement time series are estimated for each PS in the reference network, by performing an L2-norm network inversion. After the removal of the estimated APS, all the PS candidates which are not included in the reference network are connected to the PSs from the reference network. Finally, for all PSs, the residual height, mean velocity, and the displacement time series are estimated relative to the PS reference point. Typically, PS are related to man-made structures (e.g., houses, bridges, railways, roads) or natural objects (rock outcrops, boulders). The Sentinel-1 SAR dataset used in this study covers the timespan from October 15, 2014 until July 1, 2017, and consists of 66 acquisitions, with an incidence angle of 40° in the middle of the study area and a satellite heading of 195° (descending orbit). An improved version of the 3

arc-second SRTM C-band DEM (Wendleder et al., 2016) was used to calculate and remove the topographic phase from the interferograms.

5.4.2 Conversion from v_{LOS} into v_{SLOPE}

PSI is a one-dimensional measurement technique, thus, the mean velocity and displacement time-series of a PS is measured in the satellites' Line-of-Sight (LOS). Positive LOS values represent a displacement towards the satellite, while respective negative LOS values represent a displacement away from the satellite. In order to use the LOS velocities with respect to the detection of displacements caused by landslides, a conversion of the LOS velocity vector (v_{LOS}) into slope direction (v_{SLOPE}) is performed (e.g., Cigna et al., 2013, Notti et al., 2011, Notti et al., 2014). The conversion is based on the assumption that the displacement is purely parallel to the maximum slope direction. The conversion is performed by using the following equations (Notti et al., 2014):

$$v_{SLOPE} = \frac{v_{LOS}}{C} \quad (1)$$

The C coefficient represents the sensitivity of the LOS vector to measure a displacement in slope direction. It is calculated by:

$$C = N \cdot (\cos(S) \cdot \sin(A - 90)) + E \cdot (-1 \cdot (\cos(S) \cdot \cos(A - 90)) + H \cdot (\sin(S)) \quad (2)$$

where A is the terrain aspect with respect to the North, and S is the slope angle. N, E, and H are the directional cosines of the LOS vector, and are calculated by using:

$$N = \cos(90 - \theta) \cdot \cos(180 - \alpha) \quad (3)$$

$$E = \cos(90 - \theta) \cdot \cos(270 - \alpha) \quad (4)$$

$$H = \cos(\theta) \quad (5)$$

where θ is the incidence angle and α is the satellite ground track angle (approximately -15 degrees for ascending orbit and approximately -165 degrees for descending orbit) plus 90 degrees. A digital elevation model (DEM) with a spatial resolution of 10 x 10 meters is used to calculate the terrain aspect and inclination of the slopes in the study area. The DEM is based on a compilation of different data sources (LiDAR, stereoscopic aerial imagery, and digitized topographic maps) and a vertical and horizontal accuracy of 0.5–2 m is reported (BKG, 2018). For areas with very low sensitivity, C values approach zero and the v_{SLOPE} tends to infinity, thus, in order to prevent an artificial exaggeration of the v_{SLOPE} , the C-value is fixed to -0.3 if $-0.3 \leq C < 0$ and to +0.3 if $0 \leq C \leq +0.3$. As a consequence, the v_{SLOPE} cannot be higher than 3.33 times vLOS. The vLOS scaling factor limit of 3.33 is based on (Herrerra et al., 2013), where a comparison of v_{SLOPE} values with differential GPS measurements has shown that this is an appropriate threshold.

5.4.3 Cluster Analysis

The result of the conversion is used as input for the cluster analysis. The cluster analysis uses v_{SLOPE} as an input variable for the detection of PS clusters. The cluster analysis is based on the null hypothesis that there is no association between v_{SLOPE} values in nearby PSs. The alternative hypothesis is that spatial clustering exists, meaning that nearby PSs have similar v_{SLOPE} values. The result of the cluster analysis is the local Moran's I Index, the z-score, the p-value, and the code characterizing the cluster type. The local Moran's Index (I_i) is calculated by using the following equations (Anselin, 1995):

$$I_i = \frac{x_i - \bar{X}}{S_i^2} \sum_{j=1, j \neq i}^n w_{i,j} (x_j - \bar{X}) \quad (6)$$

and:

$$S_i^2 = \frac{\sum_{j=1, j \neq i}^n (x_j - \bar{X})^2}{n-1} \quad (7)$$

where x_i is the v_{SLOPE} value for the i 'th PS, \bar{X} is the mean of the v_{SLOPE} of all PSs, n is the total number of PSs, and $w_{i,j}$ is the spatial weight between the PSs i and j . The spatial weight is based on an inversed square distance model to describe the spatial relationship. Thus, only close PSs have an influence on the local Moran's I Index. As the precision of the estimated PSI velocity decreases over distance mainly due to a residual tropospheric phase and error propagation (e.g., Ketelaar, 2009, Adam, 2018), an upper threshold of the neighborhood search radius of 200 m is set.

In order to assess the significance of the cluster analysis, a randomization procedure is performed. For this reason, the locations of the PSs are randomly reconfigured n times (in this case, $n = 499$). The distribution of local Moran's I Index based on these permutations is then compared with the local Moran's I Index computed from the original PS locations. By doing so, it is possible to assess the probability that the results of the cluster analysis come from a random distribution. By using 499 permutations, the smallest possible p-value is 0.002, meaning that the minimum of the calculated probability of being wrong (e.g., PSs are falsely classified as a cluster) is 0.2%. In this study, the upper threshold for the p-value is set at 5% to account for statistical significance of the detected PS clusters.

A high value of I_i indicates that a PS has similar v_{SLOPE} values as the neighboring PSs. In general, these PS clusters can consist of either positive or negative v_{SLOPE} values. Positive v_{SLOPE} values represent an uphill movement, and have been discarded. Although a vertical uplift may occur at the feet of landslides, the velocity vector in a slope direction (v_{SLOPE}) should remain downhill, because a dominant uphill movement, of very slow landslides, is not plausible. The result of the cluster analysis is statistically significant PS clusters, indicating downhill movement. These PS clusters are the input for the classification of the landslides' state of activity.

5.4.4 Classification of the Landslides' State of Activity

The velocity of a landslide can be correlated with the damage it may cause (Cruden, 1995). The International Union of Geological Sciences Working Group on Landslides established a classification of landslide velocities in order to extend the Landslide Report within the World

Landslide Inventory. This official classification of landslide velocities spans ten orders of magnitude. It consists of seven velocity classes, and ranges from 16 mm per year to 5 m per second (Cruden, 1995). The official classification is based on well-described landslides, where the peak velocity during an exceptional behavior phase and information regarding damages are available. A comparison between peak velocities and observed damages reports is that the peak velocity class, “extremely slow” (peak velocity \leq 16 mm per year), corresponds to “No damage to structures built with precautions”, and the peak velocity class, “very slow” (peak velocity \leq 1.6 m per year), corresponds to “Some permanent structures undamaged or, if they are cracked by the movement, they can be repaired” (Cruden, 1995). The relation between peak velocity and damage is not straightforward, because damage also depends on things like the internal distortion of the displaced mass, the margin of the displaced mass, and the type of landslide. Thus, the official velocity classes are schematic, because the peak velocity alone may not give a sufficient characterization of the landslide processes (e.g., at the margin of a landslide) (Cruden, 1995). However, it offers a practical method to include information on landslide velocity in a landslide report.

In contrast to the official landslide velocity classes, the PSI technique does not measure the maximum velocity during an exceptional behavior phase. PSI provides the mean velocity of several years in the direction of a Line of Sight. Consequently, the choice of a proper threshold is a key step, and needs to take the following aspects into account (Cigna et al., 2013): the type of the observed deformation process (e.g., geometry, expected velocity), technical characteristics of the PSI data (e.g., LOS geometry), and post-processing steps (e.g., reprojection of LOS velocity into slope velocity). Recent studies at a regional scale have used LOS velocity thresholds ranging from 1.5 to 10 mm per year to classify active landslides (Righini et al., 2012, Farina et al., 2006, Cascini et al., 2010, Bianchini et al., 2017). A literature review from Mansour et al., (2011) identified a threshold of 10 mm per year, where moderate damage is present at buildings and infrastructure. Righini et al. (2012), Bianchini et al. (2012) and Bianchini et al. (2013) used the 10 mm per year threshold to classify active landslides using advanced DInSAR data.

In this study, a threshold of 10 mm per year was used to classify active landslides. This choice was driven by the following reasons: The PSI-based velocity is a mean velocity over several years, while the official threshold of 16 mm per year discriminating “extremely slow” from “very slow landslides” (which correlates with damages) refers to peak velocities (Cruden, 1991). As observed by Cascini et al. (2010), peak velocity may significantly exceed the mean velocity. Thus, a mean velocity threshold should be lower than a peak velocity threshold. Furthermore, a threshold lower than 16 mm per year reduces the probability of discarding potentially active landslides, assuring that even slow landslides with certain damage potential are classified as active (Bianchini et al., 2012). On the other hand, the threshold must not be lower than the precision of the PSI dataset (Cascini et al., 2010), which needs to be controlled prior to the cluster analysis. The PSI dataset used in this study has an uncertainty of $2\sigma < 1.2$ mm per year caused by clutter (Rodriguez Gonzalez et al., 2017). Another reason not to use a very low threshold, such as 2 mm per year, is the conversion from LOS to slope direction. The conversion will amplify any noise in the PSI data, especially in areas with low sensitivity, such as slopes with an exposition approximately towards the North or the South.

In order to classify the landslides’ state of activity based on landslides mapped a priori, the result of the PS cluster analysis was intersected with the landslide polygons. If the maximum v_{SLOPE} value of a PS, belonging to a PS cluster that intersects with a landslide polygon, is faster

than 16 mm per year, the landslide is classified as “Active, very slow”. If the maximum v_{SLOPE} value of a PS, belonging to a PS cluster that intersects with a landslide polygon, is between 16 and 10 mm per year, the landslide is classified as “Active, extremely slow”. If the maximum v_{SLOPE} value of a PS in a landslide polygon is less than 10 mm per year, the landslide is classified as “Inactive”. If no PS cluster intersects with a landslide polygon, the polygon is classified as “Not classified”.

5.4.5 Ancillary Data

The a priori mapped landslide polygons used in the classification of the landslides’ state of activity is based on a landslide hazard indication map published by (LBM, 2018). The purpose of this map is to give an areal indication of landslide hazards on a scale of 1:50,000. The map includes 383 sliding areas with an average size of 0.152 km² (Figure 5.2A). The landslides are located between 80 and 427 m. a. s. l., the maximum slope inclination is 67°, and the average slope inclination is 22°. The distribution of the slope exposition of the landslide areas is shown in Figure 5.2B. It shows that 20.6% more landslide areas are facing to the West (260–280°) than to the East (80–100°). Generally, SAR data from ascending acquisitions are suitable for slopes facing to the East, where the movement direction is likely to be toward the East. SAR data from descending acquisitions are suitable for slopes facing to the West, where the movement direction is likely to be towards the West (Cigna et al., 2013). Thus, the descending satellite orbit is better suited for this study area.

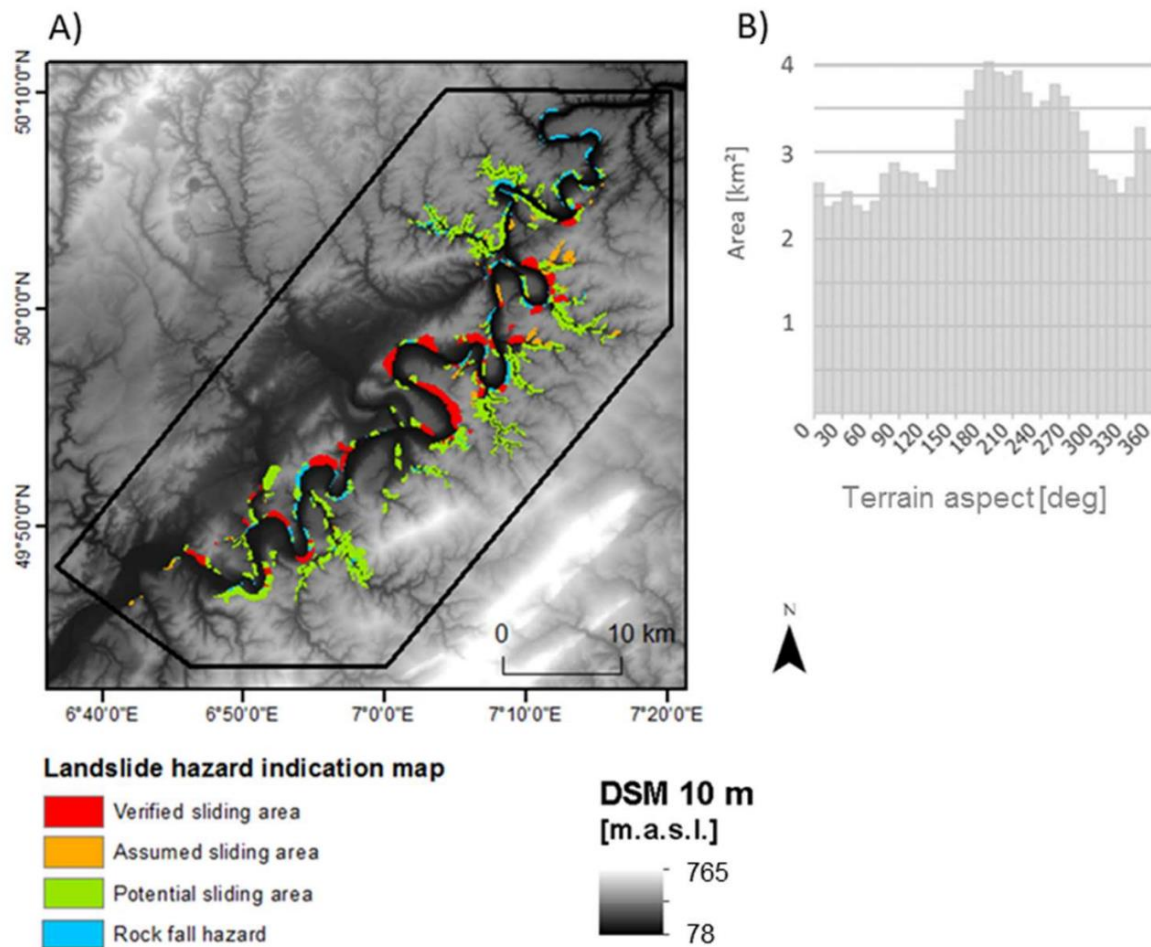


Figure 5.2: (A) Landslide hazard indication map (modified after (Rogall, 2014)). The boundary of the study area is shown by the black outline. A DEM © GeoBasis-DE / BKG 2018 (BKG 2018) serves as background. (B) The terrain aspect of all the sliding areas mapped in the landslide hazard indication map. East corresponds to 90 degrees, West corresponds to 270 degrees.

The landslide hazard indication map is based on archive documents of the state Geological Survey (Landesamt für Geologie und Bergbau Rheinland-Pfalz), stereoscopic aerial imagery, LiDAR data, and field surveys (Rogall, 2014). Visual image interpretation of the aerial imagery and geomorphological analysis of the LiDAR data were performed and verified by field surveys. The result categorized four landslide hazard indication classes: “verified sliding area”, “assumed sliding area”, “potential sliding area”, and “rockfall area”. A landslide is classified as “verified sliding area” if the sliding mass has pronounced differentiation of terrain humps, plain terrace surfaces, and head scarps. If such a landslide is located in a vineyard area, strong indications of active movements are often visible, such as roads with cracks, deformed walls, and tilted vine stocks. If the sliding mass has unclear geomorphological features, such as that the head scarp cannot be distinguished unambiguously, it is classified as “assumed sliding area”. Areas with a theoretical potential of landslides are classified as “potential sliding area”. The potential is derived by using datasets regarding the geological and geomorphological setting, and land use. It can be assumed that landslides occur in these areas only after large load changes or massive anthropogenic activities, such as terrain cuts. Areas with a significant

rockfall hazard are classified as “rockfall areas”, generally located at slopes with a mean slope angle of more than 45°. The landslide hazard indication map includes the rockfall source areas and the deposition areas (Figure 5.2).

The landslide hazard indication map does not include an in-depth landslide analysis or a risk assessment. However, the class “verified sliding area” is a strong indicator of recent or ongoing soil-creeping processes. Thus, a plausibility assessment of the classification of the landslides’ state of activity is performed by using the category, “verified sliding area”.

In order to verify the Sentinel-1 PSI data, eight PSs located at corner reflectors were compared with a series of nine differential GPS surveys. The corner reflectors were installed on October 6, 2010 and on October 12, 2011 to monitor an active landslide (Riedmann et al., 2015). The corner reflectors were installed to increase the PS density in this area. The area was of particular interest because of a road construction in the vicinity of the landslide. The dimension of the trihedral corner reflectors were specified to fit the requirements of PSI analysis based on TerraSAR-X Stripmap data from a descending orbit with an incidence angle of 43°. The construction design consisted of concrete with integrated metal plates to resist harsh weather conditions, vandalism, and theft. Although the dimension and orientation of the corner reflectors were chosen to meet the requirements of TerraSAR-X (X-band) acquisitions, the corner reflectors were detected as PS in the Sentinel-1 (C-band) dataset. For Sentinel-1, the average LOS displacement 2σ -error at the corner reflectors sites was 0.9 mm, the corresponding effective phase noise was 0.2 radians (2σ), and the signal-to-clutter ratio was 10.5. Six corner reflectors were located in an area classified as a “verified sliding area” in the landslide hazard indication map. Two corner reflectors were located outside a “verified sliding area” (Figure 5.3C and the corner reflector in the East in Figure 5.3B). The differential GPS surveys were conducted by the State Office for Mobility (LBM, 2018) and took place on the following dates: November 25, 2014, February 24, 2015, May 28, 2015, August 25, 2015, December 2, 2015, March 31, 2016, August 31, 2016, 08.2016, December 6, 2016, and March 22, 2017. A linear regression was performed to estimate the mean velocity in the directions of X, Y, and Z. For the comparison with the Sentinel-1 LOS velocity, the 3D GPS velocity vectors were projected into the direction of SAR LOS. In order to quantify the horizontal geocoding precision caused by satellite timing error and the APS of the SAR master scene, the mean deviation between the eight PSs at the corner reflectors and the precise position of the corner reflectors were calculated.

5.5 Results

In the study area, a total of 95,373 PSs were detected, resulting in an average spatial sampling density of 63.6 PS per km². The majority of PSs were located in cities, villages, and transport infrastructure (roads, railways, bridges) (Figure 5.3A). Stonewalls, guardrails, and street signs were present at these small roads and paths, and often corresponded to PSs. The landslide areas were often used for vinery and crossed by small roads and paths (Figure 5.3B).

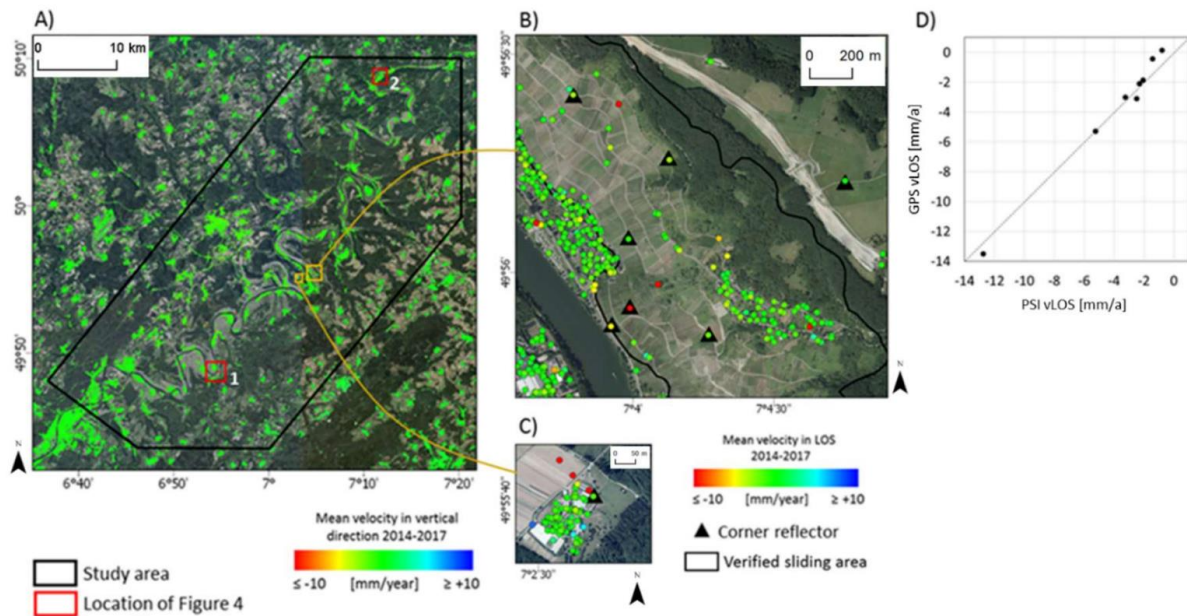


Figure 5.3: A) Overview of the spatial distribution of the persistent scatterers (PSs) in the study area. B) and C) shows the location of the corner reflectors used for verification of the Sentinel-1 Persistent Scatterer Interferometry (PSI) data. D) Shows the result of the verification of the Sentinel-1 PSI Line-of-Sight (LOS) velocity, versus the Global Positioning System (GPS) velocity at the corner reflector sites.

The verification results shows a mean difference between the PSI and GPS velocity of 0.49 mm per year ($2\sigma = \pm 0.37$ mm per year). A scatterplot visualizes the high correlation between PSI and GPS velocity (Figure 5.3D). Note that the GPS-based mean velocity (2014–2017) is based on nine measurement dates, while the PSI-based mean velocity (2014–2017) is based on 66 measurement dates. Although a linear displacement rate is assumed in both datasets, the difference in temporal resolution can bias a comparison of PSI and GPS velocities, if a strong non-linear displacement is present. The horizontal position of the eight PSs at the corner reflector sites had a mean deviation of 7.2 m with respect to the precise corner-reflector position.

The results of the conversion of the PSI LOS mean velocity into the mean velocity in slope direction is shown in Figure 5.4B and E, where positive mean velocities (representing an uphill displacement), as well as PSs located in flat areas (slope inclination $\leq 4^\circ$) are discarded meaning that the number of PSs is reduced by 78.3%. The consequence of this reduction is a reduced completeness in classification, but the exclusion of implausible v_{SLOPE} values is expected to increase the classification correctness. The results of this reduction and the results of the conversion are exemplarily shown in Figure 5.4A and D (before reduction) and in Figure 5.4B and E (after reduction). The PSs with a v_{LOS} mean velocity of approximately -10 mm per year present in the center of Figure 5.4A are affected very little by the conversion (Figure 5.4B). The reason for this is the slope exposition, which is very similar to the satellite heading and also similar to the slope angle to the SAR incidence angle. Consequently, the sensitivity of the SAR imaging geometry to measure displacements in slope direction is between 90% and 95% in this area. The strong impact of the LOS conversion for South-facing slopes is visualized in Figure 5.4D and E. Due to the low sensitivity in these areas, the C-value reaches its upper value of 0.3. The results of the conversion are the input for the subsequent PS cluster analysis. The results of the PS cluster analysis are exemplarily shown in Figure 5.4C and F. The cluster of PSs

characterizing a similar slope displacement, visible in the v_{SLOPE} map (Figure 5.4B and E), are successfully detected as a cluster (Figure 5.4C and F).

The result of the classification of the landslides' state of activity is shown in Figure 5.5. The classification result consists of 23 "active, very slow" landslides, 24 "active, extremely slow", 132 "inactive" landslides, and 204 "not classified" landslides. Thus, the landslides' state of activity is classified for 46.7% of all a priori mapped landslides. 25% of all "verified sliding areas" are not intersecting with a PS cluster. The PS cluster distribution for each landslide hazard indication area shows that 74% of the PS clusters are located in potential sliding areas and rock-fall hazard areas. The other 26% of the PS clusters are located in verified and assumed sliding areas. The landslides classified as "active, very slow" and "active, extremely slow" are compared against "verified sliding areas" based on the landslide hazard indication map. The comparison shows a good correlation, and thus confirms the plausibility of the result (Figure 5.6). All large "verified sliding areas" have been successfully classified as active landslides. In addition, the PSI-based classification has classified several large areas mapped as a "potential sliding area" in the landslide hazard indication map (Figure 5.2) as "active, very slow" or "active, extremely slow", such as in the southern and the northern part of the study area (white arrows in Figure 5.6).

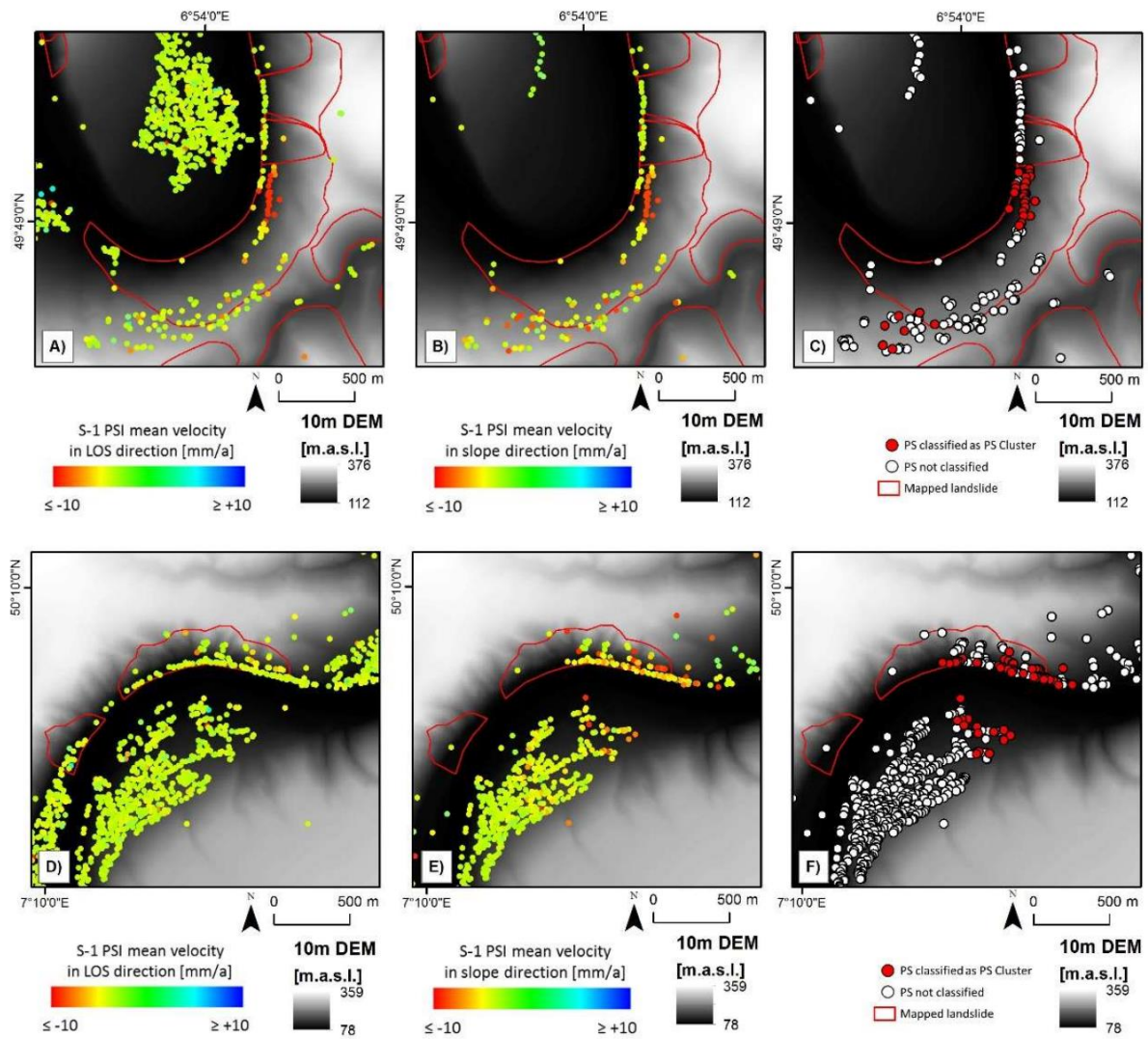


Figure 5.4: A) and D) visualize the Sentinel-1 PSI mean velocity in the LOS direction. B) and E) show the results of the conversion in a slope direction. PSs indicating uphill motion and PSs in flat areas are discarded. C) and F) show the results of the PS cluster analysis. The location of A), B) and C) is indicated in Figure 5.3A, number 1. The location of D), E) and F) is indicated in Figure 5.3A, number 2. A DEM © GeoBasis-DE / BKG 2018 serves as background.

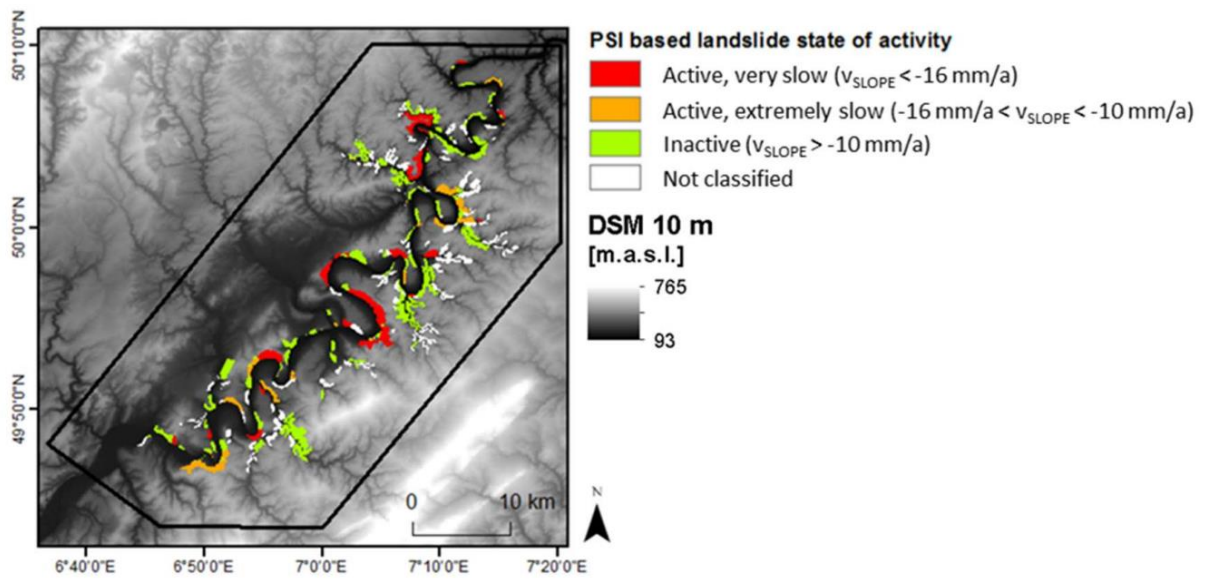


Figure 5.5: Result of the classification of the landslide state of activity based on Sentinel-1 PSI data. A DEM © GeoBasis-DE / BKG 2018 serves as background.

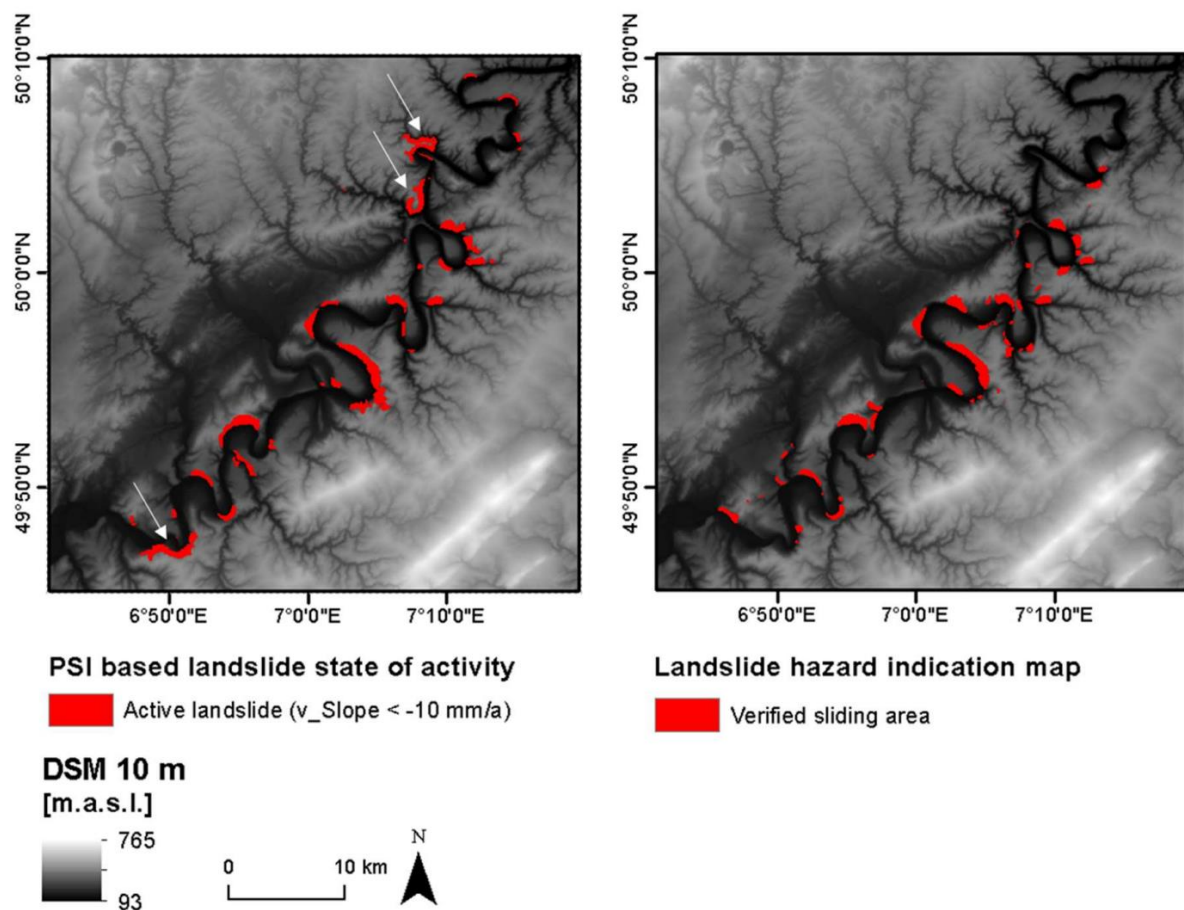


Figure 5.6: Verification of the classification result regarding “active landslides” (A) with “verified sliding areas” from the landslide hazard indication map (B). A DEM © GeoBasis-DE / BKG 2018 serves as background.

5.6 Discussion

In this work, two PSI post-processing steps were performed in order to classify active and inactive landslides on a regional scale. These steps were performed with the intention to adapt the PSI processing results to the specific requirements for the routine monitoring of a priori known areas with a landslide hazard indication. Certain characteristics and limitations were associated with the post-processing steps, which are discussed as follows.

First, the LOS velocity was converted to the slope direction based on the assumption that the landslide motion is purely parallel to the slope direction. This is plausible for things like planar slides, but not for rotational slides, where a significant vertical motion component at the top of the slide can be present. In such a case, the v_{SLOPE} is overestimating the real velocity in slope direction, because a vertical velocity component is present. The second issue regarding LOS conversion is the overestimation of the slope velocity in areas with low sensitivity. These are slopes with an exposition approximately to the North or to the South, or slopes with an inclination perpendicular to the SAR incidence angle. In order to mitigate this effect, the C-Index was fixed to -0.3 if $-0.3 \leq C < 0$ and to +0.3 if $0 \leq C \leq +0.3$, as proposed by (Herrerra et al., 2013). The consequence of this is that the velocity in slope direction cannot be higher than 3.33 times the LOS velocity. The third issue regarding the LOS conversion is that any noise in the LOS velocity is amplified by the conversion. Thus, a high measurement precision of the PSI processing results is a precondition for the conversion.

If multiple-PSI dataset with different observation geometries is available, such as from an ascending and descending orbit, the projection into slope direction could be improved. This could be achieved by estimating the vertical and the horizontal velocity vectors based on ascending and descending LOS observations. The estimated vertical velocity can then be used to improve the approximation of the velocity vector in the slope direction.

Detection of a PS cluster was performed to only classify landslides with a strong indication of a downslope motion as active. The rationale behind this approach was that the motion of a single PS could be due to a local process, such as building settlement. If several adjacent PSs showed a downslope motion, a strong indication regarding an active landslide is present. The drawback of the clustering approach is reduced classification completeness, as landslides with only one PS or heterogeneous v_{SLOPE} values are not classified. When two or more PS clusters with significantly different velocities are present in one landslide area, the extraction of one single velocity can be inappropriate. In such cases, a segmentation of the landslide area into two or more areas with different deformation characteristics can be performed (Righini et al., 2012).

Regarding the LOS velocity threshold to classify active landslides, recent studies have used thresholds in the range of 1.5 to 10 mm per year (e.g., Farina et al., 2006, Cascini et al., 2010, Righini et al., 2012, Bianchini et al., 2012, Bianchini et al., 2017). In this work, a v_{SLOPE} threshold of 10 mm per year was used. This threshold was chosen because the LOS velocity was converted into the slope direction, causing an amplification of the noise of the LOS data and potential exaggeration of the v_{SLOPE} in areas with low sensitivity (e.g., North- and South-facing slopes). Another approach regarding the choice of a velocity threshold is the use of training data. If such data are available from field surveys or in situ measurements, the PSI

velocity threshold can be determined by the highest number of agreements between the PSI-based activity classification and field-based observations.

A general limitation regarding the use of PSI to detect landslide displacements is the lack of PSs in the landslide area. The main reason for the lack of PSs is there being no geometrical visibility due to the local topography and LOS orientation, vegetation cover, and fast movements.

The geometrical visibility of a slope is a function of its exposition and slope angle, with respect to the SAR acquisition geometry. Due to foreshortening, layover and shadowing the amount of PSs can be significantly reduced. The use of SAR acquisitions taken from different orbits at different incidence angles increases the potential of high geometrical visibility.

A dense vegetation cover significantly limits the amount of PSs, because it causes a temporal decorrelation of the interferometric phase. If the phase decorrelation exceeds a certain threshold, no information is left, and the interferometric phase becomes random. Through the installation of corner reflectors or active transponders, the number of PSs in vegetated or agricultural areas can be increased (Figure 5.3B). Obviously, corner reflectors or active transponders cannot overcome the lack of PSs in archived SAR datasets, because the detection of PSs at corner-reflector or active-transponder sites can be achieved only after their installation.

The detection of PSs is limited for fast-moving landslides, due to an aliasing effect caused by the ambiguity of the interferometric phase. Therefore, the upper velocity limit of PSI is a quarter of a wavelength between two successive acquisitions. The time interval between two successive acquisitions is given by the satellite revisit time. Considering revisit time and wavelength, the maximum detectable velocities are 14.7 cm per year for ERS/Envisat (C band), 42.6 cm per year for Sentinel-1 12 day image pairs (C band), 25.7 cm per year for TerraSAR-X (X band), and 46.8 cm per year for ALOS (L band) (Crosetto et al., 2015). These are theoretical values, but in practice, the ability to detect fast displacements depends on various aspects, such as the noise level of the data, the specific phase-unwrapping technique, the spatial pattern of the deformation phenomena (the smoother the pattern, the better), and the PS density over this phenomena (the higher the density, the better) (Crosetto et al., 2015, Van Leijen, 2014). Besides aliasing, another limitation of SAR interferometric methods is encountered when the strain rate reaches half a wavelength per resolution cell in the time consecutive observations (Rosen et al., 2000). The use of other SAR processing techniques, such as SAR feature tracking (Werner et al., 2001) or range split spectrum interferometry (Shi et al., 2017) to detect fast-moving landslides, could extend the detectable velocity range of the PSI technique. However, these techniques provide spatial resolutions and accuracies which are approximately one order of magnitude worse than advanced DInSAR techniques, which limits their applicability to fast and large landslides.

5.7 Conclusion

This work presented a PSI post-processing workflow for the classification of landslides' states of activity on a regional scale. A PS cluster was proposed as a precondition for the classification of the landslide activity. The PSI dataset was verified by GPS measurements and showed a high

correlation (mean difference: 0.49 mm per year). This result shows the operational readiness of the Sentinel-1 SAR mission to detect landslide displacements. Sentinel-1 is of particular interest, because there are several recently ongoing efforts regarding the buildup of nationwide ground motion services based on this SAR mission, such as in (Dehls, 2017, Oyen, 2017, Kalia et al., 2017).

The classification result consisted of 23 “active, very slow” landslides, 24 “active, extremely slow”, 132 “inactive” landslides, and 204 “not classified” landslides. The landslides classified as “active, very slow” and “active, extremely slow” were compared against “verified sliding areas” based on a landslide hazard indication map, and results show a good correlation (Figure 5.6). Furthermore, several “potential sliding areas” (mapped in the landslide hazard indication map) were classified as “active landslides” (based on PSI data), and public authorities could use this information to extend the monitoring efforts by installation of in-situ sensors for comprehensive monitoring on a local scale, or field surveys in these areas (e.g., areas marked with white arrows in Figure 5.6).

After verification by field surveys, the updated landslide inventory can enhance landslide susceptibility assessments, which can then be used for a landslide risk analysis and risk management, in order to improve DRR. A paradigm change regarding the use of advanced DInSAR techniques from single retrospective data products, to joint analysis of multiple SAR datasets from different SAR sensors covering consecutive timespans (Righini et al., 2012, Cigna et al., 2013), towards a monitoring technique with continuously updated displacement information feeding a database (Raspini et al., 2018) based on a single SAR mission, shows the increasing capability of advanced DInSAR techniques. This capability can be used to routinely produce classifications of landslides’ states of activity for an improved DRR. The use of (semi-) automated workflows for updating landslide inventories is of particular interest in the context of nationwide, advanced DInSAR datasets with millions of measurement points. Manual data analysis and visual interpretation makes the process subjective and time-consuming. The automatization and implementation of the proposed workflow within the framework of the BBD is under discussion.

5.8 Acknowledgements

This work was realized in the framework of the project “Ground Motion Service Germany”. It is funded by the Federal Institute for Geosciences and Natural Resources (BGR). The figures contain modified Copernicus Sentinel-1 2014-2017 data. Sentinel-1 data was kindly provided by the European Space Agency (ESA). The German Aerospace Center (DLR) is contracted and acknowledged for the PSI processing. Ansgar Wehinger from the State Office of Geology and Mining Rhineland-Palatinate (LGB-RLP) is acknowledged for providing the landslide hazard indication map. The State Office for Mobility in Rhineland-Palatinate (Landesbetrieb Mobilität Rheinland-Pfalz) is acknowledged for provided the GPS data. Three reviewers are acknowledged for their constructive comments.

6 Landslide activity detection based on Sentinel-1 PSI datasets of the Ground Motion service Germany - The Trittenheim case study

This chapter was published as:

Kalia, A. C. (2022): Landslide activity detection based on Sentinel-1 PSI datasets of the Ground Motion Service Germany - the Trittenheim case study. *Landslides*, <https://doi.org/10.1007/s10346-022-01958-9>

6.1 Abstract

Spaceborne interferometric synthetic aperture radar has been proven to be able to monitor slow deforming landslides with mm-precision. Continental- and nationwide-scale Sentinel-1 PSI (persistent scatterer interferometry) datasets with millions of deformation time series are publicly available, e.g., via the European Ground Motion Service or the Ground Motion Service Germany. This creates the possibility for an increased routine use of PSI for landslide applications. However, the use of PSI datasets is often done by visual inspection. The huge amount of measurements makes visual inspection, subjective, time-consuming, and error prone due to outliers. This study demonstrates how spatial and temporal patterns of the PSI velocity and time series can be detected in a semi-automatic way to improve objective information extraction. Therefore, two landslides, namely, Trittenheim and Piesport landslides, in Germany are analyzed using Sentinel-1 PSI datasets from the Ground Motion Service Germany. The postprocessing technique semi-automatically detects spatial clusters of deforming PS with a maximum LoS velocity of 18 and 7 mm/a in Trittenheim and Piesport landslides, respectively. Furthermore, a correlation and time-lag between the surface deformation and a potential triggering factor is found. Results show that an increase in climatic water balance accelerates landslide deformation at the investigated locations. Results are verified by a second independent Sentinel-1 PSI dataset from the Ground Motion Service Germany.

6.2 Introduction

Landslides are natural hazards causing damage to infrastructure, economic losses, and can lead to loss of life (Froude and Petley, 2018). Advanced differential interferometric synthetic aperture radar (A-DInSAR) techniques, e.g., PSI (persistent scatterer interferometry), have been proven to be useful for long-term monitoring of slow moving landslides with weekly to monthly sampling and mm-precision (Feretti et al., 2001, Zhao and Lu, 2018, Solari et al., 2020). Regional (Raspini et al., 2018) and nationwide A-DInSAR datasets based on Sentinel-1 SAR data are publicly available in various regions and countries (Dehls, 2017, Kalia et al., 2017, 2021). Continental-scale A-DInSAR datasets are provided by the European Ground Motion Service (Costantini et al., 2022). A review of these services is given by Crosetto et al. (2020). The frequency of the update of these datasets ranges from every consecutive Sentinel-1 acquisition (Raspini et al., 2018) to yearly updates (Kalia et al., 2021, Constantini et al., 2022). Due to the regular updates, state-of-the-art A-DInSAR processing, and open data policy of these services, operational information products for specific applications like landslide hazard assessment become possible. The use of the large A-DInSAR datasets is often done by visual inspection of the velocity field and the time series. The huge amount of measurement points (e.g., persistent scatterer, PS) makes visual interpretation, subjective, time-consuming, and error prone due to outliers. The question arises how spatial and temporal patterns of the PSI velocity and time series can be detected in a semi-automatic way. Therefore, several InSAR post-processing techniques have been proposed by the scientific community, e.g., based on a sequential series of statistical tests to classify PS time series into pre-defined classes (Berti et al., 2013) or machine learning to estimate the probability of accelerations/decelerations induced by slope instability and subsidence (Confuorto et al., 2022). Chaussard et al. (2014) use

temporal mode principal component analysis (PCA) to compute a set of uncorrelated principal components ranked by the percentage of variance explained and constrained by an orthogonal basis, which effectively captures variance but may overlook and mix some data trends. Cohen-Waeber et al. (2018) use independent component analysis (ICA) to maximize the statistical independence of an arbitrary number of independent components. Other techniques include, e.g., the inverse velocity approach to estimate the time of slope failure (Carlà et al., 2019), wavelet analysis to quantify and correlate (intermittent) periodical signals (Haghshenas and Motagh, 2016, Tomás et al., 2016, Liu et al., 2022), and spatial clustering to identify clusters of deforming PS and/or distributed scatterers (Lu et al., 2012, Barra et al., 2017, Xi, 2017, Kalia, 2018). However, the spatial and temporal characteristics of A-DInSAR datasets vary by orders of magnitude (depending on the number of acquisitions, the spatial measurement density), which can have an influence on the ability of these post-processing techniques regarding the extraction of meaningful information. Thus, the scalability of three post-processing techniques (Berti et al., 2013, Barra et al., 2017, Liu et al., 2022) are assessed in this work. Therefore, all three post-processing techniques are applied and parameterized using a Sentinel-1 PSI dataset from descending track 139 which is processed in the framework of the Ground Motion Service Germany. Subsequently, the same techniques and parameters are evaluated on a second independent Sentinel-1 PSI dataset from descending track 37, which is also processed in the framework of the Ground Motion Service Germany. The rationale for the use of these three post-processing techniques is as follows. First, clusters of deforming PSs are detected to focus the attention of an end-user to specific areas of the PSI dataset characterized by a high reliability. Second, an exemplarily chosen PS time series, within this specific area, is analyzed regarding a time-lag to a potential triggering factor. The climatic water balance (climatic water balance = precipitation – potential evapotranspiration, Thornthwaite and Mather, 1957) is used as potential triggering factor, instead of the often used precipitation, because the deep seated sliding surface is approximately 100 m below the Earth's surface in the investigated landslides. Thus, it is hypothesized that rainfall water can reach the sliding surface (and cause an acceleration of the deformation by decreasing the friction coefficient at the sliding surface) only in times with high precipitation and low evapotranspiration.

6.3 Sentinel-1 PSI dataset and study area

6.3.1 Sentinel-1 PSI dataset

This study is based on wide-area Sentinel-1 PSI datasets from two tracks of the Ground Motion Service Germany (Kalia et al., 2021). The PSI data used in this study is part of the 3rd update of the German Ground Motion Service (released on 12.04.2022). The PSI technique (Feretti et al., 2001) belongs to the group of advanced differential interferometric stacking techniques. The PSI technique uses a stack of wrapped interferograms, all referring to a single reference image, to estimate the residual ellipsoidal height, deformation rate, and time series for coherent pixels (persistent scatterer, PS). The estimates are relative to a reference point and surface deformations are measured in the satellites line-of-sight (LoS) direction. The wide-area Sentinel-1 PSI processing is performed by a modified version of the PSI GENESIS processor (Adam et al., 2013, Goel et al., 2016, Adam, 2019). The modifications include geodetic corrections, e.g., plate tectonic motion, solid earth tides (Rodriguez Gonzalez et al., 2018), and

tropospheric phase mitigation by a simulation and subtraction of the tropospheric delay using the ECMWF (European Centre for Medium-Range Weather Forecasts) ERA-5 numerical weather forecast model (Adam, 2019). The modifications are set-up that it is able to provide a high precision of deformation rate estimates, even over rural areas and large distances, e.g., more than 100 km (Parizzi et al., 2021). An improved version of the 3 arc-second SRTM C-band DEM (Wendleder et al., 2016) was used for topographic phase correction. After PSI processing a Global Navigation Satellite System (GNSS) calibration (Parizzi et al., 2020) was applied to tie the PSI results to the same geodetic reference frame. The GNSS velocities used for calibration are based on post-processed GNSS time series data from 243 continuous GNSS stations from the SAPOS network spread across Germany (Brockmeyer et al., 2021 unpublished). Table 6.3.1 shows the characteristics of the Sentinel-1 PSI data used in this study. Figure 6.1 shows the footprint of the processed Sentinel-1 PSI datasets used in this case study. The Sentinel-1 PSI dataset based on track 139 is used for parametrization of the post-processing techniques. Subsequently, the parameterized post-processing techniques are applied to the PSI dataset based on track 37 to assess the transferability of the post-processing techniques.

Table 6.3.1: Characteristics of the Sentinel-1 SAR datasets used for PSI processing

Direction/track	Incidence angle* θ [°]	Heading angle α [°]	Timespan [dd.mm.yyyy]	Acquisitions [#]
			01.04.2015 - 30.12.2020	
Desc/139	40.7	186.3	06.04.2015 -	279
Desc/037	31.5	185.9	29.12.2020	291

* at the center of the study area

6.3.2 Study area

The study area has a size of 30 km² and is located at the river Moselle in Germany (Fig. 6.1). River Moselle flows roughly from south-west to north-east. River Moselle is meandering strongly through the Hunsrück Slate (Devonian strongly tectonically modified clay-slate, Rogall, 2014) and fluvial erosion is producing undercut slopes. The undercut slopes are not in gravitational equilibrium. Very slow (1.6 m/a > landslide velocity > 16 mm/a) and extremely slow (< 16 mm/a) landslides with deep seated sliding surfaces and extremely rapid (5 m/s) rock falls are present in the study area (Cruden and Varnes, 1996, Rogall, 2014). The elevation range is from 78 m to more than 400 m above sea level. Two landslides are investigated in this case study, the “Piesport landslide” and the “Trittenheim landslide” (Fig. 6.1B). The exposition of these landslides varies from south, south-west (Piesport landslide) to north, north-west (Trittenheim landslide). Due to the heading angle of the satellite orbit, in some parts of the landslides, with an exposition approximately north–south the LoS sensitivity to measure a downslope motion is zero. The Sentinel-1 PSI dataset from track 139 shows three clusters of moving PSs (indicated by red arrows in Fig. 6.2A). These are also visible in the Sentinel-1 PSI dataset from track 37 (Fig. 6.2B). In the study area, 3993 PS are detected using track 139 and 4632 PS using track 37. PSI velocities range from -18.01 to $+2.46$ mm/a (track 139), resp. from -14.41 to $+3.08$ mm/a (track 37). Highest PS densities are in built-up areas, e.g., the villages Trittenheim, Neumagen-Dhron, Piesport, and Minheim (Fig. 6.2). Most of the landslide areas

are covered by vineyards, intersected with small roads, traffic signs, and railings. The upper parts of the landslides are mostly covered by forest. At the lower part of the Piesport and at the top of the Trittenheim landslide, a village is located (Fig. 6.2C). This built-up infrastructure causes a coherent point scattering in the SAR time series. In consequence, these pixels are detected as PS during the PSI processing. In general, different objects and processes (e.g., railing, stonewall, soil creeping, sliding mass) can contribute to the reconstructed deformation time series of the PS phase center. Figure 6.3 shows the PSI LoS velocity and an exemplary PS deformation time series from track 139 and 37 at the Trittenheim landslide. The estimated velocities and the time series pattern from track 139 and 37 are very similar. Due to the shallower incidence angle of track 37, the LoS sensitivity to measure a downslope vector is higher than from track 139. Both time series show an acceleration in the beginning of 2020 (Fig. 6.3). The Trittenheim landslide has a width of 500 m and a length of 1.700 m. The upper scarp has a height of up to 25 m with an inclination of 45–60°. The landslide type can be characterized as deep-seated continuous creep. The landslide can be differentiated into three sections: a rupture area, a middle deformation zone, and a landslide toe. The sliding surface is several tenth of meters below the Earth's surface. At nearby similar landslides, the sliding surface was drilled at 55 and 65 m below the Earth's surface. The subsurface of the landslide consists of the Hunsrück Slate. At the bottom of the landslide, a main road the so-called K86 is present. Several roads show distinct cracks, dry stone walls are tilted, and river Moselle has been narrowed by 25 m, indicating a landslide deformation over long time spans. In the 1990s, the Trittenheim Bridge has been reconstructed due to damages caused by deformation of the landslide. It has to be noted that no recent terrestrial measurements exist in this area, and land clearance activity alongside newly builtup roads did not show recent cracks and deformations, thus, the current state of activity is unknown to public authorities (Rogall, 2014). The Piesport landslide is one of the largest landslides in the Moselle Valley. It has a width of 2.700 m and a length of 700 m. The upper scarp has a height of 30–40 m and a steep slope with an inclination of 80°. The landslide type can be characterized as deep-seated continuous creep. In the eastern part of the Piesport landslide, distinct cracks and deformations of retaining walls and roads are observed (Rogall, 2014). The deformation of the sliding mass in the eastern part has led to a narrowing of 30 m in this part of river Moselle. While active landslide deformations are confirmed in the eastern part, the western part is considered inactive (Rogall, 2014).

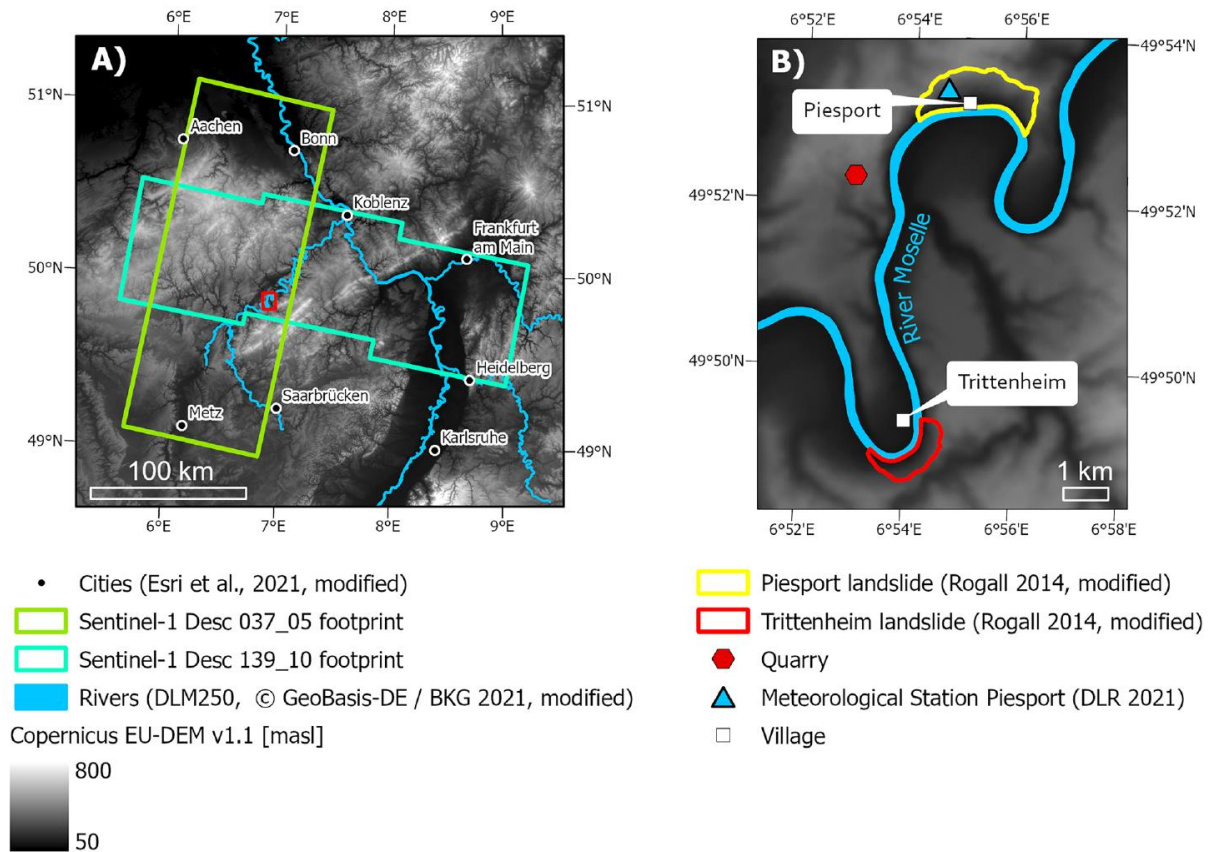


Figure 6.1: Location of the processed Sentinel-1 PSI datasets from track 139 and 37 (A), location of study area and the Piesport- and Trittenheim- Landslide (B). The red inset in A shows the extent of B). A digital elevation model serves as background

6.4 Methodology

This paper uses three different methods to analyze PS deformation time series. Active deformation area (ADA) mapping described in the “Active deformation area mapping” section is used to identify significantly deforming clusters of PS time series. Then, a series of statistical tests, described in the “Time series classification” section, are applied to the PS time series to (i) identify an acceleration date and (ii) quantify a time-lag w.r.t. a potential landslide triggering factor. Finally, a wavelet analysis is performed to analyze correlation and time-lag between intermittent periodical signals of surface deformation and potential landslide triggering factor. All results are verified by a second independent Sentinel-1 PSI dataset, from another track of the Ground Motion Service Germany.

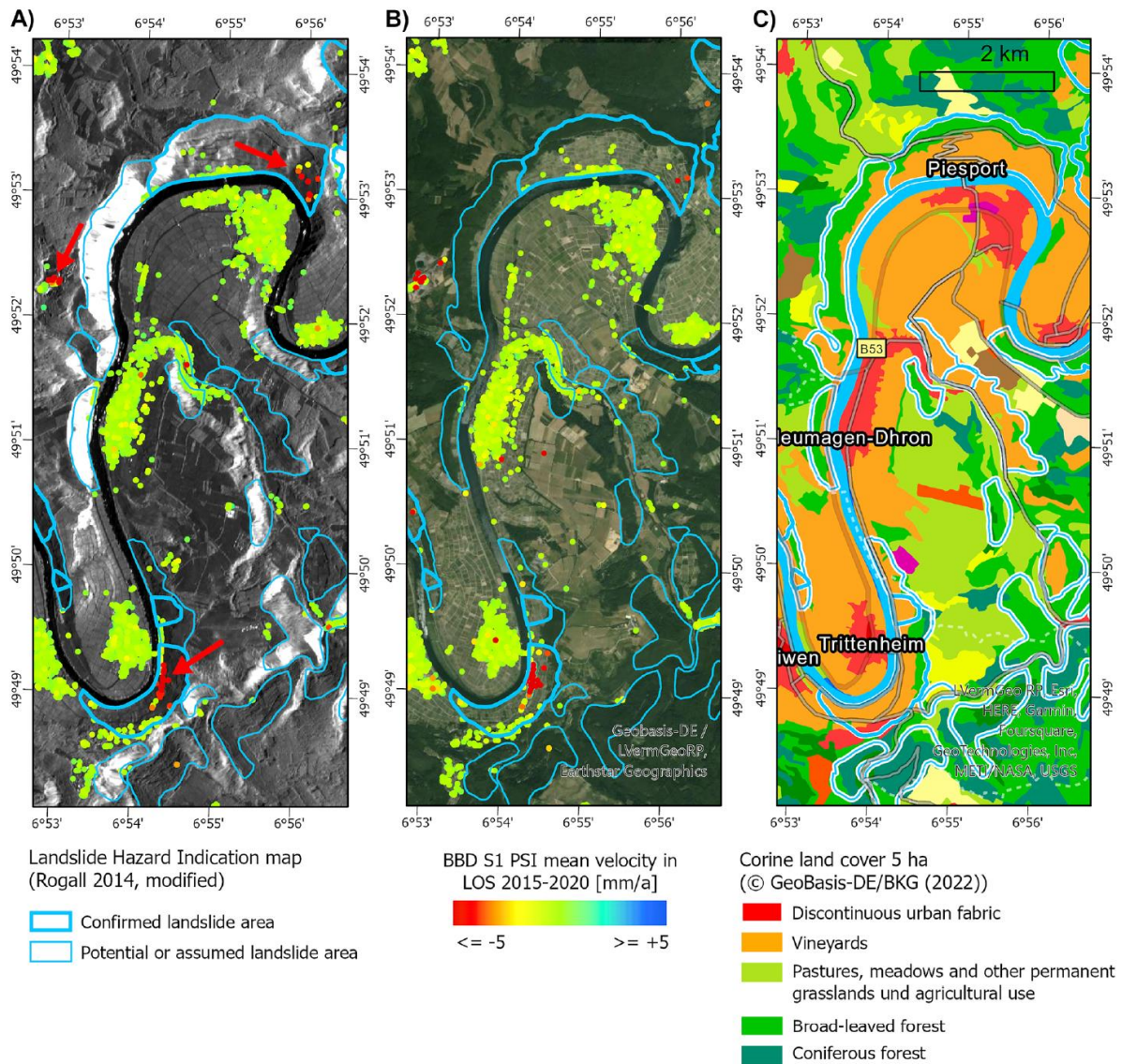


Figure 6.2: Sentinel-1 PSI dataset from track 139 superimposed on the temporal mean amplitude image (A), Sentinel-1 PSI dataset from track 37 superimposed on the temporal mean amplitude image (B), ESRI hybrid reference layer superimposed on Corine landcover 5 ha (C). A landslide map (Rogall, 2015) is superimposed in (A), (B) and (C).

6.4.1 Active deformation area mapping

The mapping of active deformation areas (ADA) is proposed by Barra et al. (2017), Tomás et al. (2019), and Navarro et al. (2019). The ADA can be obtained by the software ADA Tools developed by Navarro et al. (2019). The rationale behind the ADA detection is that a loss of few information is accepted in order to (i) decrease the general noise level and (ii) increase the usability of InSAR stacking results. The ADA-mapping approach consists of two steps (i) ADA detection and (ii) ADA extraction. The ADA detection starts with a filtering of the PS deformation time series regarding isolated, single PSs, noise PSs, and spatial outliers. Therefore, a priori defined thresholds regarding the maximum distance used to define a PS as isolated and the accepted noise-level are used. The spatial criteria is based on two conditions

and uses a moving window around the PSs (e.g., twice the spatial resolution of the input SAR data). The first condition is based on the presence of at least one more PS within the search window. The second condition is that at least two PS are moving within the search window. The threshold used to classify a moving PS is based on the standard deviation (σ) of the deformation rate of all PSs. The initial parameters suggested by Barra et al. (2017) uses a threshold of 1.5σ . If the absolute value of the deformation rate is higher than the threshold, it is classified as “active”, otherwise, it is considered as “stable.” PS classified as “active” are the input for the next step, the ADA extraction. The ADA extraction begins with the construction of a circular polygon around the “active” PS. Then the intersecting polygons are merged to form a spatial cluster of PS. If the cluster consists of a minimum number of PS, it is considered as a significant deformation area. For each extracted ADA, several attributes are included, e.g., the number of aggregated PS, mean, maximum and minimum deformation rate of the aggregated PS, and a quality index. The purpose of the quality index is to provide information on the reliability of each ADA. It is based on a combination of the spatial and temporal noise of the aggregated PS.

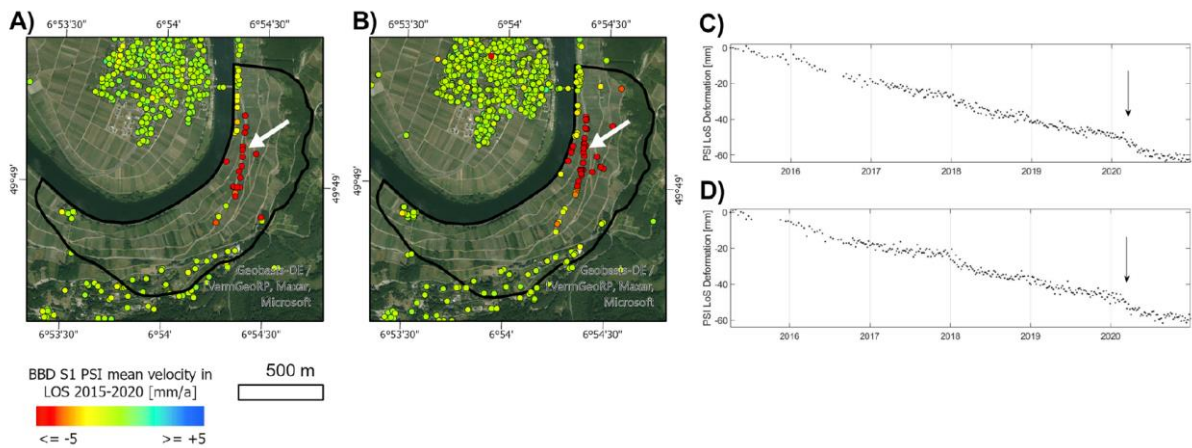


Figure 6.3: Sentinel-1 PSI LoS velocity from track 139 (A) and track 37 (B). Corresponding deformation time series based on track 139 (C) and based on track 37 (D). The location of the deformation time series is indicated by the white arrows in A) and B). An acceleration in the beginning of 2020 is visible in both deformation time series (black arrow in C) and D))

6.4.2 Time series classification

In order to semi-automatically extract information from the PS time series, a series of conditional sequence of statistical tests is performed using the method proposed by Berti et al. (2013). The approach classifies the PS time series into six a priori defined deformation classes: “uncorrelated,” “linear,” “quadratic,” “bilinear,” “discontinuous with constant velocity,” and “discontinuous with variable velocity.” In this case study, the focus is in particular to identify PS with an acceleration and to semi-automatically extract the date when the acceleration began. This time series pattern corresponds to the class “bilinear.” Given that the PS time series has a significant linear trend, a bilinear model is tested. Therefore, a changepoint regression is used. A changepoint regression, also known as piecewise or segmented regression, divides the time series into intervals and a separate linear regression is fitted for every interval (Main et al.,

1999, Steven, 2001). The segments are used to identify whether a change in the slope exists and when the change occurs. Based on the approach proposed by Main et al. (1999), the PS time series t_1, \dots, t_n is split into two intervals, divided by a breakpoint t_b . The breakpoint is moved along the time series from $b = 5$ to $b = n-5$, with $n =$ number of deformation measurement. Thus, a minimum of 5 deformation measurements are required to build an interval. This threshold has been chosen, to prevent very short intervals at the beginning or at the end of the PS time series. For every breakpoint, a two-line unconstrained model is fitted for the intervals t_1, \dots, t_b and t_{b+1}, \dots, t_n and the Bayesian information criterion (BIC, Schwarz, 1978) is calculated to assess the goodness of fit:

$$\text{BIC}(t_b) = \ln\left(\frac{\text{RSS}}{n}\right) + \frac{(k+1)}{n} \ln(n)$$

where RSS is the residual sum of squares and k is the number of model parameters (in the case of a two-line regression $k = 3$). The BIC is also calculated for a single linear and a quadratic regression (BIC_L and BIC_Q , with $k = 1$ and $k = 2$). The BIC is used for model selection and uses a penalty term for the number of parameters in the model. By doing so, the BIC approaches overfitting by finding the best model that is fitting the data (low RSS value) using only a few parameters (low k). If the minimum value of $\text{BIC}(t_b)$ is smaller than BIC_L and BIC_Q , the bilinear regression outperforms the quadratic and linear regression (Berti et al., 2013). The date of the minimum value of $\text{BIC}(t_b)$ is the date of the breakpoint for the bilinear regression.

6.4.3 Wavelet analysis

In order to analyze potential (intermittent) periodical signals of the PS time series, a wavelet analysis is performed (Grinsted et al., 2004). As only the non-linear component of the PS time series is of interest in the wavelet analysis, the original PS time series is decomposed into two components (a linear and a non-linear component). The linear component is estimated by using a least squares fitting. The residuals of this linear trend are assigned as the non-linear component. First, a continuous wavelet transform is used because it is capable to detect periodical patterns in low SNR time series. The continuous wavelet coherence is calculated as follows (Grinsted et al., 2004):

$$W_t(\tau, s) = \int_{-\infty}^{\infty} x(t) \Psi_{\tau, s}^*(t) dt \quad \tau, s \in \mathbb{R}, s \neq 0$$

where Ψ is the daughter wavelet, Ψ^* is the complex conjugate of Ψ , τ is the translation parameter and s is the scaling factor. The result of the continuous wavelet coherence is visualized as a 2D graph with the X-axis representing the date of the time series and the Y-axis representing the frequency of the periodical signals. High power values, visualized in the 2D graph indicates the existence of significant periodical patterns at corresponding timespans.

In order to analyse potential periodical similarities between two time series, a cross wavelet transform and a wavelet coherence is calculated. The cross wavelet transform is calculated by multiplication of the first continuous wavelet transform (based on the PS time series) with the complex conjugate of the second continuous wavelet transform (based on the climatic water balance). The resulting amplitude has high values where both continuous wavelet transforms have high values. These high values represent time-spans where both time series have an (intermittent) periodical signal. The resulting phase represents a potential time lag between two (intermittent) periodical signals. The cross wavelet transform is calculated as follows (Liu et al., 2011):

$$W_{xy}(\tau, s) = W_x(\tau, s) W_y^*(\tau, s)$$

where W_y^* is the complex conjugate of W_y , and the power spectrum of the crossed wavelet is $|W_x|^2$.

The wavelet coherence is defined as coherence of the two continuous wavelet transforms. It is calculated by the normalized cross-correlation coefficient and a scaling factor between the two continuous wavelet transforms. The wavelet coherence can show additional similarities between two (intermittent) periodical signals, compared to the cross wavelet transform. The wavelet coherence is calculated as follows (Nourani et al., 2019):

$$R_{xy}(\tau, s) = \frac{|S(W_{xy}(\tau, s))|}{\sqrt{|(S(W_x(\tau, s)))|^2 |(S(W_y(\tau, s)))|^2}}$$

where S is a smoothing operator. The difference between cross wavelet transform and wavelet coherence is that the cross wavelet transform performs best when the power level of the signal is similar in both continuous wavelet transforms. On the other hand, the wavelet coherence is able to deal with different signal power levels, because of a normalization and smoothing. As a consequence, the wavelet coherence has a lower resolution in space and time with regards to the cross wavelet transform but can handle different levels of signal power.

In the case study two continuous wavelet transforms are computed, the first is based on a PS time series, the second is based on the climatic water balance, which is a potential landslide triggering factor. The climatic water balance data is based from a meteorological station located 8 km north of the PS time series analysed in the wavelet analysis. Because the sliding surface of the landslide is several tenth of meters below the land surface, the climatic water balance is used instead of precipitation measurements, which is often used as a potential triggering factor in landslide analysis. In order to investigate on a relationship between (intermittent) periodical signals of the climatic water balance and landslide deformation two continuous wavelet transforms are combined by cross wavelet transform and wavelet coherence.

A requirement for the wavelet analysis is a regular sampling in time across both time series datasets. The PSI time series has a nominal 6-day temporal sampling rate, while the climatic water balance has a daily temporal sampling rate. In the PSI observation time span (1.4.2015 – 30.12.2020, track 139) 350 acquisitions are theoretically possible with a 6-day sampling. As the 6-day sampling was not possible before the start of the Sentinel-1B satellite (25.04.2016) and acquisition gaps exists especially at the beginning of the SAR missions due to the commissioning phase the actual dataset consists of 279 out of the theoretical 350 acquisitions (80%). Thus, at first the PSI time series is filled up by a piecewise linear interpolation between acquisition gaps. Second, the climatic water balance was resampled from daily- to 6-day average. Therefore, the subsequent 6-day climatic water balance average was calculated for each PSI observation date. After these pre-processing steps the continuous wavelet transform of the PSI- and climatic water balance- time series are calculated. Subsequently, the continuous wavelet transform of the PSI- and climatic water balance- time series are the input for the cross wavelet transform and wavelet coherence.

6.5 Results

The results section first reports on the ADA-mapping results used to identify clusters of deforming PS (“ADA-mapping results” section). Subsequently, the time series of these PS is analyzed. Using one exemplary PS deformation time series, the classification results are provided in the “Time series classification results” section and the results of the wavelet analysis are presented in the “Wavelet analysis” section.

6.5.1 ADA-mapping results

Four clusters of moving PSs are classified as ADA in the study area. Two of them are located in the Piesport landslide, one in the Trittenheim landslide (Fig. 6.4) and the third is located in a quarry. The ADA in the Trittenheim landslide consists of 20 PS with a mean deformation rate of 5.65 mm/a in LoS. The maximum PS velocity of this ADA is 18.01 mm/a in LoS. The two ADA at the Piesport landslide consists of 4, resp. 3 PS, with a maximum velocity of 7.09 resp. 5.28 mm/a in LoS. All three ADA’s are characterized by a high Quality Index, indicating a reliable ADA. It has to be noted that several isolated but deforming PS are not classified as ADA (Fig. 6.4).

Concerning the LoS deformation rate, the ADA in the Trittenheim Landslide is deforming faster than the ADA in the Piesport Landslide. Both ADA’s are in large landslide areas, with respect to the average landslide size in the Moselle Valley. Both ADA are located in landslides where soil creeping is present. The creeping soil is part of the sliding mass. The sliding mass is intersected from top to bottom by a road with adjacent stone-walls and metal railings (Fig. 6.3).

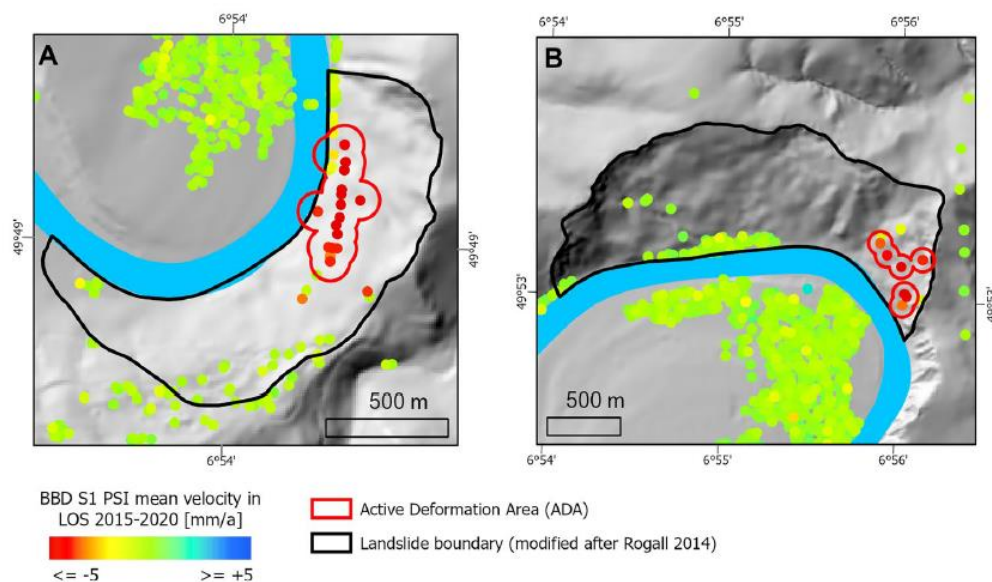


Figure 6.4: Sentinel-1 PSI mean velocity, detected ADA and landslide boundary of the Trittenheim- (A) and Piesport- landslide (B). A shaded relief digital elevation model serves as background

Focusing on the Trittenheim landslide a comparison of the PSI velocity with a geological transect shows that at least three PS velocity clusters can be differentiated (Fig. 6.5). First, a cluster with very low deformation rates slower than -5 mm/a is present at the landslide top. Followed by slightly higher velocities in the rupture area (approximately 250 – 300 m.a.s.l.) with only few PS points. Then a cluster with the highest velocities of up to -18 mm/a located in the middle deformation zone (approximately 200 – 250 m.a.s.l.). Finally, a cluster with low velocities at the landslide toe (150 – 200 m.a.s.l.). In the landslide toe area, a federal street (K86) is present. This is a highly vulnerable element and even low velocities, e.g. -5 mm/a, can be of interest for safety measures.

Regarding the northern ADA located at the Piesport landslide the deformation rates are in general slower with regards to the Trittenheim landslide. At the top of the landslide (approximately 320 – 400 m.a.s.l.) no PS is present. The highest velocities in the rupture area (> 300 m.a.s.l.) are slower than -4 mm/a. In the middle deformation zone velocities reaches -7 mm/a (Fig. 6.6). Below < 250 m.a.s.l. velocities starts to decrease rapidly. All PS deformation time series of both ADA in landslide areas show a linear deformation trend spanning the entire observation time span. The exemplary chosen PS shows a long-term linear trend as well as a periodical signal and abrupt changes of the deformation date (Fig. 6.3). The following sections shows the results based on the exemplary chosen PS time series.

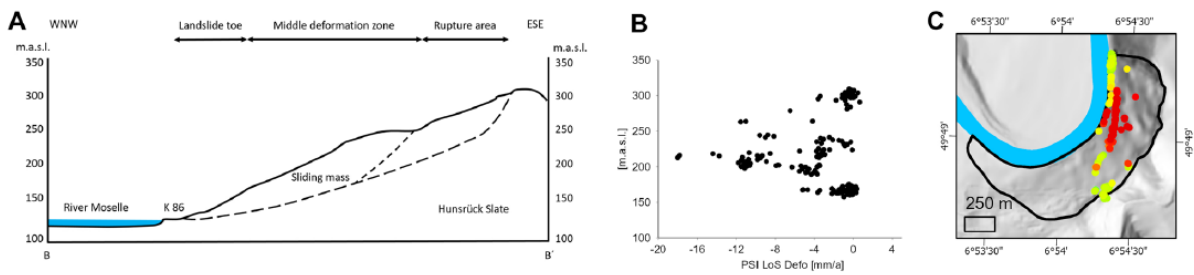


Figure 6.5: Transect of the Trittenheim landslide (A, modified after Rogall 2014), PSI LoS deformation rates vs. elevation (B). The PS velocities shown in B) corresponds to the PS shown in C)

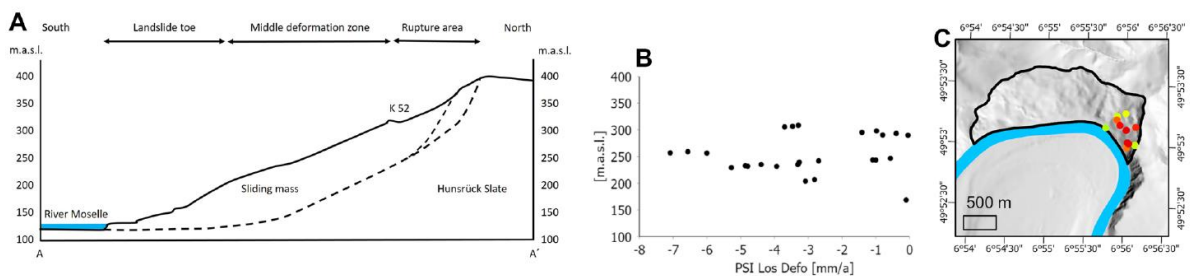


Figure 6.6: Transect of the Piesport landslide (A, modified after Rogall 2014), PSI LoS deformation rates vs. elevation (B). The PS velocities shown in B) corresponds to the PS shown in C)

6.5.2 Time series classification results

In order to detect characteristic patterns of the PS time deformation time series a sequence of statistical tests is performed. Especially PS characterized by an acceleration within the time series are investigated. The motivation is a quantification of a potential time lag between strong rainfall events during times of low potential evapotranspiration and an accelerated deformation. As an example, the deformation time series of a single PS shows an acceleration and is classified as bi-linear with a breakpoint on 11.03.2020 (the location of the PS is shown in Fig. 6.2A by the white arrow). A comparison of the PSI time series with a potential landslide triggering factor, e.g. the climatic water balance shows high positive values in February 2020, approximately one month before the acceleration started. That means, a high precipitation coinciding with a little potential evapotranspiration was present before the detected acceleration. It is hypothesized that the kinematic behaviour of the landslide mass is affected by a higher water content and a lower friction coefficient at the deep seated sliding surface. Fig. 6.7 shows the overall deformation trend covering almost six years of measurements and the detected acceleration. A time-lag of 42 days can be observed between the start of the previous positive climatic water balance period (29.01.2020, red bar in Fig. 6.7) and the PSI breakpoint (11.3.2020, red dot in Fig. 6.7). Until the breakpoint the slope of the linear regression shows a velocity of $v=10.1$ mm/a. After the breakpoint a velocity of $v=14.1$ mm/a is estimated by a linear regression. The corresponding BIC, based on the 5- measurement segments, shows the minimum of 1.3 at the 11.03.2020 and marks the breakpoint of the changepoint regression (Fig. 6.7B).

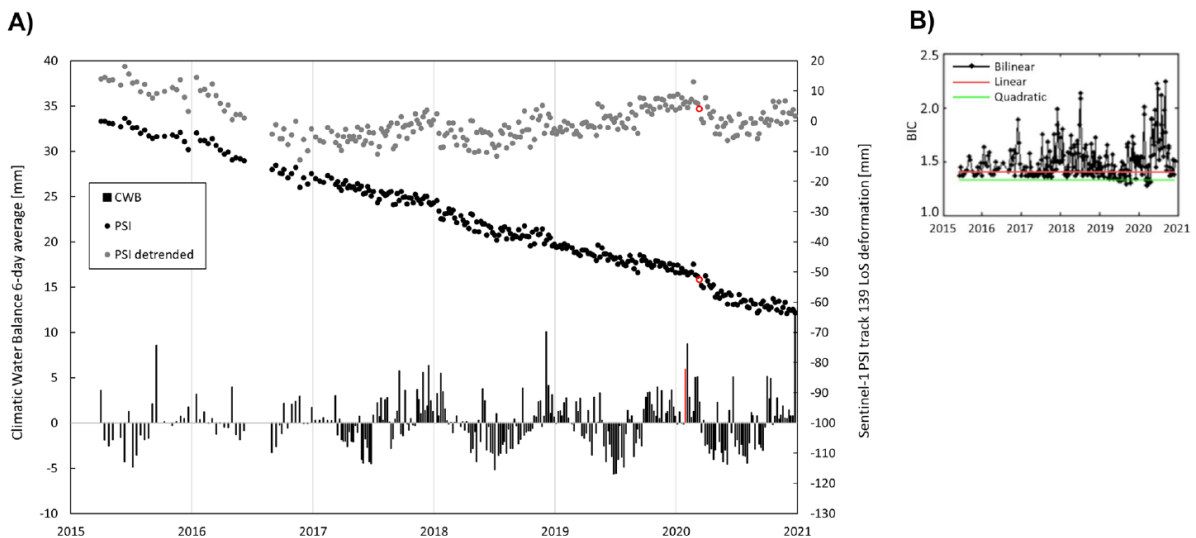


Figure 6.7: Climatic water balance vs. PSI LoS deformation time series (A). The PSI detrended time series is two-times exaggerated for visualisation. The acquisition date where an acceleration is detected is shown as red dot. The earliest date with positive climatic water balance before the acceleration is shown as red bar. Bayesian Information Criterion (BIC) for successive five-measurement segments (black points) (B), for a quadratic regression (green line) and for a linear regression (red line) of the PS deformation time series from track

6.5.3 Wavelet analysis

The same PS time series used in the “Time series classification results” section is used in the wavelet analysis. In order to calculate the wavelet transform the PS deformation time series is detrended and gap filled (Fig. 6.8A, bottom). The continuous wavelet transform shows a periodical signal with a yearly frequency from the beginning of 2018 until the end of 2020 (Fig. 6.8A, top). The power of this signal reaches a value of 16. A periodical signal with a 2-year frequency starting in 2016 is also visible, with slightly higher power values (Fig. 6.8A, top). However, the cone of influence indicates that most of the 2-year signal is not reliable, because the time series is too short. The continuous wavelet transform of the climatic water balance time series shows a strong yearly periodical signal throughout the entire time series (Fig. 6.8B, top). The power values of this signal reaches a value of 30. The yearly periodical signal is clearly visible in the climatic water balance time series plot (Fig. 6.8B, bottom).

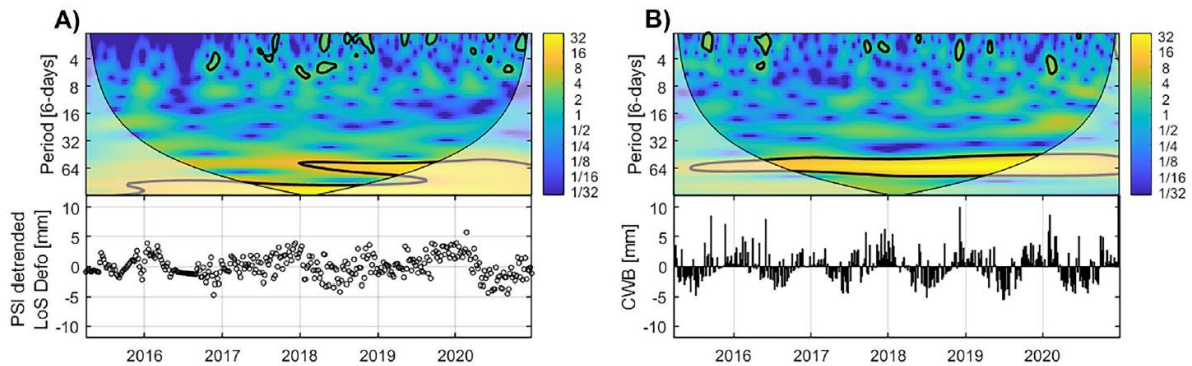


Figure 6.8: continuous wavelet coherence of detrended and gap-filled PSI time series (A) and continuous wavelet coherence of climatic water balance (B). The black line in the continuous wavelet coherence shows the 5% significance level against red noise. The cone of influence, visualized as transparent grey areas shows the time-frequency range which can be affected by edge distortions

The results of the cross wavelet transform show a high correlation between both continuous wavelet transforms. The cross wavelet transform shows a common yearly (and 2-years) periodical signal (Fig. 6.9A). Both signals are mostly in phase which is visualized by the arrows pointing to the right. If the periodical signals were in anti-phase the arrows would point to the left. After 2018 the arrows are pointing slightly downwards, meaning the deformation has a lag to the climatic water balance.

The wavelet coherence shows that a significant correlation starts in 2017 until the end of the time series (Fig. 6.9B). The two-year periodical signal is not significant based on the wavelet coherence. The slight downward pointing of the arrows indicate that there is a time-lag between the time series of ~ 10 days ($\text{time-lag} = 10^\circ \cdot \pi/180^\circ \cdot 365 \text{ days}/(2\pi) = 10.14 \text{ days}$). Three other time-frequency areas with lower periods are also detected by the wavelet coherence, which are not detected by the cross wavelet transform.

6.6 Discussion

The ADA-mapping approach based on track 139 successfully detects all visible deformation clusters (Piesporth-, Trittenheim- landslide, Quarry) after adjusting the thresholds (Tab. 6.6.1). The ADA-mapping result, in the landslide areas, using default- and adjusted- thresholds is shown in Fig. 6.10. Based on the default thresholds only a part of the southern cluster of deforming PS in the Trittenheim landslide is detected (Fig. 6.10A). The northern cluster of deforming PS, located in the Trittenheim landslide, is not detected by default thresholds using track 139. The ADA-mapping results based on track 37 also show that default thresholds underestimated the cluster of deforming PS (Fig. 6.10B). Regarding the Piesport landslide only the ADA-approach using track 139 and adjusted threshold is able to detect the cluster of deforming PS (Fig. 6.10C). The reason for the failure of the ADA-approach based on track 37 is the low spatial PS density (Fig. 6.10D).

Table 6.6.1: Default- and adjusted- thresholds for the ADA-mapping

	Default thresholds	Adjusted thresholds
Isolation distance [m]	40	200
Minimum size of non-isolated clusters	2	2
Factor for stdev filter [σ]	1.5	3.5
Threshold for velocity class 1 [mm/a]	10	16
Clustering radius [m]	26	80
Minimum ADA size	5	3
Values to compute the mean of the deformation [#]	4	4

Due to the low PS density caused by the rural landcover in the landslide areas, relatively large distances between deforming PS's are present. This affects the spatial thresholds used in the ADA-mapping approach. The increased distance threshold detected the visually identified clusters but also detected many other implausible ADA. Thus, the factor for the standard deviation filter threshold is also increased. The threshold for velocity class 1 was increased from 10 mm/a to 16 mm/a, because this is the threshold used to distinguish very slow- from extremely slow- landslides (Cruden and Varnes, 1996). The minimum ADA size was lowered from 5 PS to 3 PS due to the low PS density. However, results show that the thresholds needed an adjustment to be successful and the question of transferability is still open, e.g. how a spatially large PSI dataset with various landcover types and as a consequence various PS densities can be exploited by using fixed thresholds.

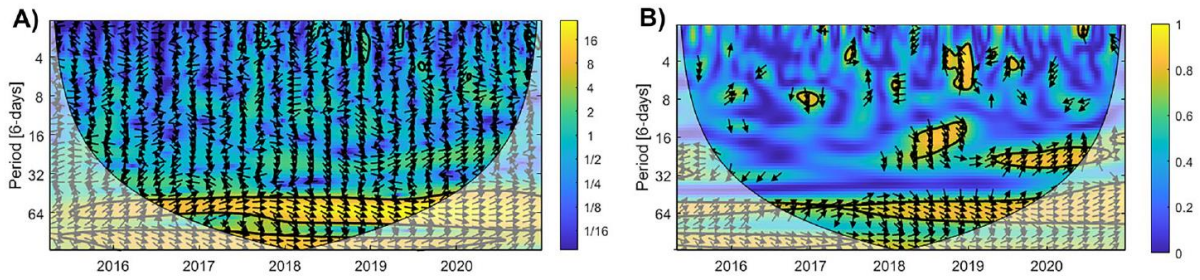


Figure 6.9: Cross wavelet transform of detrended PSI time series and climatic water balance (A) and wavelet coherence of detrended PSI time series and climatic water balance (B)

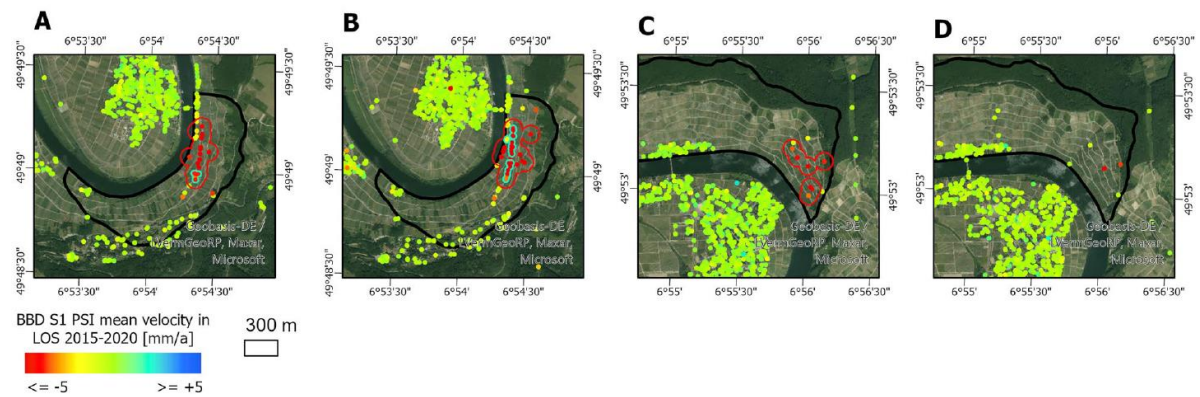


Figure 6.10: ADA-mapping result based on default- and adjusted- thresholds based on track 139 (A, C) and 37 (B, D)

In order to verify results from the time series classification and the wavelet analysis a PS deformation time series from another track is used (track 37). The PS is chosen based on the nearest spatial distance to the PS used from track 139 in the results section. Regarding the estimation of a time-lag between the acceleration start and a potential triggering factor (climatic water balance) the changepoint regression from track 139 indicates a 42-day delay. Using the PS from track 37 the changepoint regression failed in finding a reasonable breakpoint date (e.g. ~begin of 2018 or begin of 2020, Fig. 6.10A). Thus, no reasonable time-lag is calculated by the time series classification approach using track 37. Reasonable breakpoint dates correspond to low BIC values (Fig. 6.10B), however the lowest BIC value lies in October, 6th 2020, where no acceleration is visible in the PS time series (Fig. 6.11A). This raises the question of transferability of this approach regarding breakpoint detection.

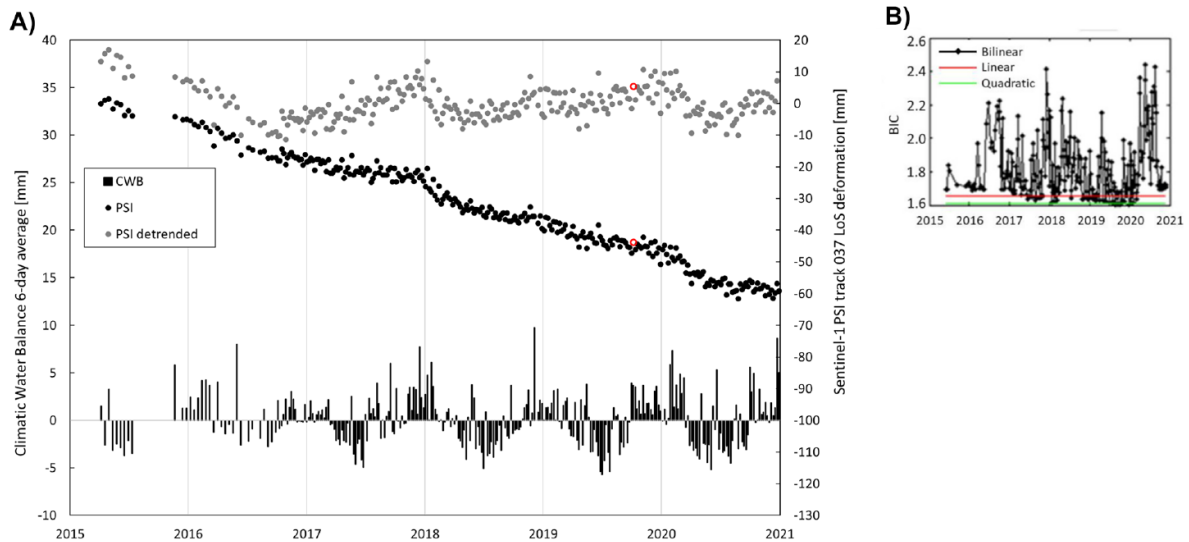


Figure 6.11: Climatic water balance vs. PS deformation time series based on track 37 (A). The PSI detrended time series is two-times exaggerated for visualisation. The detected breakpoint date is shown as red dot. Bayesian Information Criterion (BIC) for successive five-measurement segments (black points) (B), for a quadratic regression (green line) and for a linear regression (red line) of the PS deformation time series from track 37

The continuous wavelet transform from the PS time series from track 37 shows a similar yearly (and 2-yearly) periodical signal as from track 139 (Fig. 6.12). The cross wavelet transform and wavelet coherence of track 37 confirms the correlation between PS deformation and climatic water balance regarding a yearly (and two-yearly) periodical signal (Fig. 6.12C, D). Based on the wavelet coherence the time-lag is 10-days for 2018 - 2019. The wavelet verification indicate a good transferability to another PS time series from another track with a similar time series pattern.

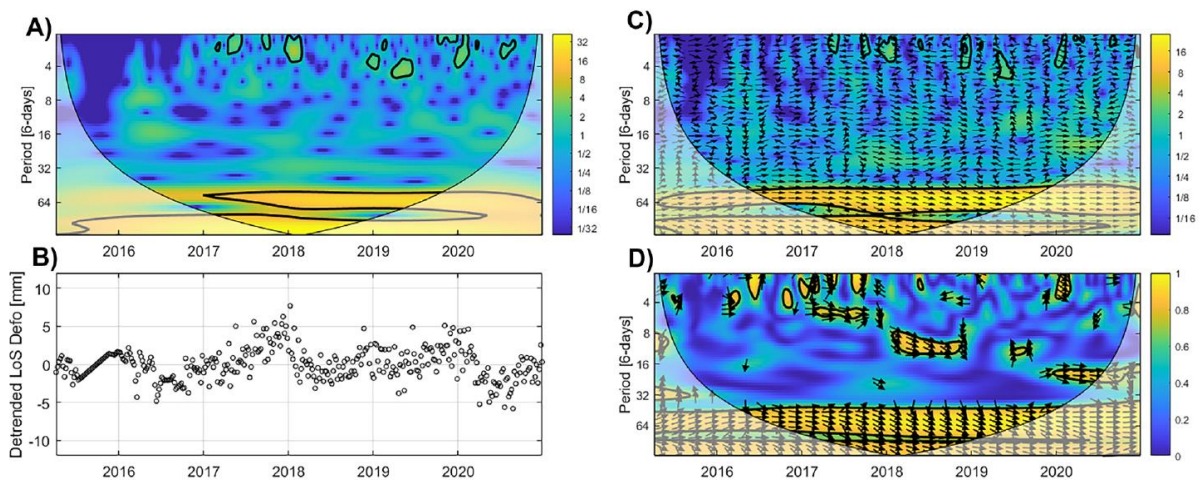


Figure 6.12: Continuous wavelet transform (A) of detrended, gap filled PSI time series of the PS deformation time series from track 37 (B). The black line in the continuous wavelet transform shows the 5% significance level against red noise. The cone of influence, visualized as transparent grey areas shows the time-frequency range, which can be affected by edge

distortions. C) Shows the cross wavelet transform of the detrended, gap filled PSI time series of the PS from track 37 and the climatic water balance shown in Fig. 10B). D) Shows the corresponding wavelet coherence

6.7 Conclusion

The results of the case study show that information regarding groups of deforming PS, accelerations of deformation and intermittent periodical signals can be semi-automatically extracted from a wide area Sentinel-1 PSI dataset from the Ground Motion Service Germany (Kalia et al., 2021). In order to assess the transferability of the three applied post processing techniques (Berti et al., 2013, Barra et al., 2017, Liu et al., 2022) the approaches are tested on a second independent Sentinel-1 PSI dataset from another track which is also processed in the framework of the Ground Motion Service Germany (track 37). Verification results show that only the cluster of deforming PS in the Trittenheim landslide is detected by using track 37. The active deformation area correctly detected by using track 139 is not detected by using track 37. The reason is the low spatial PS density. Just two deforming PS are present in the Piesport landslide from track 37. This is below the minimum threshold of at least three deforming PS to form a cluster within the ADA-mapping approach.

Regarding the detection of a plausible acceleration date, the changepoint regression is successful by using the PS time series from track 139. It failed by using the PS time series from track 37. The estimated time-lag between acceleration and a potential triggering factor (climatic water balance) is 42 days (based on the acceleration date from track 139).

The wavelet analysis successfully quantified a yearly (and 2-years) periodical signal in both exemplarily chosen PS deformation time series from track 139 and 37. Both wavelet coherence results indicate a time-lag of 11 days between the seasonal acceleration and the seasonal signal of the potential triggering factor (climatic water balance) for 2018 and 2019.

To conclude, the ADA-mapping approach is able to highlight reliable deformation areas and can guide the end-users attention. Once these areas are identified, time series analysis can provide further insights regarding correlation and quantification of time-lags with respect to a potential triggering factor.

6.8 Acknowledgement

The European Space Agency (ESA) is acknowledged for providing Sentinel-1 data. The GAF AG and the German Aerospace Center (DLR) is acknowledged for wide-area Sentinel-1 PSI processing as contractor for the German Ground Motion Service. Mr. Ansgar Wehinger from the State Geological Survey of Rhineland-Palatinate is acknowledged for discussion regarding the Sentinel-1 PSI results. The figures contain modified Copernicus Sentinel-1 2015–2020 data. Open Access funding enabled and organized by Projekt DEAL. This work is funded by the Federal Institute for Geosciences and Natural Resources (BGR).

7 Conclusion

In Summary, this thesis proposes a concept for the GMS Germany, and investigates how the resulting nationwide PSI datasets of the GMS Germany can be used in a (semi-) automatic way for landslide applications.

In this thesis, at first, a concept for a GMS Germany based on Sentinel-1 wide-area PSI datasets is proposed (chapter 4). The concept answers the first research question of this thesis: “What are the user requirements for a nationwide Ground Motion Service in Germany?” in two ways. The first way is regarding the deformation processes which are of interest for the users. The result consists of ten deformation processes: e.g. coastal subsidence, landslides, (abandoned) mining (table 4.3.1). The second way is regarding the properties of the A-DInSAR datasets. The consistency of the A-DInSAR datasets with other measurements (e.g. GNSS, leveling) and the reliability of the A-DInSAR datasets were identified as important user requirement (chapter 4.3.). These user requirements leads to the technical requirements, which are the second research question of this thesis: “What are the technical requirements regarding an A-DInSAR for a nationwide Ground Motion Service in Germany?” The technical requirements includes, e.g. a GNSS calibration of the A-DInSAR datasets to provide consistency with other measurements, a validation strategy to provide a high reliability of the A-DInSAR datasets (chapter 4.5.).

Subsequently, the GMS Germany was realized and yearly updates are provided, free and open, through a big data WebGIS application (Kalia et al., 2021). The concept defines the A-DInSAR specifications for the GMS Germany. The GMS Germany started in 2019 with the online dissemination of the first wide-area Sentinel-1 PSI dataset covering entire Germany. In order to assess the accuracy and usability of the datasets several studies were performed by the author and by responsible authorities (State Geological Surveys, Geodetic agencies on federal and state level). Comparison with GNSS-, levelling- and independent A-DInSAR velocities showed an accuracy of $\sigma_{\text{VLOS}} = 2 - 3 \text{ mm a}^{-1}$ (Kalia, 2018, Kalia et al., 2021, Kalia et al., 2022, Kalia, 2022b). The observed level of accuracy is in agreement with other verification studies assessing the accuracy of Sentinel-1 A-DInSAR datasets (Mancini, et al., 2021, Costantini et al., 2022b). Furthermore, the high accuracy together with the nationwide coverage, yearly updated production and free and open dissemination through a WebGIS are important for the improved operational use of A-DInSAR datasets in Germany. However, the use of A-DInSAR datasets is usually done by visual interpretation, which is subjective, time-consuming and error-prone due to outliers.

In order to improve the usability several authors proposed (semi-) automatic A-DInSAR post-processing methods, e.g. to identify active deformation areas (Barra et al., 2017). With the purpose to investigate on these methods, the third research question of this thesis is: “What are the requirements for a semi-automatic mapping of the landslide state of activity, detection of accelerations and seasonality within PS deformation time series?” This question was answered by the second and third paper (chapter 5 and 6). E.g. for a semi-automatic mapping of the landslide state of activity, a visibility and sensitivity of the LoS geometry with respect to the landslide (deformation vector) has to be present (chapter 5.6.) and a certain measurement point density is required to detect clusters of moving PS (fig. 6.10.). To the authors knowledge this is the first time a (semi-) automatic mapping of landslide activity, based on A-DInSAR datasets, is performed in Germany. The proposed clustering method uses the deformation rate of the PS

and their spatial location to detect deformation areas. By using statistically significant deformation areas, instead of performing a visual interpretation, the usability of the A-DInSAR dataset is increased. The regional scale classification resulted in 23 “active, very slow” landslides, 24 “active, extremely slow”, 132 “inactive” landslides, and 204 “not classified” landslides. Verification of the results against a thematic map (landslide hazard indication map), field surveys and GNSS time series showed the plausibility of the results. The large amount of “not classified” landslides represents a major limitation of this approach. There are multiple reasons why a landslide was not classified, e.g. no PS due to the temporal decorrelation, no cluster of moving PS due to low geometrical sensitivity or fast non-linear deformation. However, in 47 landslides the current state of activity was mapped. This is an additional information which can be used to enhance landslide inventories. A similar technique, the so-called ADA-detection, proposed by Barra et al. (2017), was investigated in chapter 6. Results showed that the default parametrization of the ADA-detection were not suited to the rural study area characterized by a low PS density. After adjusting the distance- and noise- thresholds the ADA detection was improved. The strong variability of PS density (dozens of PS km⁻¹ to more than thousand PS km⁻¹) and spatial scales of detected deformation areas (few hundred meters to several km) makes a proper parametrization of the ADA-detection approach challenging for a nationwide dataset.

Another important landslide application based on A-DInSAR datasets is the understanding of the involved kinematic processes with respect to potential triggering factors, e.g. precipitation. In order to investigate how temporal deformation patterns of the PSI time series of the GMS Germany can be detected in a semi-automatic way, a case study is performed (chapter 6). The case study focuses on temporal relationships between certain deformation patterns (acceleration and periodical signal) and a potential landslide triggering factor (climatic water balance as a proxy for soil water saturation). Therefore, the time lag between a high value of climatic water balance and an automatically detected acceleration is calculated. The approach used to detect the start of the acceleration is based on the BIC. The approach is verified by a second independent Sentinel-1 PSI dataset from the GMS Germany. The result based on the second PSI dataset showed that the BIC approach was not successful in detecting the start of the acceleration. An increase of the temporal window used for the calculation of the BIC does not show an improvement of the results. Thus, the most plausible reason, why the BIC approach failed, is the noise level of the deformation time series compared to the magnitude acceleration signal. The second temporal relationship, investigated in chapter 6, is focusing on a time lag between an intermittent periodical deformation signal and an intermittent periodical signal of the climatic water balance. The approach is based on wavelet analysis and is verified by a second independent Sentinel-1 PSI dataset from the GMS Germany. Results show, that the wavelet approach was able to detect a plausible time-lag, of 11 days, in both PSI datasets.

8 Outlook

Based on the experiences gathered during this thesis, the following research directions are proposed for an increased usability of regularly updated A-DInSAR datasets produced by operational GMS.

Improving wide-area S-1 A-DInSAR processing: Nationwide- or even Continental- A-DInSAR products are a milestone in the operational use of A-DInSAR. However, limitations are present, e.g. relatively low measurement point density in rural areas. In order to increase the measurement point density GMS could use PS/DS processing instead of PSI processing. Albeit the high potential of a PS/DS dataset, the precision of a nationwide PS/DS dataset should be investigated, e.g. because of the higher phase noise of the DS. In principle, this could be done by an intercomparison of independent PS/DS datasets or by comparison with terrestrial measurements. Other limitations are i) the very low sensitivity regarding deformations in the North-South direction and ii) phase unwrapping errors in areas with strong non-linear deformations. The sensitivity in North-South direction could be improved by e.g. an increased LoS diversity (López-Dekker et al., 2021).

Improving the GMS WebGIS: Currently, A-DInSAR products are provided as velocity maps and deformation time series. Although, the deformation can be non-linear in time, e.g. acceleration, deceleration and periodical signal, the mean velocity of the entire processed timespan is visualized as a map. This could be improved by an adjustable timespan and subsequent calculation and visualization of the mean velocity, for user specific timespans.

Improving (semi-) automatic information extraction: Instead of using a-priori defined noise- and distance- thresholds for the detection of active deformation areas, machine learning techniques could be used. E.g. DBSCAN or self-organizing maps could be used to detect spatio-temporal clusters. These classification techniques could be used to detect nearby groups of measurement points with similar deformation time series.

9 Bibliography

- Abdikan, S., Arikan, M., Sanli, F. B., Cakir, Z., 2013. Monitoring of coal mining subsidence in peri-urban area of Zonguldak city (NW Turkey) with persistent scatterer interferometry using ALOS-PALSAR. *Environ. Earth Sci.* 71, 4081–4089.
- Adam, N., Kampes, B., Eineder, M., 2004. Development of a scientific permanent scatterer system: Modifications for mixed ERS/ENVISAT time series. In *Proceedings of the Envisat Symposium 2004*, Salzburg, Austria, 6–10 September 2004, ESA: Paris, France.
- Adam, N., Kampes, B., Eineder, M., 2005. Development of a scientific permanent scatterer system: Modifications for mixed ERS/ENVISAT time series. In *Envisat & ERS Symposium (Vol. 572)*.
- Adam, N., Kampes, B. M., 2008. Service Validation Protocol C5 V3.5. Protocol from the GMES TerraFirma project. Available at (accessed on 15.06.2016): http://www.terrafirma.eu.com/Documents/dossiers/stage2/C5_Servicevalidationprotocol_V3.4_Aug08.pdf.
- Adam, N., Parizzi, A., Eineder, M., Crosetto, M., 2009. Practical persistent scatterer processing validation in the course of the TerraFirma project. *J. Appl. Geophys.* 69, 59–65.
- Adam, N., Gonzalez, F. R., Parizzi, A., Liebhart, W., 2011a. Wide area persistent scatterer interferometry: algorithms and examples. *FRINGE 2011*, pp. 1–5 Frascati, Italy: ESA Communications, ESTEC, Noordwijk, The Netherlands.
- Adam, N., Rodriguez, F.G., Parizzi, A., Liebhart, W., 2011b. Wide area persistent scatterer interferometry. *International Geoscience and Remote Sensing Symposium (IGARSS)*, pp. 1481–1484.
- Adam, N., Gonzalez, F.-R., Parizzi, A., Brcic, A., 2013. Wide area Persistent Scatterer Interferometry: Current developments, algorithms and examples. *IEEE International Geoscience and Remote Sensing Symposium - IGARSS*, Melbourne, VIC, pp. 1857-1860.
- Adam, N., 2018. PSI-Prozessierung von Sentinel-1 Daten für den Bodenbewegungsdienst Deutschland: Erweiterungen des Integrierten Wide-Area Prozessors (IWAP) des DLR und Eigenschaften der erzeugten Produkte, BBD Workshop, Hannover, Germany.
- Adam, N., 2018. The development of a high precision troposphere effect mitigation processor for SAR interferometry. In *Proceedings of the IGARSS 2018*, Valencia, Spain, 22–27 July 2018, pp. 1–4.
- Adam, N., 2019. Methodology of a Troposphere Effect Mitigation Processor for SAR Interferometry. *IEEE Journal of Selected Topics in Applied Earth Observations and Remote Sensing*, vol. 12, no. 12, pp. 5334-5344.
- Agram, P. S., Simons, M., 2015. A noise model for InSAR time series. *J. Geophys. Res. Solid Earth* 120 (4), 2752–2771.
- Agudo, M., Crosetto, M., Raucoules, D., Bourguine, B., Closset, L., Bremmer, C., Veldkamp, H., Tragheim, D., Bateson, L., 2006. PSIC4 — Defining the Methods for PSI Validation and Intercomparison. BRGM/RP-55636-FR, BRGM 2007, available at (accessed on:

29.06.2016):. http://earth.esa.int/psic4/PSIC4_Defining_Methods-PSI_Validation_and_Intercomparison_rprt_Task6.pdf.

- Ansari, H., De Zan, F., Adam, N., Goel, K., Bamler, R., 2016. Sequential estimator for distributed scatterer interferometry. 2016 IEEE International Geoscience and Remote Sensing Symposium (IGARSS), pp. 6859–6862.
- Ansari, H., Rußwurm, M., Ali, M., Montazeri, S., Parizzi, A., Zhu, X. X., 2021. InSAR Displacement Time Series Mining: A Machine Learning Approach. IEEE International Geoscience and Remote Sensing Symposium IGARSS, pp. 3301–3304, doi: 10.1109/IGARSS47720.2021.9553465.
- Anselin, L., 1995. Local indicators of spatial association—Lisa. *Geogr. Anal.*, 27, 93–115.
- Barra, A., Solari, L., Béjar-Pizarro, M., Monserrat, O. et al., 2017. A Methodology to Detect and Update Active Deformation Areas Based on Sentinel-1 SAR Images, *Remote Sensing*, Vol. 9, No. 10.
- Behre, K.-E., 2004. Coastal development, sea-level change and settlement history during the later Holocene in the Clay District of Lower Saxony (Niedersachsen), northern Germany. *Quat. Int.* 112, 37–53.
- Bekaert, D., Hooper, A., Wright, T., 2015. Reassessing the 2006 Guerrero slow-slip event, Mexico: implications for large earthquakes in the Guerrero Gap. *J. Geophys. Res. Solid Earth* 120, 1357–1375.
- Bekaert, D. P. S., Hooper, A., Wright, T. J., 2015b. A spatially variable power law tropospheric correction technique for InSAR data. *J. Geophys. Res. Solid Earth*, 120: 1345–1356. doi: 10.1002/2014JB011558.
- Berardino, P., Fornaro, G., Lanari, R., Sansosti, E., 2002. A new algorithm for surface deformation monitoring based on small baseline differential SAR interferograms. *Geoscience and Remote Sensing, IEEE Transactions on* 40, 2375–2383.
- Berti, M., Corsini, A., Franceschini, S., Iannacone, J. P., 2013. Automated classification of persistent scatterers interferometry time-series. *Nat. Hazards Earth Syst. Sci. Discuss.*, 1, 207–246.
- Bianchini, S., Cigna, F., Righini, G., Proietti, C., Casagli, N., 2012. Landslide hotspot mapping by means of persistent scatterer interferometry. *Environ. Earth Sci.*, 67, 1155–1172.
- Bianchini, S., Herrera, G., Mateos, R., Notti, D., Garcia, I., Mora, O., Moretti, S., 2013. Landslide activity maps generation by means of persistent scatterer interferometry. *Remote Sens.*, 5, 6198–6222.
- Bianchini, S., Solari, L., Casagli, N., 2017. A gis-based procedure for landslide intensity evaluation and specific risk analysis supported by persistent scatterers interferometry (PSI). *Remote Sens.*, 9, 1093.
- BKG, 2018. Digitales Geländemodell Gitterweite 10 m, dgm10. Product description available online: <http://www.geodatenzentrum.de/docpdf/dgm10.pdf> (accessed on 16 November 2018).
- Brandes, C., Steffen, H., Steffen, R., Wu, P., 2015. Intraplate seismicity in northern Central Europe is induced by the last glaciation. *Geology* 43, 611–614.

- Brockmeyer, M., 2015. Auswertung SAPOS Referenzstationen Niedersachsen. Pers. communication.
- Brockmeyer, M., 2021. SAPOS GNSS time series processing, Hannover, 15.4.2021, unpublished.
- Calò, F., Ardizzone, F., Castaldo, R., Lollino, P., Tizzani, P., Guzzetti, F., Lanari, R., Angeli, M.- G., Pontoni, F., Manunta, M., 2014. Enhanced landslide investigations through advanced DInSAR techniques: the Ivancich case study, Assisi, Italy. *Remote Sens. Environ.* 142, 69–82.
- Capes, R., 2012. PanGeo: enabling access to geological information in support of GMES. EAGE/GRSG Remote Sensing Workshop. <http://dx.doi.org/10.3997/2214-4609.20143281>.
- Carlà, T., Intrieri, E., Raspini, F. et al., 2019. Perspectives on the prediction of catastrophic slope failures from satellite InSAR. *Sci Rep* 9, 14137, <https://doi.org/10.1038/s41598-019-50792-y>.
- Casagli, N., Cigna, F., Bianchini, S., Hölbling, D., Füreder, P., Righini, G., Del Conte, S., Friedl, B., Schneiderbauer, S., Iasio, C. et al., 2016. Landslide mapping and monitoring by using radar and optical remote sensing: Examples from the EC-FP7 project safer. *Remote Sens. Appl. Soc. Environ.*, 4, 92–108.
- Cascini, L., Fornaro, G., Peduto, D., 2010. Advanced low- and full-resolution DInSAR map generation for slow-moving landslide analysis at different scales. *Eng. Geol.*, 112, 29–42.
- Casu, F., Elefante, S., Imperatore, P., Zinno, I., Manunta, M., De Luca, C., Lanari, R., 2014. SBAS-DInSAR parallel processing for deformation time series computation. *IEEE Journal of Selected Topics in Applied Earth Observations and Remote Sensing* 7 (8): 3285–3296. <http://dx.doi.org/10.1109/JSTARS.2014.2322671>.
- Chang, L., Dollevoet, R. P. B. J., Hanssen, R. F., 2016. Nationwide Railway Monitoring Using Satellite SAR Interferometry. *IEEE Journal of Selected Topics in Applied Earth Observations and Remote Sensing*, pp. 1–9. <http://dx.doi.org/10.1109/JSTARS.2016.2584783>.
- Chang, L., Hanssen, R.F., 2014. Detection of cavity migration and sinkhole risk using radar interferometric time series. *Remote Sens. Environ.* 147, 56–64.
- Chaussard, E., Bürgmann, R., Shirzaei, M., Fielding, E. J., Baker, B., 2014. Predictability of hydraulic head changes and characterization of aquifer-system and fault properties from InSAR-derived ground deformation. *J. Geophys. Res. Solid Earth*, 119, 6572–6590, doi:10.1002/2014JB011266.
- Chaussard, E., Amelung, F., Abidin, H., Hong, S.-H., 2013. Sinking cities in Indonesia: ALOS PALSAR detects rapid subsidence due to groundwater and gas extraction. *Remote Sens. Environ.* 128, 150–161.
- Cigna, F., Bianchini, S., Casagli, N., 2013. How to assess landslide activity and intensity with persistent scatterer interferometry (PSI): The PSI-based matrix approach. *Landslides*, 10, 267–283.
- Cohen-Waeber, J., Bürgmann, R., Chaussard, E., Giannico, C., Ferretti, A., 2018. Spatiotemporal patterns of precipitation-modulated landslide deformation from independent component analysis of InSAR time series. *Geophysical Research Letters*, 45, 1878–1887, <https://doi.org/10.1002/2017GL075950>.

- Cohen-Waeber, J., Bürgmann, R., Chaussard, E., Giannico, C., Ferretti, A., 2018. Spatiotemporal patterns of precipitation-modulated landslide deformation from independent component analysis of InSAR time series. *Geophysical Research Letters*, 45, 1878–1887, <https://doi.org/10.1002/2017GL075950>.
- Confuorto, P., Medici, C., Bianchini, S., Del Soldato, M., Rosi, A., Segoni, S., Casagli, N., 2022. Machine Learning for Defining the Probability of Sentinel-1 Based Deformation Trend Changes Occurrence. *Remote Sensing*. 14. 1748. 10.3390/rs14071748.
- Costantini, M., 1998. A novel phase unwrapping method based on network programming. *IEEE Transactions on Geoscience and Remote Sensing*, vol. 36, no. 3, pp. 813-821, May 1998, doi: 10.1109/36.673674.
- Costantini, M., Minati, F., Trillo, F. et al., 2022. EGMS: Europe-Wide Ground Motion Monitoring Based on Full Resolution InSAR Processing of all Sentinel-1 Acquisitions. In: *International Geoscience and Remote Sensing Symposium (IGARSS)*. IEEE. IGARSS 2022, 17.-22. Juli 2022, Kuala Lumpur, Malaysia.
- Costantini, M., Minati, F., Trillo, F., Ferretti, A., Passera, E., Rucci, A., Dehls, J., Larsen, Y., Marinkovic, P., Eineder, M., Brcic, R., Siegmund, R., Kotzerke, P., Kenyeres, A., Proietti, S., Solari, L., Andersen, H. S., 2022b. European Ground Motion Service (EGMS): General Description, Product Quality, and Examples. *Living Planet Symposium 2022*, 23.-27. Mai 2022, Bonn, Germany.
- Covello, F., Battazza, F., Coletta, A., Lopinto, E., Fiorentino, C., Pietranera, L., Valentini, G., Zoffoli, S., 2010. COSMO-SkyMed an existing opportunity for observing the Earth. *J. Geodyn.* 49, 171–180.
- Crosetto, M., Solari, L., Mróz, M., Balasis-Levinsen, J., Casagli, N., Frei, M., Oyen, A., Moldestad, D. A., Bateson, L., Guerrieri, L., Comerci, V., Andersen, H. S., 2020. The Evolution of Wide-Area DInSAR: From Regional and National Services to the European Ground Motion Service. *Remote Sens.* 2020, 12, 2043. <https://doi.org/10.3390/rs12122043>.
- Crosetto, M., Monserrat, O., Cuevas-González, M., Devanthéry, N., Crippa, B., 2016. Persistent scatterer interferometry: A review. *ISPRS J. Photogramm. and Remote Sens.*, 115, 78–89.
- Cruden, D. M., 1991. A simple definition of a landslide. *Bull. Int. Assoc. Eng. Geol. Bull. l'Assoc. Int. Géol. l'Ing.*, 43, 27–29.
- Cruden, D. M., 1995. A suggested method for describing the rate of movement of a landslide. *Bull. Int. Assoc. Eng. Geol. Bull. l'Assoc. Int. Géol. l'Ing.*, 52, 75–78.
- Cruden, D. M. and Varnes, D. J., 1996. Landslide types and processes. In *Landslides Investigation and Mitigation*, Turner AK and Schuster RL, Eds., Special Report 247, Transportation Research Board, US National Research Council: Washington, DC, USA, pp. 36–75
- Davide, F., Nicola, C., Casu, F., Confuorto, P., De Luca, C., Del Soldato, M., Lanari, R., Manunta, M., Manzo, M., Raspini, F., 2022. Automated classification of A-DInSAR-based ground deformation by using random forest, *GIScience & Remote Sensing*, 59:1, 1749-1766, DOI: 10.1080/15481603.2022.2134561.
- De Zan, F., Monti Guarnieri, A., 2006. TOPSAR: Terrain Observation by Progressive Scans. *IEEE Trans. Geosci. Remote Sens.* 44, 2352–2360.

- Dehls, J., 2017. InSAR.No: A national insar deformation mapping service in Norway. In Proceedings of the Fringe 2017—10th International Workshop on Advances in the Science and Applications of SAR Interferometry and Sentinel-1 InSAR, Helsinki, Finland, 5–9 June 2017.
- Del Soldato, M., Solari, L., Novellino, A., Monserrat, O., Raspini, F., 2021. A New Set of Tools for the Generation of InSAR Visibility Maps over Wide Areas. *Geosciences*, 11, 229. <https://doi.org/10.3390/geosciences11060229>.
- Del Soldato, M., Confuorto, P., Bianchini, S., Sbarra, P., Casagli, N., 2021b. Review of works combining GNSS and InSAR in Europe. *Remote Sensing*, 13(9), 1684.
- Del Ventisette, C., Righini, G., Moretti, S., Casagli, N., 2014. Multitemporal landslides inventory map updating using spaceborne SAR analysis. *Int. J. Appl. Earth Obs. Geoinf.* 30, 238–246.
- DLR, 2016. Nationales Forum für Fernerkundung und Copernicus. Available at (accessed on: 29.06.2016). <http://www.d-copernicus.de/veranstaltungen-uebersicht>.
- EC, 2013. Proposal for a Regulation of the European Parliament and of the Council Establishing the Copernicus Programme and Repealing Regulation (EU) No 911/2010.
- Egglesmann, R., 1984. Subsidence of peatland caused by drainage, evaporation and oxidation. Proceedings of the Third International Symposium on Land Subsidence. IAHS Publication, Venice, Italy, pp. 497–505.
- Emardson, T. R., Simons, M., Webb, F. H., 2003. Neutral atmospheric delay in interferometric synthetic aperture radar applications: statistical description and mitigation. *J. Geophys. Res. Solid Earth* 108 (B5):2231. <http://dx.doi.org/10.1029/2002JB001781>.
- Engesser, W., Ruch, C., Wirsing, G., 2010. Geologische Untersuchungen von Baugrundhebungen im Bereich des Erdwärmesondenfeldes beim Rathaus in der historischen Altstadt von Staufen i. Br. Sachstandsbericht, Az.: 94-4763//10-563, 459p., Landesamt für Geologie, Rohstoffe und Bergbau (LGRB), Available at (accessed on 1.10.2022): <https://lgrbwissen.lgrb-bw.de/sites/default/files/public/lgrbwissen/dokumente/lgrb-dokumente-sachstandsbericht-2010-ews-schadensfall-staufen-mit-anlagen.pdf> (in German).
- ESA, 2015. Sentinel-1 Mission Status Reports 59. Available at (accessed on: 15.06.2016): https://sentinel.esa.int/documents/247904/1752934/Sentinel-1-Mission_Status_Report_59-Period_9-15_June_2015.pdf.
- ESA, 2016. Sentinel-1 Mission Status Report 110. Available at (accessed on: 15.06.2016): https://sentinel.esa.int/documents/247904/2214416/Sentinel-1-Mission_Status_Report_110-Period_7-13_June_2016.
- ESA, 2017. Sentinel-1 SAR, Data Formats, Product Slices. Available at (accessed on: 11.04.2017): <https://sentinel.esa.int/web/sentinel/user-guides/sentinel-1-sar/data-formats/product-slices>.
- Farina, P., Colombo, D., Fumagalli, A., Marks, F., Moretti, S., 2006. Permanent scatterers for landslide investigations: outcomes from the ESA-SLAM project. *Eng. Geol.*, 88, 200–217.
- Fattahi, H., Amelung, F., 2014. InSAR uncertainty due to orbital errors. *Geophys. J. Int.* 199 (1), 549–560.

- Fattahi, H., Amelung, F., 2015. InSAR bias and uncertainty due to the systematic and stochastic tropospheric delay. *J. Geophys. Res. Solid Earth* 120 (12), 8758–8773.
- Ferretti, A., Prati, C., Rocca, F., 1999. Permanent scatterers in SAR interferometry. *International Geoscience and Remote Sensing Symposium*, Hamburg, Germany, 28.6.-2.7.1999, pp. 1-3.
- Ferretti, A., Prati, C., Rocca, F., 2000. Nonlinear subsidence rate estimation using permanent scatterers in differential SAR interferometry. *IEEE Trans. Geosci. Remote Sens.* 38, 2202–2212.
- Ferretti, A., Prati, C., Rocca, F., 2001. Permanent scatterers in SAR interferometry. *IEEE Trans. Geosci. Remote Sens.* 39, 8–20.
- Ferretti, A., Monti-Guarnieri A., Prati, C., Rocca, F., Massonnet, D., 2007. *InSAR Principles: Guidelines for SAR Interferometry Processing and Interpretation*. ESA Publications, TM-19. ISBN 92-9092-233-8. Available at: http://www.esa.int/About_Us/ESA_Publications
- Ferretti, A., Fumagalli, A., Novali, F., Prati, C., Rocca, F., Rucci, A., 2011. A new algorithm for processing interferometric data-stacks: Squeesar. *IEEE Trans. Geosci. Remote Sens.*, 49, 3460–3470.
- Ferretti, A., 2014. *Satellite InSAR Data: Reservoir Monitoring From Space*. EAGE Publications bv, Netherlands ISBN: 978-90-73834-71-2.
- Ferretti, A., Passera, E., Capes, R., 2021. End-to-end implementation and operation of the European Ground Motion Service (EGMS) - Algorithm Theoretical Basis Document. 81p. EGMS-D3-ALG-SC1-2.0-006. Available at (accessed on. 1.10.2022): <https://land.copernicus.eu/user-corner/technical-library/egms-algorithm-theoretical-basis-document>
- Fokker, P. A., Visser, K., Peters, E., Kunakbayeva, G., Muntendam-Bos, A.G., 2012. Inversion of surface subsidence data to quantify reservoir compartmentalization: a field study. *J. Pet. Sci. Eng.* 96-97, 10–21.
- Froude, M. J., Petley, D. N., 2018. Global fatal landslide occurrence from 2004 to 2016. *Nat. Hazards Earth Syst. Sci.*, 18, 2161–2181.
- Fuhrmann, T., Caro Cuenca, M., Knöpfler, A., van Leijen, F.J., Mayer, M., Westerhaus, M., Hanssen, R.F., Heck, B., 2015. Estimation of small surface displacements in the Upper Rhine Graben area from a combined analysis of PS-InSAR, levelling and GNSS data. *Geophys. J. Int.* 203, 614–631.
- Galve, J.P., Castañeda, C., Gutiérrez, F., Herrera, G., 2015. Assessing sinkhole activity in the Ebro Valley mantled evaporite karst using advanced DInSAR. *Geomorphology* 229, 30–44.
- Gariano, S. L., Guzzetti, F., 2016. Landslides in a changing climate. *Earth-Sci. Rev.*, 162, 227–252.
- Gatelli, F., Monti Guarnieri, A., Parizzi, F., Pasquali, P., Prati, C., Rocca, F., 1994. The wave-number shift in SAR interferometry. *IEEE Trans. Geosci. Remote Sens.* 32, 855–865.
- Gernhardt, S., Adam, N., Eineder, M., Bamler, R., 2009, TerraSAR-X High Resolution Spotlight Persistent Scatterer Interferometry. In: *Proceedings of Fringe 2009*, p. 1-5. Fringe 2009, 30. Nov. - 04. Dec., Frascati, Italy.

- Goel, K., Adam, N., Shau, R., Rodriguez Gonzalez, F., 2016. Improving the reference network in wide-area Persistent Scatterer Interferometry for non-urban areas. *IEEE International Geoscience and Remote Sensing Symposium (IGARSS)*, Beijing, pp. 1448-1451, <https://doi.org/10.1109/IGARSS.2016.7729370>.
- Goel, K., Adam, N., 2015a. Absolute GPS Calibration of Niedersachsen PSI Deformation Estimates, personal communication.
- Goel, K., Adam, N., 2015b. Mosaiking of Niedersachsen PSI Estimates, personal communication.
- Goel, K., Adam, N., Shau, R., Rodriguez Gonzalez, F., 2016. Improving the reference network in wide-area Persistent Scatterer Interferometry for non-urban areas, *IEEE International Geoscience and Remote Sensing Symposium (IGARSS)*, Beijing, 10–15 July 2016, pp. 1448-1451, <https://doi.org/10.1109/IGARSS.2016.7729370>.
- Grinsted, A., Moore, J. C., Jevrejeva, S., 2004. Application of the cross wavelet transform and wavelet coherence to geophysical time series. *Nonlin. Processes Geophys.*, 11, 561–566, <https://doi.org/10.5194/npg-11-561-2004>.
- Gruijters, S., van der Krogt, R., 2013. TerraFirma and SubCoast: using satellite data for flood related issues and ground subsidence. *EGU General Assembly Conference Abstracts*. 15, pp. EGU2013–EGU9133.
- Guéguen, Y., Deffontaines, B., Fruneau, B., Al Heib, M., de Michele, M., Raucoules, D., Guise, Y., Planchenault, J., 2009. Monitoring residual mining subsidence of Nord/Pas-de-Calais coal basin from differential and Persistent Scatterer Interferometry (Northern France). *J. Appl. Geophys.* 69, 24–34.
- Guzzetti, F., Mondini, A.C., Cardinali, M., Fiorucci, F., Santangelo, M., Chang, K.-T., 2012. Landslide inventory maps: New tools for an old problem. *Earth-Sci. Rev.*, 112, 42–66.
- Hanssen, R., 2001. *Radar Interferometry Data Interpretation and Error Analysis*. Kluwer Academic Publishers, <https://doi.org/10.1007/0-306-47633-9>.
- Haghshenas Haghghi, M. and Motagh, M. 2016. Assessment of ground surface displacement in Taihape landslide, New Zealand, with C- and X-band SAR interferometry, *New Zealand Journal of Geology and Geophysics*, 59:1, 136-146, DOI: 10.1080/00288306.2015.1127824.
- Herrera, G., Gutiérrez, F., García-Davalillo, J.C., Guerrero, J., Notti, D., Galve, J.P., Fernández-Merodo, J.A., Cooksley, G., 2013. Multi-sensor advanced DInSAR monitoring of very slow landslides: The Tena Valley case study (Central Spanish Pyrenees). *Remote Sens. Environ.*, 128, 31–43.
- Herrera, G., Mateos, R.M., García-Davalillo, J.C., Grandjean, G., Poyiadji, E., Maftei, R., Filipciuc, T.-C., Jemec Auflič, M., Jež, J., Podolszki, L., et al., 2018. Landslide databases in the Geological Surveys of Europe. *Landslides*, 15, 359–379.
- Hooper, A., 2008. A multi-temporal InSAR method incorporating both persistent scatterer and small baseline approaches. *Geophys. Res. Lett.* 35, L16302. <http://dx.doi.org/10.1029/2008GL034654>.
- IKÜS, 2008. Abschlussbericht IKÜS-Projekt, Aufbau eines integrierten Höhenüberwachungssystems in Küstenregionen durch Kombination höhenrelevanter Sensorik. Project report available at

(accessed on 29.06.2016):. <https://tu-dresden.de/bu/umwelt/geo/gi/gg/ressourcen/dateien/veroeffentlichungen/BMBF03KIS055-58.pdf?lang=de>.

- Jahn, C.H., 2015. Aktuelle Entwicklungen im geodätischen Raumbezug Deutschlands. FuB Flächenmanagement und Bodenordnung. 77 pp. 201–208.
- Jahn, C. H., Rubach, J., Eisner, C., Schenk, A., Wagenführ, P., Dick, H.G., Brünner, A., 2011. The SAPOS® — quality management of the working group of the surveying administrations of the states of the Federal Republic of Germany. ZFV - Zeitschrift für Geodäsie, Geoinformation und Landmanagement 136, 127–137.
- Kalia, A. C., Frei, M., Lege, T., 2014. Preparation of a national Copernicus service for detection and monitoring of land subsidence and mass movements in the context of remote sensing assisted hazard mitigation. SPIE Remote Sensing Conference, Amsterdam, Proc. SPIE 9245, Earth Resources and Environmental Remote Sensing/GIS Applications V:pp. 924506–924508 <http://dx.doi.org/10.1117/12.2067268>.
- Kalia, A. C., Frei, M., Lege, T., 2016. A Copernicus downstream service for surface displacement monitoring in Germany. EGU General Assembly Conference Abstracts 2016. 18, pp. EGU2016–EG13957.
- Kalia, A. C, Frei, M, Lege, T., 2017. A copernicus downstream-service for the nationwide monitoring of surface displacements in Germany. Remote Sens. Environ., 202, pp. 234–249.
- Kalia, A. C., 2018. Classification of Landslide Activity on a Regional Scale Using Persistent Scatterer Interferometry at the Moselle Valley (Germany). Remote Sens., 10, 1880, <https://doi.org/10.3390/rs10121880>
- Kalia, A. C., Frei, M., Lege, T., 2021. BodenBewegungsdienst Deutschland (BBD): Konzept, Umsetzung und Service-Plattform. Zeitschrift für Geodäsie, Geoinformation und Landmanagement, 4/2021, DOI: 10.12902/zfv-0365-2021.
- Kalia, A. C., 2022. Nutzungshinweise BBD, version 3. (in German) https://www.bgr.bund.de/DE/Themen/GG_Fernerkundung/Downloads/Nutzungshinweise-BBD_PSI-Daten.pdf?__blob=publicationFile&v=2 (accessed on: 12.04.2022)
- Kalia, A. C, Frei, M., Lege, T., 2022b. Updated nationwide surface deformation datasets of the Ground Motion Service Germany. ESA Living Planet Symposium 2022, Bonn, Germany, https://express.converia.de/frontend/index.php?page_id=22633&additions_conferenceschedule_action=detail&additions_conferenceschedule_controller=paperList&pid=64529&hash=1be86d6d8b6743e0260f27414e8f3f3ce3040644a68e7da53a6fa64da8e3f3cd
- Kampes, B. M., 2006. Radar Interferometry - Persistent Scatterer Technique. Remote Sensing and Digital Image Processing 12. Springer, Netherlands. <http://dx.doi.org/10.1007/978-1-4020-4723-7>.
- Kampes, B. M., Adam, N., 2003. Velocity field retrieval from long term coherent points in radar interferometric stacks. Geoscience and Remote Sensing Symposium, IGARSS 2003 Conference Proceedings. 942, pp. 941–943.
- Ketelaar, V.B.H.G., 2009. Satellite Radar Interferometry—Subsidence Monitoring Techniques, 1st ed., Springer: Berlin, Germany, p. 244, <http://dx.doi.org/10.1007/978-1-4020-9428-6>.

- Krieger, G., Fiedler, H., Hajnsek, I., Eineder, M., Werner, M., Moreira, A., 2005. TanDEM-X: mission concept and performance analysis. In IEEE International Geoscience and Remote Sensing Symposium, Vol. 7, pp. 4890-4893.
- Kley, J., 2013. Saxonische Tektonik im 21. Jahrhundert. *Z. Dtsch. Ges. Geowiss.* 164, 295–311.
- Kobayashi, T., Morishita, Y., Yurai, H., 2015. Detailed crustal deformation and fault rupture of the 2015 Gorkha earthquake, Nepal, revealed from ScanSAR-based interferograms of ALOS-2. *Earth, Planets and Space* 67:1–13. <http://dx.doi.org/10.1186/s40623-015-0359-z>.
- Koch, A., Martin, M., Prestel, R., Ruch, C., Sage, A., Trapp, C., 2015. Geologische Untersuchungen von Baugrundhebungen im nordöstlichen Stadtgebiet von Böblingen (Hebungsgebiet "Nord") – Sachstandsbericht –. Az.: 95-4764//15-7202 Kh/Mt/Ps/Ru/Sag/Tr/W/Pop, 159p., Landesamt für Geologie, Rohstoffe und Bergbau (LGRB), Available at (accessed on 1.10.2022): <https://lgrbwissen.lgrb-bw.de/medien/dokumente/lgrb-dokumente-sachstandsbericht-ews-schadensfaelle-boeblingen-mit-anlagen.pdf> (in German).
- Kockel, F., Krull, P., Reinhold, K., 2008. Salt Structures of Northern Gemany (1:500,000). BGR, Hannover available at (accessed on 29.06.2016):. https://download.bgr.de/bgr/Geologie/Salzkarte/pdf600/BGR_Salzkarte.zip.
- Krauter, E., 2001. Phänomenologie natürlicher Böschungen (hänge) und ihrer massenbewegungen. In Grundbau-Taschenbuch, 1st ed., Smolczyk, U., Ed., Ernst & Sohn: Berlin, Germany, Volume 6, pp. 613–666.
- Lahner, L., Wellmer, F.-W., 2004. Geoscientific Map of Germany 1:2,000,000 — Important Deposits. BGR, Hannover available at (accessed on 29.06.2016):. <https://download.bgr.de/bgr/Rohstoffe/GK2000/GK2000Lagerstaetten/pdf/Lagerstaettenkarte.zip>.
- Lanari, R., Mora, O., Manunta, M., Mallorquí, J.J., Berardino, P., Sansosti, E., 2004. A small-baseline approach for investigating deformations on full-resolution differential SAR interferograms. *IEEE Trans. Geosci. Remote Sens.* 42, 1377–1386.
- Lazecky, M., Hlavacova, I., Bakon, M., Sousa, J. J., Perissin, D., Patricio, G., 2017. Bridge Displacements Monitoring Using Space-Borne X-Band SAR Interferometry. *IEEE Journal of Selected Topics in Applied Earth Observations and Remote Sensing*, vol. 10, no. 1, pp. 205–210, Jan. 2017, doi: 10.1109/JSTARS.2016.2587778.
- LBEG, 2014. Oil and Gas Fields in Lower-Saxony, Pers. communication with Dr. Viola.
- LBEG, 2015. Crude Oil and Natural Gas in Germany — Annual Report. Available at (accessed on 15.06.2016):. <http://www.lbeg.niedersachsen.de/erdoel-erdgas-jahresbericht/jahresbericht-erdoel-und-erdgas-in-der-bundesrepublik-deutschland-936.html#english>.
- LBM, 2018. Auswertung der Corner Reflektor Messung vom 14.06.2018, Landesbetrieb Mobilität Rheinland-Pfalz: Trier, Germany.
- Lege, T., 2014. Detektion und Monitoring von Geofahren, Oberflächen- und Massenbewegungen, chapter 5.5. Erdbeobachtung für Mensch und Umwelt. Ergebnisbericht (Version 2). BMVI, BMUB, BMI and DLR 2014 :pp. 21–22 available at (accessed on 15.06.2016):. http://www.d-gmes.de/sites/default/files/dokumente/Forum_2014/Ergebnisbericht_2014_Version2.pdf.
- Lege, T., Frei, M., Kalia, A. C., 2016. Integrated InSAR based copernicus ground motion service for Germany — paleoseismic aspects. 7th International INQUA Meeting on Paleoseismology,

- Active Tectonics and Archeoseismology (PATA). INQUA Focus Group on Paleoseismology and Active Tectonics, Crestone, Colorado, USA.
- LGB, 2003. Geologische Übersichtskarte von Rheinland-Pfalz 1:300,000, State Office of Geology and Mining Rhineland-Palatinate: Mainz, Germany.
- Li, F. K., Goldstein, R. M., 1990. Studies of multibaseline spaceborne interferometric synthetic aperture radars, *IEEE Trans. Geosci. Remote Sens.*, vol. 28, pp. 88–96.
- Liebhart, W., Adam, N., Rodriguez Gonzalez, F., Parizzi, A., Cong, X.Y., 2012. Four level least squares adjustment in Persistent Scatterer Interferometry for the Wide Area Product. *IEEE International Geoscience and Remote Sensing Symposium (IGARSS)*, pp. 3859–3862.
- Liu, Y., Brown, J., Demargne, J., Seo, D.-J., 2011. A wavelet-based approach to assessing timing errors in hydrologic predictions. *J Hydrol* 397(3–4):210–224.
- Liu, Y., Qiu, H., Yang, D. et al., 2022. Deformation responses of landslides to seasonal rainfall based on InSAR and wavelet analysis. *Landslides* 19, 199–210, <https://doi.org/10.1007/s10346-021-01785-4>.
- López-Dekker, P., Biggs, J., Chapron, B., Hooper, A., Käab, A. et al., 2021. The Harmony Mission: End of Phase-0 Science overview. *IEEE International Geoscience and Remote Sensing Symposium*, Jul 2021, Brussels, Belgium. [ff10.1109/IGARSS47720.2021.9554896ff.ffhal-03797318f](https://doi.org/10.1109/IGARSS47720.2021.9554896ff.ffhal-03797318f)
- Lu, P., Casagli, N., Catani, F., Tofani, V., 2012. Persistent scatterers interferometry hotspot and cluster analysis (PSI-HCA) for detection of extremely slow-moving landslides. *Int. J. Remote Sens.*, 33, 466–489
- Lubitz, C., Motagh, M., Wetzel, H., Anderssohn, J., 2012. TerraSAR-X time series uplift monitoring in Staufen, South-West Germany. *Geoscience and Remote Sensing Symposium (IGARSS)*, pp. 1306–1309.
- Lubitz, C., Motagh, M., Wetzel, H.-U., Kaufmann, H., 2013. Remarkable urban uplift in Staufen im Breisgau, Germany: observations from TerraSAR-X InSAR and leveling from 2008 to 2011. *Remote Sens.* 5, 3082–3100.
- Mahapatra, P., van der Marel, H., van Leijen, F., Samiei-Esfahany, S., Klees, R., Hanssen, R., 2015. Connecting InSAR to a global geodetic datum: towards absolute scatterer displacements. *FRINGE 2015*. ESA-ESRIN, Frascati (Rome), Italy.
- Main, I. G., Leonard, T., Papasouliotis, O., Hatton, C. G., Meredith, P. G., 1999. One slope or two? Detecting statistically significant breaks of slope in geophysical data with application to fracture scaling relationships, *Geophys. Res. Lett.*, 26, 2801–2804.
- Mancini, F., Grassi, F., Cenni, N. A., 2021. Workflow Based on SNAP–StaMPS Open-Source Tools and GNSS Data for PSI-Based Ground Deformation Using Dual-Orbit Sentinel-1 Data: Accuracy Assessment with Error Propagation Analysis. *Remote Sens.*, 13, 753. <https://doi.org/10.3390/rs13040753>
- Mansour, M. F., Morgenstern, N. R., Martin, C. D., 2011. Expected damage from displacement of slow-moving slides. *Landslides*, 8, 117–131.

- Massonnet, D., Rossi, M., Carmona, C., Adragna, F., Peltzer, G., Feigl, K., Rabaute, T., 1993. The displacement field of the Landers earthquake mapped by radar interferometry. *Nature* 364, 138–142.
- Navarro, J. A., Cuevas-González, M., Tomás, R., Barra, A., Crosetto, M., 2019. A toolset to detect and classify Active Deformation Areas using interferometric SAR data. In *Proceedings of the 5th International Conference on Geographical Information Systems Theory, Applications and Management (GISTAM 2019)*, 3-6 May 2019, Crete (Greece).
- Notarnicola, C., Paloscia, S., Pierdicca, N., Bovenga, F., Refice, A., Pasquariello, G., Nitti, D.O., Nutricato, R., 2014. Corner Reflectors and Multi-temporal SAR Inteferometry for Landslide Monitoring. 9243 p. 92430.
- Notti, D., Herrera, G., Bianchini, S., Meisina, C., García-Davalillo, J. C., Zucca, F. A., 2014. methodology for improving landslide psi data analysis. *Int. J. Remote Sens.*, 35, 2186–2214.
- Notti, D., Meisina, C., Zucca, F., Colombo, A., 2011. Models to predict persistent scatterers data distribution and their capacity to register movement along the slope. In *Proceedings of the Fringe Workshop 2011*, Frascati, Italy, 19–23 September.
- Nourani, V., Ghasemzade, M., Mehr, A., Sharghi, E., 2019. Investigating the effect of hydroclimatological variables on Urmia Lake water level using wavelet coherence measure. *Journal of Water and Climate Change* 10(1):13–29
- Oyen, A., 2017. Towards an insar based nationwide monitoring strategy in the Netherlands. In *Proceedings of the Fringe 2017—10th International Workshop on Advances in the Science and Applications of SAR Interferometry and Sentinel-1 InSAR*, Helsinki, Finland, 5–9 June 2017.
- Prats-Iraola, P., Scheiber, R., Marotti, L. et al., 2012. TOPS Interferometry with TerraSAR-X, *IEEE Transactions on Geoscience and Remote Sensing*, vol. 50, no. 8, pp. 3179–3188.
- Parizzi, A., Brcic, R., De Zan, F., 2021. InSAR Performance for Large-Scale Deformation Measurement. *IEEE Transactions on Geoscience and Remote Sensing*, vol. 59, no. 10, pp. 8510-8520, doi: 10.1109/TGRS.2020.3039006.
- Parizzi, A., Rodriguez Gonzalez, F., Brcic, R., 2020. A Covariance-Based Approach to Merging InSAR and GNSS Displacement Rate Measurements. *Remote Sens.*, 12, 300, <https://doi.org/10.3390/rs12020300>.
- Parizzi, A., 2015. GPS Requirements for PSI Calibration, Personal communication.
- Raucoules, D., Bourguin, B., de Michele, M., Le Cozannet, G., Closset, L., Bremmer, C., Veldkamp, H., Tragheim, D., Bateson, L., Crosetto, M., Agudo, M., Engdahl, M., 2009. Validation and intercomparison of Persistent Scatterers Interferometry: PSIC4 project results. *J. Appl. Geophys.* 68, 335–347.
- Raspini, F., Bianchini, S., Ciampalini, A., Del Soldato, M., Solari, L., Novali, F., Del Conte, S., Rucci, A., Ferretti, A., Casagli, N., 2018. Continuous, semi-automatic monitoring of ground deformation using Sentinel-1 satellites. *Sci. Rep.*, 8, 1–11.

- Riedmann, M., Lang, O., Bindrich, M., 2015. Terrasar-x basierte Hangrutschüberwachung bei Graach Rheinland-Pfalz. In *GeoMonitoring 2015*, Hrgs. Busch, W, Knospe, S., Clausthal-Zellerfeld, Germany, p. 250.
- Righini, G., Pancioli, V., Casagli, N., 2012. Updating landslide inventory maps using persistent scatterer interferometry (PSI). *Int. J. Remote Sens.*, 33, 2068–2096.
- Rodriguez Gonzalez, F., Parizzi, A., Brcic, R., 2018. Evaluating the impact of geodetic corrections on interferometric deformation measurements. In: *Proceedings of the European Conference on Synthetic Aperture Radar, EUSAR*, p. 377-381. VDE Verlag GmbH. EUSAR 2018, 4.-7. June 2018, Aachen, Germany. ISBN 978-3-8007-4636-1. ISSN 2197-4403.
- Rodriguez Gonzalez, F., Bhutani, A., Adam, N., 2011. L1 network inversion for robust outlier rejection in persistent scatterer interferometry. In *Proceedings of the 2011 IEEE International Geoscience and Remote Sensing Symposium, Vancouver, BC, Canada, 24–29 July 2011*, pp. 75–78.
- Rodriguez Gonzalez, F., Parizzi, A., Fuh Chuo, E., Brcic, R., Shau, R., Adam, N., Redl, S., Siegmund, R., 2017. *Processing Report for the Ground Motion Service Germany*, DLR Oberpfaffenhofen, Germany, p. 627.
- Rogall, M., 2014. *Gefahrenhinweiskarte Mittelmosel —Rutschungen und Steinschläge 1:50.000 Erläuterungen*. State Office of Geology and Mining Rhineland-Palatinate, Mainz, Germany, p. 32.
- Rosen, P., Hensley, S., Joughin, I., Li, F., Madsen, S. N., Rodriguez, E., Goldstein, R., 2000. *Synthetic Aperture Radar Interferometry*. *Proceedings of the IEEE*, 88(3), 333-382.
- Rosi, A., Tofani, V., Tanteri, L., Tacconi Stefanelli, C., Agostini, A., Catani, F., Casagli, N., 2017. The new landslide inventory of Tuscany (Italy) updated with PS-InSAR: Geomorphological features and landslide distribution. *Landslides*, 15, 5–19.
- Sassa, K. F. H., Wang, F., Wang, G., 2005. *Landslides—Risk Analysis and Sustainable Disaster Management*, Springer: Berlin, Germany, Vol. 1.
- Schwarz, G., 1978. Estimating the dimension of a model. *Ann. Stat.*, 6:461–464.
- Scheiber, R., Moreira, A., 2000. Coregistration of interferometric SAR images using spectral diversity. *IEEE Transactions on Geoscience and Remote Sensing*, vol. 38, no. 5, pp. 2179–2191.
- Shau, R., Goel, K., Adam, N., 2016. *Erläuterungen zur Berechnung der Absolutwerte und Varianzen des PSI Referenznetzwerks*, Personal communication.
- Shi, X., Jiang, H., Zhang, L., Liao, M., 2017. Landslide displacement monitoring with split-bandwidth interferometry: A case study of the shuping landslide in the three gorges area. *Remote Sens.*, 9, 937.
- Solari, L., Del Soldato, M., Raspini, F., Barra, A., Bianchini, S., Confuorto, P., Casagli, N., Crosetto, M., 2020. Review of Satellite Interferometry for Landslide Detection in Italy. *Remote Sens.*, 12, 1351, <https://doi.org/10.3390/rs12081351>.
- Spies, T., Kaiser, D., Schlittenhardt, J., Reicherter, K., Hürtgen, J., 2016. Establishment of a comprehensive data base for seismic hazard assessment in Germany and Central Europe.

using historical, paleoseismic and neotectonic evidence. 7th International INQUA Meeting on Paleoseismology, Active Tectonics and Archeoseismology (PATA). INQUA Focus Group on Paleoseismology and Active Tectonics, Crestone, Colorado, USA.

- Stange, F., 2007. BOART1000OB V2.0. 2007. (C) BGR, Hannover available at (accessed on: 29.06.2016): https://download.bgr.de/bgr/Boden/BOART1000/shp/boart1000_ob_v20.zip.
- Steffen, H., Wu, P., 2011. Glacial isostatic adjustment in Fennoscandia—a review of data and modeling. *J. Geodyn.* 52, 169–204.
- Steven, A. J., 2001. Inference and estimation in a changepoint regression problem. *The Statistician*, 50, 51–61.
- Thornthwaite, C. W., Mather, J. R., 1957. Instruction and tables for computing potential evapotranspiration and the water balance. John Hopkins Univ., Laboratory in Climatology, Publ. in Climat., 10, No. 3.
- Toloczyki, M., Trurnit, P., Voges, A., Wittekindt, H., 2006. Geological Map of Germany 1: 1,000,000 (GK1000). BGR, Hannover available at (accessed on: 29.06.2016): <https://download.bgr.de/bgr/Geologie/GK1000/shp/GK1000.zip>.
- Tomás, R., Ignacio Pagán, J., Navarro, J. A. et al., 2019. Semi-Automatic Identification and Pre-Screening of Geological-Geotechnical Deformational Processes Using Persistent Scatterer Interferometry Datasets. *Remote Sensing*, Vol. 11, No. 14, <https://doi.org/10.3390/rs11141675>.
- Tomás, R., Li, Z., Lopez-Sanchez, J. M. et al., 2016. Using wavelet tools to analyse seasonal variations from InSAR time-series data: a case study of the Huangtupo landslide. *Landslides* 13, 437–450, <https://doi.org/10.1007/s10346-015-0589-y>.
- Tomás, R., Herrera, G., Delgado, J., Lopez-Sanchez, J.M., Mallorquí, J.J., Mulas, J., 2010. A ground subsidence study based on DInSAR data: Calibration of soil parameters and subsidence prediction in Murcia City (Spain). *Eng. Geol.* 111, 19–30.
- Tomás, R., Ignacio Pagán, J., Navarro J. A., Cano, M. Luis Pastor, J., Riquelme, A., Cuevas-González, M. Crosetto, M. Barra, A., Monserrat, O., López-Sánchez, J. M., Ramón, A., Iborra, S., del Soldato, M., Solari, L., Bianchini, S., Raspini F., Novali, F., Ferreti, A., Constantini, M., Trillo, F., Herrera, G. and Casagli, N., 2019. Semi-Automatic Identification and Pre-Screening of Geological-Geotechnical Deformational Processes Using Persistent Scatterer Interferometry Datasets, *Remote Sensing*, Vol. 11, No. 14, <https://doi.org/10.3390/rs11141675>.
- Torres, R., Snoeij, P., Geudtner, D., Bibby, D., Davidson, M., Attema, E., Potin, P., Rommen, B., Floury, N., Brown, M., Traver, I.N., Deghaye, P., Duesmann, B., Rosich, B., Miranda, N., Bruno, C., L'Abbate, M., Croci, R., Pietropaolo, A., Huchler, M., Rostan, F., 2012. GMES Sentinel-1 mission. *Remote Sens. Environ.* 120, 9–24.
- Turner, A. K., Schuster, R. L., 1996. Special Report 247, Transportation Research Board, US National Research Council: Washington, DC, USA, pp. 36–75.
- Ulaby, F. T., Moore, R. K., Fung, A. K., 1982. Radar Remote Sensing and Surface Scattering and Emission Theory. *Microwave Remote Sensing Active and Passive*, I, 624 p.

- Ulmer, F.-G., Adam, N., 2015. A synergy method to improve ensemble weather predictions and differential SAR interferograms. *ISPRS J. Photogramm. Remote Sens.* 109, 98–107. Van Leijen, F., 2014.
- USGS, 2004. Landslide Types and Processes. USGS fact sheet 2004-3072, 4 p. <https://pubs.usgs.gov/fs/2004/3072/pdf/fs2004-3072.pdf> (accessed on 3.10.2022).
- Van Leijen, F., 2014. Persistent Scatterer Interferometry Based on Geodetic Estimation Theory. Ph.D. Thesis, TU Delft, Institutional Repository, Delft, Netherlands.
- Veldkamp, H., Tragheim, D., Bateson, L., Crosetto, M., Agudo, M., Engdahl, M., 2009. Validation and intercomparison of Persistent Scatterers Interferometry: PSIC4 project results. *J. Appl. Geophys.* 68, 335–347.
- Wendleder, A., Felbier, A., Wessel, B., Huber, M., Roth, A., 2016. A Method to Estimate Long-Wave Height Errors of SRTM C-Band DEM. *IEEE Geoscience and Remote Sensing Letters*, vol. 13, no. 5, pp. 696-700, May 2016, doi: 10.1109/LGRS.2016.2538822.
- Werner, C., Wegmüller, U., Strozzi, T., Wiesmann, A., 2003. Interferometric point target analysis for deformation mapping. *International Geoscience and Remote Sensing Symposium (IGARSS)*, pp. 4362–4364.
- Werner, C., Strozzi, T., Wiesmann, A., Wegmüller, U., Murray, T., Pritchard, H., Luckman, A., 2001. Complimentary measurement of geophysical deformation using repeat-pass SAR. In *Proceedings of the IGARSS 2001, Scanning the Present and Resolving the Future, IEEE 2001 International Geoscience and Remote Sensing Symposium, Sydney, Australia, 9–13 July 2001, Vol. 3257*, pp. 3255–3258.
- Werninghaus, R., 2004. TerraSAR-X mission. *Proc. SPIE 5236 SAR Image Analysis, Modeling, and Techniques*, VI., 9, pp. 9–16, <http://dx.doi.org/10.1117/12.511500>.
- Wolf, C., 2012. Analysis of ground motion in areas of underground storage of oil and gas and natural gas production in the North German Lowland. *TerraFirma Product - Interpretation Report, V1.0*. BGR, Hannover, p. 36 (unpublished).
- Xi, F., 2017. Detektion von Anormalen Zeitreihen an Persistent-Scatterer-Punkten im Zusammenhang mit der Ableitung Flächenhafter Bodenbewegungen. *Doctoral Thesis, TU Clausthal, Clausthal-Zellerfeld, Germany*.
- Zebker, H., Villasenor, J., 1992. Decorrelation in interferometric radar echoes. *IEEE Transactions on Geoscience and Remote Sensing*, vol. 30, no. 5, pp. 950-959.
- Zhao C and Lu Z (2018) Remote Sensing of Landslides - A Review. *Remote Sens.*, 10, 279, <https://doi.org/10.3390/rs10020279>.
- Zinno, I., Mossucca, L., Elefante, S., De Luca, C., Casola, V., Terzo, O., Casu, F., Lanari, R., 2016. Cloud computing for earth surface deformation analysis via spaceborne radar imaging: a case study. *IEEE Transactions on Cloud Computing* 4, 104–118.
- Zitzmann, A., 2003. The geological map of Germany 1:200,000—From analogous sheets to a geological data bank. *Zeitschrift der Deutschen Geologischen Gesellschaft*, 154, 121–139.

Acknowledgement

I would like to thank my supervisors from the Institute of Photogrammetry and Geoinformation (IPI) Prof. Dr. Mahdi Motagh and Prof. Dr. Christian Heipke for their guidance, continuous support and scientific advice in all stages of my PhD research. I thank Dr. Mahmud Haghshenas Haghshenas for fruitful discussions and critical proof reading.

I thank Nico Adam (DLR) for fruitful discussion regarding InSAR.

I thank Dr. Michaela Frei and Dr. Thomas Lege (BGR) for providing me the opportunity to perform a PhD research. I thank Dr. Martin Schodlok for his guidance and proof reading.

I thank my parents, Maria and Abdoerrahim, and my sisters, Tania and Anette, for continuous support and love. I thank my girlfriend, Ina, for her love and endless patience.

Curriculum Vitae

Personal Information

Andre Cahyadi Kalia
Born on 25.05.1984 in Friedberg, Germany

Study

2004-2011
Dipl.-Geographer
Justus Liebig University, Gießen, Germany

Work experience

2011-2013
Scientist
University of Hohenheim, Stuttgart, Germany

2013-now
Scientist
Federal Institute for Geosciences and Natural Resources (BGR),
Hannover, Germany

Peer reviewed publications

2017
Kalia, A. C., Frei, M., Lege, T.: A Copernicus downstream-service for the nationwide monitoring of surface displacements in Germany, *Rem. Sens. of Environ.*, Volume 202, p. 234-249, ISSN 0034-4257, <https://doi.org/10.1016/j.rse.2017.05.015>

2018
Kalia, A. C.: Classification of landslide activity on a regional scale using Persistent Scatterer Interferometry at the Moselle Valley (Germany), *Remote Sens.*, 10(12), 1880; <https://doi.org/10.3390/rs10121880>

2021
Pilger, C., Gaebler, P., Hupe, P., **Kalia, A. C.**, Schneider, F. M., Steinberg, A., Sudhaus, H., Ceranna, L.: Yield estimation of the 2020 Beirut explosion using open access waveform and remote sensing data. *Sci. Rep.* 11, 14144. <https://doi.org/10.1038/s41598-021-93690-y>

2021
Kalia, A. C., Frei, M., Lege, T.: BodenBewegungsdienst Deutschland (BBD): Konzept, Umsetzung und Service-Plattform. *Zeitschrift für Geodäsie, Geoinformation und Landmanagement (zfv)*, Wißner-Verlag, 146(4), S. 273-279, DOI: 10.12902/zfv-0365-2021, <https://geodaesie.info/zfv/heftbeitrag/8701>

2022
Kalia, A. C.: Landslide activity detection based on Sentinel-1 PSI datasets of the Ground Motion Service Germany - The Trittenheim case study. *Landslides*, DOI: 10.1007/s10346-022-01958-9

Eidesstattliche Erklärung

Ich erkläre an Eides statt,

- die Regeln der geltenden Promotionsordnung zu kennen und eingehalten zu haben und mit einer Prüfung nach den Bestimmungen der Promotionsordnung einverstanden zu sein,
- die Dissertation selbst verfasst zu haben (Selbständigkeitserklärung), keine Textabschnitte von Dritten oder eigener Prüfungsarbeiten ohne Kennzeichnung übernommen und alle von ihr oder ihm benutzten Hilfsmittel und Quellen in seiner Arbeit angegeben zu haben,
- Dritten weder unmittelbar noch mittelbar geldwerte Leistungen für Vermittlungstätigkeiten oder für die inhaltliche Ausarbeitung der Dissertation erbracht zu haben (d.h. die wissenschaftliche Arbeit darf weder in Teilen noch in Gänze von Dritten gegen Entgelt oder sonstige Gegenleistung erworben oder vermittelt worden sein),
- die Dissertation noch nicht als Prüfungsarbeit für eine staatliche oder andere wissenschaftliche Prüfung eingereicht zu haben.

Ich habe die gleiche oder eine in wesentlichen Teilen ähnliche Arbeit bei keiner anderen Hochschule als Dissertation eingereicht.

Hannover, 8.3.2023